



**The Scientific Institute for Advanced Training and Studies**

**Experimental  
and  
Theoretical NANOTECHNOLOGY**

**Vol. 4, No. 2, 2020**

**Yarub Al-Douri  
Editor-in-Chief**

**e-ISSN: 2590-4132**

**Honorary Editor: M. Nayfeh (USA)**

---

**Editors**

S. Abdullah (Malaysia)	H. Ekinçi (Turkey)	M-B Leptit (France)	T. E. Simos (Greece)
O. Alani (UK)	S. El-Safty (Japan)	J. Lui (USA)	J. Sing (Australia)
M. Ameri (Algeria)	Y. P. Feng (Singapore)	R. Nowak (Finland)	P. R. Somani (India)
N. E. Arif (Iraq)	L. Feo (Italy)	S. Radiman (Malaysia)	M. Tanemura (Japan)
V. K. Arora (USA)	M. Henni (UK)	M. V. Reddy (Singapore)	N. Tit (UAE)
M. Al-Jassim (USA)	A.Hui (USA)	A. H. Reshak (Czech Republic)	K. D. Verma (India)
S. Baroni (Italy)	M. R. Johan (Malaysia)	A. Rubio (Spain)	S. Wang (Singapore)
M. Bounoudina (Bahrain)	R. Jose (Malaysia)	M. Rusop (Malaysia)	J. Whitaker (USA)
Z. Cai (USA)	N. Joshi (USA)	P. Ruterana (France)	A.Zaoui (France)
A.Chaudhry (India)	A. H. Jumaa (Iraq)	P. Schwerdtfeger (New Zealand)	D. H. Zhang (Singapore)
N. E. Christensen (Denmark)	M. A. R. Khan (USA)	U.Schwingenschlo egl (Germany)	
D. Chua (Singapore)	R. Khenata (Algeria)		

---

**Contact us**

Experimental and Theoretical NANOTECHNOLOGY

Prof. Dr. Yarub Al-Douri; Editor-in-Chief : [editor.etn@siats.co.uk](mailto:editor.etn@siats.co.uk)

<http://etn.siats.co.uk>

**Experimental and Theoretical  
NANOTECHNOLOGY**  
<http://etn.sjats.co.uk/>

*Experimental and Theoretical NANOTECHNOLOGY*

**VOL. 4, NO. 2, 2020**

**e-ISSN 2590-4132**

**2020**



## ***Experimental and Theoretical NANOTECHNOLOGY***

Experimental and Theoretical NANOTECHNOLOGY is a multidisciplinary peer-reviewed international journal published four issues a year. It includes specialized research papers, short communications, reviews and selected conference papers in special issues on the characterization, synthesis, processing, structure and properties of different principles and applications of NANOTECHNOLOGY; with focus on advantageous achievements and applications for the specialists in engineering, chemistry, physics and materials science.

Experimental and Theoretical NANOTECHNOLOGY covers and publishes all aspects of fundamental and applied researches of experimental and theoretical nanoscale technology dealing with materials synthesis, processing, nanofabrication, nano probes, spectroscopy, properties, biological systems, nanostructures, nano electronics, nano-optics, nano-mechanics, nano-devices, nano biotechnology, nanomedicine, Nano toxicology within the scope of the journal. Experimental and Theoretical NANOTECHNOLOGY aims to acquire the recent and outstanding researches for the benefit of the human being.

## Synthesis of GaN nanowires by ammoniating Ga<sub>2</sub>O<sub>3</sub>/BN

L. Needs, K. Williams\*

School of Computing Science and Engineering, University of Salford, Salford, United Kingdom

\*) Email: [k.williams@salford.ac.uk](mailto:k.williams@salford.ac.uk)

Received: 1/9/2019 / Accepted: 19/1/2020 / Published: 1/4/2020

---

GaN nanowires were successfully prepared on Si(111) substrate through ammoniating Ga<sub>2</sub>O<sub>3</sub>/BN films deposited by radio frequency magnetron sputtering system. The synthesized nanowires were confirmed as hexagonal wurtzite GaN by X-ray diffraction, selected-area electron diffraction and Fourier transform infrared spectra. Scanning electron microscopy and transmission electron microscopy revealed that the grown GaN nanowires have a smooth and clean surface with diameters ranging from 40 to 160 nm and lengths typically up to several tens of micrometers. The representative photoluminescence spectrum at room temperature exhibited a strong UV light emission band centered at 363 nm and a relative weak purple light emission peak at 422 nm. The growth mechanism is discussed briefly.

---

**Keywords:** Sputtering; GaN; Photolumines.

### 1. Introduction

GaN has been considered to be the most promising optoelectronic material for such applications as light emitting diodes (LEDs), laser diodes (LDs) as well as high power electronic devices, due to its large direct energy band gap of 3.39 eV at room temperature and strongly emissive properties[1,2]. In the past decade, one-dimensional GaN nanomaterials have attracted extensive attention owing to their great uses in the novel nanoelectronic devices and the quantum devices[3]. Up to the present, several techniques have been developed to prepare one-dimensional GaN nanomaterials such as carbon nanotube-confined reaction[4], template-based growth method<sup>[5]</sup>, catalytic growth<sup>[6]</sup> and direct reaction of metal Ga with NH

[7]. Furthermore, Huang *et al.* have reported successful fabrication of logic gates and demonstrated the computation capabilities from assembled *p*-Si and *n*-GaN crossed nanowire junctions[8]. However, the synthesis of high-quality GaN nanowires with a large-scale on Si substrate is very important for the

application of GaN nanowires, and needs to be optimized.

In this paper, we report a successful synthesis of highly crystalline GaN nanowires through ammoniating Ga<sub>2</sub>O<sub>3</sub>/BN films on Si(111) substrate deposited by radio frequency (RF) magnetron sputtering system. We chose hexagonal BN on Si (denoted BN/Si) as a substrate for hexagonal GaN films growth because of the reasonably low lattice mismatch (8%)[9] and higher thermal conductivity than that of sapphire; the latter is insulating and is poorly lattice matched (16%). Moreover, if GaN can be prepared on BN/Si, it will offer a very attractive way to incorporate future GaN optoelectronic devices into silicon-based very large-scale integrated circuits.

## 2. Experiment

The GaN nanowires were prepared by a two-step method. The first step was to deposit Ga<sub>2</sub>O<sub>3</sub>/BN films on Si(111) substrate in turn using a JCK-500A RF magnetron sputtering system (13.56 MHz). The targets for depositing BN films and Ga<sub>2</sub>O<sub>3</sub> films were hot-pressed BN with a purity of 99.9% and sintered Ga<sub>2</sub>O<sub>3</sub> with a purity of 99.99%. The base pressure before sputtering was about  $6.4 \times 10^{-4}$  Pa. The working gas was pure argon and the working pressure was 2 Pa. During deposition, the substrate' temperature was fixed at 300 K by a water-cooled pipe, and the RF power was adjusted to 150 W. The distance between the target and substrate was 8 cm, and the deposition time was about 20 min for BN films and 90 min for Ga<sub>2</sub>O<sub>3</sub> films.

Subsequently, the samples were ammoniated under flowing ammonia atmosphere in an open tube furnace. When the furnace reached the equilibrium temperature of 950°C, the quartz boat with the samples was pushed into the constant temperature region of the furnace. Flowing N<sub>2</sub> was first introduced into the tube for 5 min to flush out the residual air. Then NH<sub>3</sub> was flowed into the tube for 15 min at a flow rate of 800 mL/min while the N<sub>2</sub> was switched off. At the end of the ammoniating process, the NH<sub>3</sub> was flushed out by N<sub>2</sub> before the boat was taken out of the furnace.

A scanning electron microscope (SEM, Hitachi S-570), transmission electron microscope (TEM, Hitachi H-800) and high-resolution transmission electron microscope (HRTEM, Philips TECNAI-20) were used to observe the morphology of the synthesized samples. X-ray diffraction (XRD, Rigaku D/max-rB Cu K $\alpha$ ) and Fourier transform infrared spectroscopy (FTIR, TENSOR27) were used to examine the crystalline structure and elemental state of the samples. The photoluminescence (PL) spectra of the samples were measured in an FLS920 fluorescence spectrophotometer at room temperature.

## 3. Results and discussion

Figure 1 shows the typical SEM images of the synthesized samples at different magnifications. At low magnification, it can be clearly observed from Fig. 1(a) that a great deal of micrometre-sized spheres with diameters ranging from 2 to 27  $\mu$ m is sparsely distributed over a large area on the Si substrate. In fact, the whole surface of the substrate is found to be covered with spheres by the full-scale observation of SEM. And the further ob-

servation reveals that each sphere consists of a large cluster of high-density nanowires as shown in the high magnification image (Fig. 1(b)). The SEM image of Fig. 1(c) demonstrates that the nanowires possess a very smooth surface and a relatively straight morphology with a diameter of about 40–160 nm and a length of about several tens of micrometers, which is possibly favorable for the future applications of nanodevice.

Figure 2 shows the typical XRD pattern of the samples. All the reflection peaks can be indexed to a hexagonal wurtzite GaN phase with lattice constants of  $a = 0.3186$  nm and  $c = 0.5178$  nm, which are well consistent with the reported values for one-dimensional GaN nanomaterials[10]. The low-intensity (0002) peak, in comparison with that of ref. [10], may be attributed to a small quantity of nanowires grown along the [0001] direction. No diffraction peaks from Ga<sub>2</sub>O<sub>3</sub>, BN or other crystalline impurities were found in any of our samples, indicating that the sample was of high purity. And the sharp diffraction peaks also revealed that the GaN nanowires thus prepared had a high crystalline quality.

Figure 3(a) shows the TEM image of a single GaN nanowire with a diameter of about 60 nm, providing more structural information. It is straight and has a fairly clean surface without any particles. Figure 3(b) shows an HRTEM lattice image of another GaN nanowire. The distinct lattice fringes indicate that the nanowire is single crystal. No defect was observed in the lattice image, revealing that the nanowire has a high-quality crystal lattice. The spacing between two conjoint planes is about 0.243 nm, which corresponds to the {10 11} planes of hexagonal GaN, indicating that the growth plane of the nanowire is one of the {10 11} planes. The single crystalline nature of the nanowire can also be identified from the corresponding selected area electron diffraction (SAED) pattern taken by the fast Fourier transform (FFT) techniques (Fig. 3(c), which can be indexed to the reflection of the hexagonal wurtzite GaN along the [1213] axis.

Figure 4 shows the FTIR transmission spectrum of the synthesized GaN nanowires. Four prominent IR absorption bands were observed at 563 (band 1), 609 (band 2), 670 (band 3) and 1105 cm<sup>-1</sup> (band 4), respectively. According to refs. [9,10], band 1 corresponds to GaN stretching vibration (E<sub>1</sub>(TO) mode) in the hexagonal type GaN crystals, indicating that hexagonal GaN was obtained under current conditions, which

accords with the results of XRD and SAED. Bands 2–4 are relevant to the Si substrate. Band 2 is associated with a local vibration of substitutional carbon in the Si crystal lattice[11,12]. Band 3 is related to the absorption by Si-C bonds in amorphous phase<sup>[11]</sup>, illustrating the diffusion of carbon impurity into the Si substrate during the film growth. And band 4 is due to the Si-O-Si asymmetric stretching vibration in the SiO<sub>2</sub> resulting from oxygenation of Si substrate surface<sup>[13]</sup>.

Under 300 nm photoexcitation, a strong and broad UV light emission band centered at 363 nm and a relatively weak purple light emission peak at 422 nm are observed as shown in Figure 5. Because the as-prepared GaN nanowires are too large for quantum confinement effects, and even the thinnest GaN nanowire's diameter is much larger than the Bohr exciton radius (11 nm)[14] of GaN, the bandgap emission at 363 nm has no blue shift compared with the bulk GaN<sup>[15]</sup>. Another purple light emission peak might be ascribed to the existence of defects or surface states[16]. However, further work is needed to understand the PL mechanism of the GaN nanowires.

Although the detailed growth mechanism of the GaN nanowires is still not fully understood, we might briefly describe the process based on the above observation and the analysis. It is well known that  $\text{Ga}_2\text{O}_3$  begins to decompose into  $\text{Ga}_2\text{O}$  and Ga above  $800^\circ\text{C}$  and  $\text{NH}_3$  decomposes stepwise into  $\text{NH}_2$ ,  $\text{NH}$  and  $\text{N}$  at  $850^\circ\text{C}$ [7] in the ammoniating period. GaN molecules are subsequently formed through the reaction of  $\text{Ga}_2\text{O}$  with  $\text{NH}_3$  or the reaction of Ga atoms with N atoms. First, the GaN molecules diffuse and agglomerate into the GaN micrograins. Then the very small GaN micrograins grow up with the progress of the ammoniating and accordingly lay the foundations for the growth of nanostructured GaN. Thus the temperature, ammonia and  $\text{Ga}_2\text{O}_3$  are all crucial in the growth progress of nanostructured GaN. However, as the intermedium between Si substrate and  $\text{Ga}_2\text{O}_3$  films, BN films are also very important for the fabrication of GaN nanostructure. To test this conclusion, we also ammoniated a sample with only a deposited  $\text{Ga}_2\text{O}_3$  layer on Si(111) substrate under the same condition and duration of time, and found no such nanowires formed. A study of the detailed role of the BN films during the growth of GaN nanowires is still in progress.

#### 4. Conclusion

In summary, single-crystal GaN nanowires were successfully prepared by ammoniating  $\text{Ga}_2\text{O}_3/\text{BN}$  films at  $950^\circ\text{C}$ . SEM and TEM observations demonstrate that the as-synthesized GaN nanowires have a smooth surface with diameters ranging from 40 to 160 nm and lengths up to several tens of micrometers, which may be applied in the future nanodevices. XRD, FTIR and SAED analyses revealed that the nanowires are hexagonal wurtzite GaN. The PL spectrum at room temperature exhibited a strong emission at 363 nm and a relatively weak emission at 422 nm.

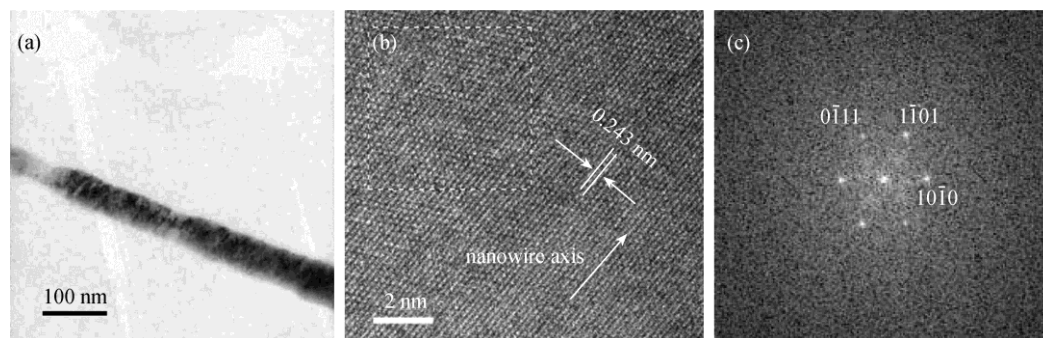


Fig. 3. (a) TEM image of a single GaN nanowire; (b) HRTEM lattice image of GaN nanowire; (c) SAED pattern taken by FFT techniques.

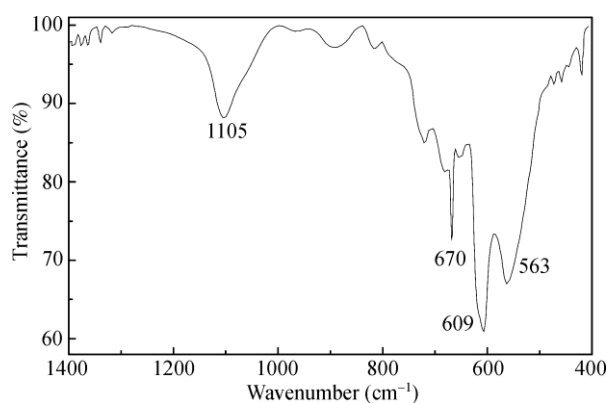


Fig. 4. FTIR transmission spectrum of the synthesized GaN nanowires.

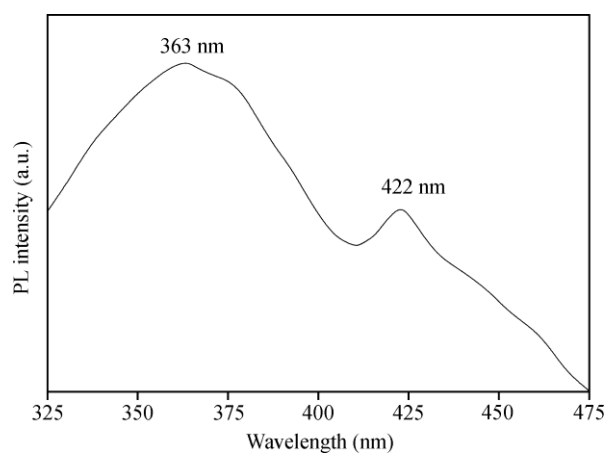


Fig. 5. PL spectrum of the synthesized GaN nanowires.

## References

- [1] S. Nivetha, R. Perumalsamy, A. Ayeshamariam, A. Mohamed Saleem, M. Karunanithy, M. Jayachandran, *Exp. Theo. NANOTECHNOLOGY* 3 (2019) 109
- [2] Brown S A, Reeves R J, Haase C S. Reactive-ion-etched gallium nitride: Metastable defects and yellow luminescence. *Appl Phys Lett*, 1999, 75(21): 3285 – 3287
- [3] Morales A M, Lieber C M. A laser ablation method for the synthesis of crystalline semiconductor nanowires. *Science*, 1998, 279(5348): 208 – 211
- [4] Han W Q, Fan S S, Li Q Q, et al. Synthesis of gallium nitride nanorods through a carbon nanotube-confined reaction. *Science*, 1997, 277: 1287 – 1289
- [5] Cheng G S, Chen S H, Zhu X G, et al. Highly ordered nanostructures of single-crystalline GaN nanowires. *Mater Sci & Eng: A*, 2000, 286: 165 – 168
- [6] Lyu S C, Cha O H, Suh E K, et al. Catalytic synthesis and photoluminescence of gallium nitride nanowires. *J Chem Phys Lett*, 2003, 367: 136 – 140
- [7] J. Hamed, H. Abd, R. Muzahim, *Exp. Theo. NANOTECHNOLOGY* 3 (2019) 131
- [8] Huang Y, Duan X, Cui Y, et al. Logic gates and computation from assembled nanowire building blocks. *Science*, 2001, 294(5545): 1313 – 1317
- [9] Boo J H, Rohr C, Ho W. MOCVD of BN and GaN thin films on silicon: new attempt of GaN growth with BN buffer layer. *J Crystal Growth*, 1998, 189/190: 439 – 444
- [10] Dong Z, Xue C, Zhuang H, et al. Synthesis of three kinds of GaN nanowires through

Ga<sub>2</sub>O<sub>3</sub> films' reaction with ammonia. Phys E, 2005, 27: 32–37

[11] Sun Y, Miyasato T, Wigmore J K. Characterization of excess carbon in cubic SiC films by infrared absorption. J Appl Phys, 1999, 85: 3377–3379

[12] Melendez-Lira M, Menendez J, Kramer K M, et al. Substitutional carbon in Si<sub>1-y</sub> C<sub>y</sub> alloys as measured with infrared absorption and Raman spectroscopy. J Appl Phys, 1997, 82: 4246–4252

[13] Meng G W, Zhang L D, Qin Y, et al. Synthesis of β-SiC nanowires with SiO<sub>2</sub> wrappers. Nanostructured Materials, 1999, 12: 1003–1006

[14] Ridley B K. Quantum Process in Semiconductors. Oxford: Clarendon, 1982. 62–66

[15] Tagreed K. Hamad, Alaa H. Ali, Alaa J. Ghazai, Hussein T. Salloom, Exp. Theo. NANOTECHNOLOGY 3 (2019) 149

[16] Chen C C, Yeh C H, Chen C H, et al. Catalytic growth and characterization of gallium nitride nanowires. J Am Chem Soc, 2001, 123: 2791–2798

## Characterization of BiFeO<sub>3</sub> nanotube and Y-junction BiFeO<sub>3</sub> nanotubes

F.Vervliet<sup>1</sup>, D. Willinger<sup>2</sup>, L. C. Álvarez<sup>3,\*</sup>

<sup>1</sup>Department of Materials Engineering (MTM), KU Leuven, Leuven, B-3001, Belgium

<sup>2</sup>Fritz Haber Institute of the Max Planck Society, Department of Inorganic Chemistry, Faradayweg 4–6, Berlin, 14195, Germany

<sup>3</sup>Institute of Polymer Science and Technology, ICTP-CSIC, Juan de la Cierva 3, Madrid, E-28006, Spain

\*) Email: [alvalc@ictp.csic.es](mailto:alvalc@ictp.csic.es)

*Received: 2/11/2019 / Accepted: 3/3/2020 / Published: 1/4/2020*

---

Multiferroic BiFeO<sub>3</sub> (BFO) nanotube arrays (□ 100 nm in diameter and □ 50 □m in length) were synthesized by the sol-gel method utilizing the anodic aluminum oxide (AAO) membrane technique. The micro- structure and chemical components of the BFO nanotubes were investigated using scanning electron microscopy (SEM), transmission electron microscopy (TEM) and X-ray photoelectron spectrometer (XPS). The BFO nanotubes exhibited polycrystalline microstructures. The novel Y-junction BFO nano- tubes were simultaneously fabricated.

---

**Keywords:** BFO; Nanotubes; Characterization.

### 1. Introduction

Multiferroic materials having ferroelectric and ferro- magnetic properties are promising in the development of novel-concept memories[1–6]. Among the multiferroic materials studied so far, BFO has received great attention due to its high Curie temperature (850°C) and the Néel

temperature (370°C). However, the application of its bulk form has been limited by leakage problems, likely due to low resistivity, defects, and non-stoichiometry issues[7]. Recently, some groups proposed to address this problem by changing the size and shape of BFO, and BFO nanomaterials with different sizes and shapes have been synthesized. Wang et al.[1] synthesized the BFO film of about 200 nm in thickness by the hetero-epitaxially constrained growth, which had a great enhancement in polarization compared with its bulk form. Park et al.[8] synthesized pure-phase, substrate-free and single-crystalline BFO nanoparticles with the magnetization value which gradually increased with decreasing the size in a certain range. The relationship between the size of BFO nanotubes and their physical properties has also aroused much interest[9,10] due to their special applications compared with the films and nanoparticles, such as vertical magnetic recording with ultrahigh recording density and nanodevices[9]. Moreover, the BFO nanotubes that contain Bi elements offer interesting optical properties for photocatalytic applications[11], and thus it is very important to fabricate and study BFO nanotubes. The synthesis of multiferroic nanostructures with a controllable size and shape is critical not only in nanodevice applications but also in fundamental research. There are many ways to fabricate nanotubes, for example, VLS[12], liquid phase method[13], and AAO membrane method<sup>[14]</sup>. Among them, the AAO membrane method does not require complicated operation equipments and thus is cost-effective. Normally, the AAO membrane with pore diameters of 10–200 nm remains stable at high temperature and in organic solvents, and the pores are uniform in size and well aligned perpendicular to the membrane surface. These advantages make AAO templates ideal for the synthesis of oxide nanotubes. The diameter and shape of nanotubes are conveniently controlled by changing the size and structure of membrane channel[15–17]. Zhang et al.[9] synthesized the BFO nanotubes, which showed significant piezoelectric characteristics and weak ferromagnetism[10]. In this work, AAO membranes and Y-junction channel AAO membranes were fabricated using the two-step anodization process, and the BFO nanotube arrays and Y-junction BFO nanotubes were synthesized by the sol-gel method utilizing the as-prepared AAO membrane.

## 2. Experimental

### 2.1. Synthesis of BFO nanotube arrays and Y-junction BFO nanotubes

AAO membranes[15] and Y-junction channel AAO membranes[17,18] were synthesized according to the literature. An Al foil of 99.9% purity was dc anodized in 0.3 mol/L H<sub>2</sub>C<sub>2</sub>O<sub>4</sub> aqueous solution under constant voltage of 50 V for 4 h at 0°C. After chemically removing the oxide layer in the mixed solution (1.8 wt% chromic acid and 6 wt% phosphoric acid at the volume ratio of 1:1) at 60°C for 2 h, the second anodization was performed under the same conditions for 4 h. Then, the residual Al substrate was removed through the replacement reaction by putting the sample into the saturated CuSO<sub>4</sub> solution. The pores of the anodic alumina were subsequently widened by immersing the anodized templates into 6 wt% phosphoric acid at 30°C for 30 min. The same process was adopted for the fabrication of Y-junction channel AAO membranes except for the second anodization process which was divided into two stages: the first anodization stage required 50 V and 2 h; the second anodization stage required 35(50/2) V and 2h. Y-junction channels of AAO membranes were successfully

synthesized. During the material synthesis,  $\text{Bi}(\text{NO}_3)_3 \cdot 5\text{H}_2\text{O}$  and  $\text{Fe}(\text{NO}_3)_3 \cdot 9\text{H}_2\text{O}$  with molar ratio of 1:1 were added to ethylene glycol. The resulting mixture was stirred at room temperature for 30 min. The concentration of the final solution was adjusted to 0.3 mol/L with pH value of 2–3 by adding 2-methoxyethanol and nitric acid. After standing for 1–2 days, stable and yellow-brown sol was obtained. Then the two types of AAO membranes were immersed in the precursor solution for 20 min. In order to obtain the perovskite phase and to get rid of  $\text{NO}_3^-$ , the precursor-containing templates were subsequently annealed in air at  $700^\circ\text{C}$  for 30 min in the quartz tube. The samples were characterized after cooling down to room temperature.

## 2.2 Characterization method of samples

The morphologies of AAO membranes and BFO nanotube arrays were investigated using scanning electron microscopy (SEM, JSM-5600 LV, accelerating voltage 20 kV). The structure and morphology of BFO nanotubes were characterized using transmission electron microscopy (TEM, JEM-2010, accelerating voltage 200 kV). The components of the samples were investigated using X-ray photoelectron spectroscopy (XPS, KRATOS AXIS ULTR) with a monochromatic  $\text{Al } K_\alpha$  source. The wide spectrum and high-resolution spectrum were respectively run under pass energy of 80 eV and 40 eV. All spectra were corrected according to the C 1s peak at 284.8 eV.

## 3. Results and discussion

### 3.1. SEM characterization of BFO nanotube arrays

Figure 1(a) shows the top-view SEM image of the empty AAO membrane. The diameter of the pores of the as-anodized template is about 100 nm and the distribution of the pores is uniform. Figure 1(b) shows the cross-section SEM image of the empty AAO membrane. The channel of the AAO membrane is very straight and the arrangement of the channel is very uniform, too. According to the actual length of the channel, the thickness of the AAO membrane is about 50  $\mu\text{m}$ . Figure 1(c) shows the SEM surface image of BFO nanotube arrays growing in a template after partial removal of the AAO membrane using 4 mol/L NaOH. The diameter of the orderliness BFO nanotube arrays is about 100 nm. The length of BFO nanotube is tens of micrometers. EDX data (inset of Figure 1(c)) demonstrates that the BFO nanotubes consist of Bi, Fe and O, and the molar amounts of Bi and Fe are the same. The Al signal is attributed to the residual membrane.

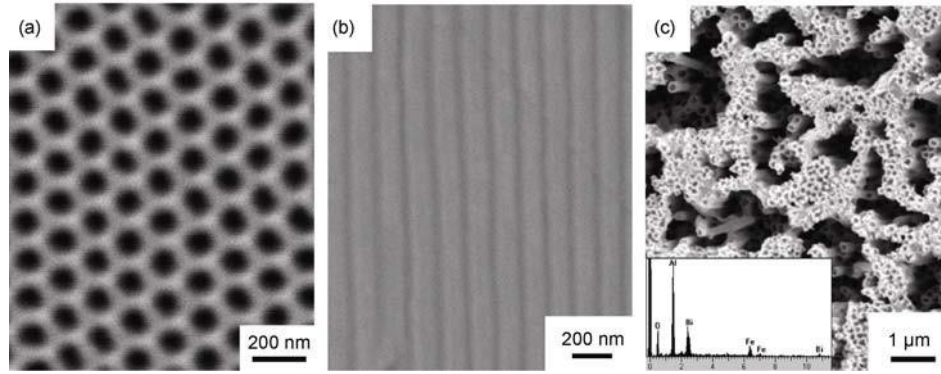


**Figure 1** (a) Top-view SEM image of the AAO membrane; (b) cross-section SEM image of the AAO membrane; (c) top-view SEM image of BFO nanotube arrays. The inset is the corresponding EDX data of BFO nanotubes.

### 3.2. TEM characterization of BFO nanotubes

For further observation of nanotubes, the samples were characterized using TEM. Before TEM observation, AAO membranes were completely dissolved for 24 h in aqueous 4 mol/L NaOH, which was cleaned in the de-ionized water for several times. The crystallinity and morphology of a single BFO nanotube of  $\approx 100$  nm in diameter were analyzed by TEM and are shown in Figure 2(a), in good agreement with the pore diameters of the AAO membranes. The inset shows the selected area electron diffraction pattern (SAED) taken from the nanotube, which reveals the polycrystalline structure nature of the BFO nanotubes. Figure 2(b) shows the 400 K TEM image of the BFO nanotube. The wall thicknesses of the nanotubes is about 15 nm and the wall is composed of many particles in sizes from several nanometers to tens of nanometers. Figure 2(c) shows the high-resolution electron microscopy (HRTEM) image of the BFO nanotube, where the well-recognized lattice spacing of about 0.281 nm corresponds to {012} atomic planes. The HRTEM images further confirm that the nanotubes have the polycrystalline perovskite structure.

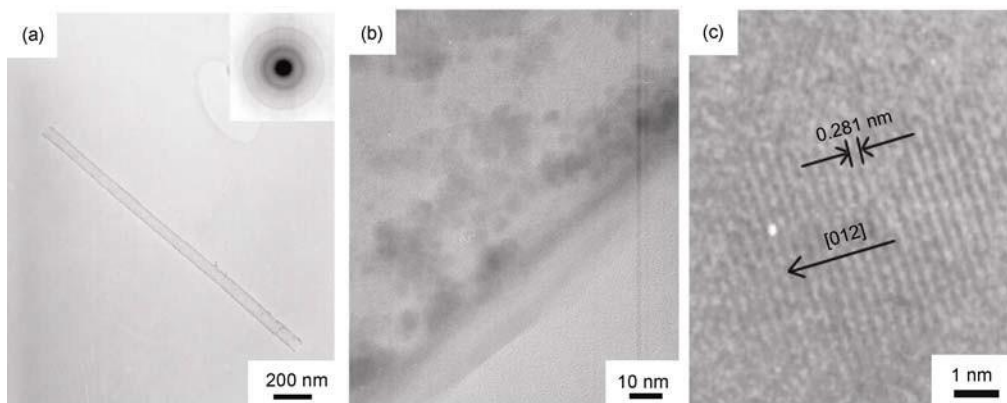


**Figure 2** TEM images of BFO nanotubes. (a)  $\times 10k$ , the inset is the corresponding SAED image; (b)  $\times 400k$ ; (c) HRTEM image.

### 3.3. XPS characterization of BFO nanotubes

Figure 3(a) shows the XPS spectrum of BFO nanotubes, which indicates the existence of Bi, Fe and O in the BFO nanotubes. Figure 3(b) shows the high-resolution spectrum of Fe 2p in the BFO nanotubes. In this figure, the strong peak of 710.51 eV and the peak of 724.0 eV attributed to  $\text{Fe}^{3+}$  can be observed. This indicates that in the BFO nanotubes the Fe element exists in the oxidation state of  $\text{Fe}^{3+}$  without  $\text{Fe}^{2+}$ , further demonstrating that the synthesized BFO nanotubes are in the pure phase.

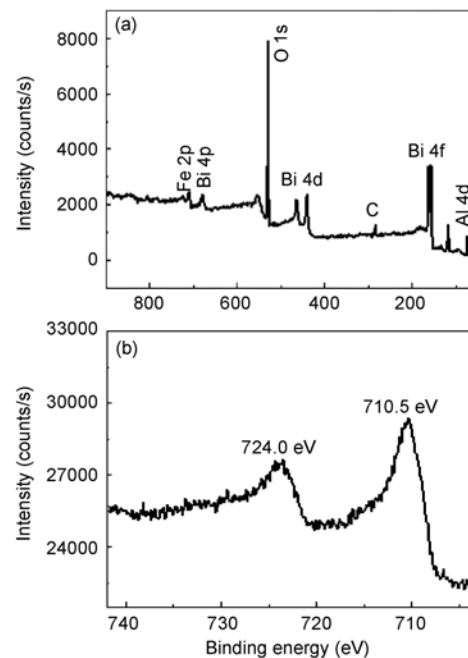


**Figure 3** XPS spectrum of BFO nanotubes. (a) Survey scan spectrum; (b) high-resolution scan of Fe 2p.

### 3.4. TEM characterization of Y-junction BFO nanotubes

Figure 4(a) shows the *cross-section* SEM image of the empty Y-junction channel AAO membrane. It is noticeable that the Y-junction channel AAO membrane has two layers, which is attributed to the voltage change in the manufacture process. The pore diameter is proportional to the anodization voltage. Hence the diameter reduces from about 100 nm to about 70 nm with decreasing the anodization voltage from 50 to 35 V. In order to maintain the total anodization area of the template, almost all pores branched into two in smaller diameter pores[18]. Figure 4(b) shows the Y-junction BFO nanotubes. These nanotubes perfectly copy the structure of the membrane.

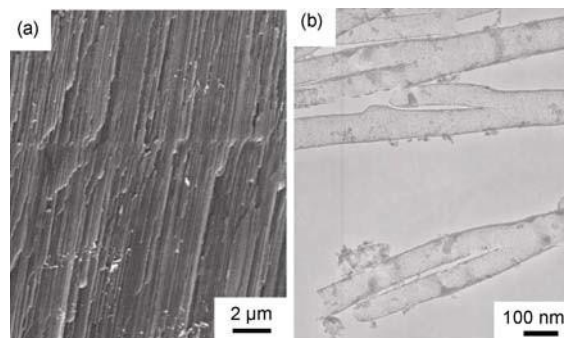


**Figure 4** (a) Cross-section SEM image of the Y-junction channel AAO membrane; (b) TEM image of Y-junction nanotubes.

#### 4. Conclusions

In conclusion, as-prepared multiferroic BFO Nanotube arrays were synthesized by the sol-gel method utilizing the AAO membrane technique. The structural characterization indicates that the BFO nanotubes have the polycrystalline microstructure. More interestingly, novel Y-junction BFO nanotubes were successfully synthesized based on the fabrication of Y-junction channel AAO membranes.

#### References

- [1] S. E. Jasim, M. A. Jusoh, R. Jose, *Exp. Theo. NANOTECHNOLOGY* 3 (2019) 65
- [2] Kumar M M, Palkar V R, Srinivas K, et al. Ferroelectricity in a pure BiFeO<sub>3</sub> ceramic. *Appl Phys Lett*, 2000, 76(19): 2764 – 2766
- [3] Palkar V R, John J, Pinto R. Observation of saturated polarization and dielectric anomaly in magnetoelectric BiFeO<sub>3</sub> thin films. *Appl Phys Lett*, 2002, 80(9): 1628 – 1630
- [4] Kimura T, Kawamoto S, Yamada I, et al. Magnetocapacitance effect in multiferroic BiMnO<sub>3</sub>. *Phys Rev B*, 2003, 67(18): 180401
- [5] Son J Y, Kim B G, Kim C H, et al. Writing polarization bits on the multiferroic BiMnO<sub>3</sub> thin film using Kelvin probe force microscope. *Appl Phys Lett*, 2004, 84(24): 4971 – 4973
- [6] Kimura T, Goto T, Shintani H, et al. Magnetic control of ferroelectric polarization. *Nature*, 2003, 426(6): 55 – 58
- [7] Park T-J, Mao Y B, Wong S S. Synthesis and characterization of multiferroic BiFeO<sub>3</sub> nanotubes. *Chem Commun*, 2004, 23: 2708 – 2709
- [8] P. Y. Feng, L-Q. Fa, C-G. Wang, *Exp. Theo. NANOTECHNOLOGY* 3 (2019) 169
- [9] Zhang X Y, Lai C W, Zhao X, et al. Synthesis and ferroelectric properties of multiferroic BiFeO<sub>3</sub> nanotube arrays. *Appl Phys Lett*, 2005, 87(14): 143102
- [10] Wei J, Xue D S, Xu Y. Photoabsorption characterization and magnetic property of multiferroic BiFeO<sub>3</sub> nanotubes synthesized by a facile sol-gel template process. *Scripta Mater*, 2008, 58: 45 – 48
- [11] Gao F, Yuan Y, Wang K F, et al. Preparation and photoabsorption characterization of BiFeO<sub>3</sub> nanowires. *Appl Phys Lett*, 2006, 89(10): 102506
- [12] Tenne R, Margulis L, Genut M, et al. Polyhedral and cylindrical structures of tungsten disulphide. *Nature*, 1992, 360(6403): 444 – 446

- [13] Zhang W X, Wen X G, Yang S H, et al. Single-crystalline scroll-type nanotube arrays of copper hydroxide synthesized at room temperature. *Adv Mater*, 2003, 15(10): 822–825
- [14] Steinhart M, Wendorff J H, Greiner A, et al. Polymer nanotubes by wetting of ordered porous template. *Science*, 2002, 296: 1997
- [15] Hua Z H, Chen R S, Li C L, et al. CoFe<sub>2</sub>O<sub>4</sub> nanowire arrays prepared by template-electrodeposition method and further oxidization. *J Al- loys Compd*, 2007, 427: 199–203
- [16] Sui Y C, Gonzalez-Leon J A, Bermudez A, et al. Synthesis of multi branched carbon nanotubes in porous anodic aluminum oxide tem- plate. *Carbon*, 2001, 39: 1709–1715
- [17] Tian Y T, Meng G W, Biswas S K, et al. Y-branched Bi nanowires with metal-semiconductor junction behavior. *Appl Phys Lett*, 2004, 85(6): 967–969
- [18] S. Chernkov, P. Badov, *Exp. Theo. NANOTECHNOLOGY 3 (2019) 175*



## Numerical investigation of heat transfer augmentation in curved channel using hybrid nanofluids

A. M. Ahmed Alwaise<sup>1</sup>, M. Ibrahim Alwiase<sup>2</sup>, A.Y. Qasim<sup>3</sup>

<sup>1</sup>University of Mosul, Collage of Petroleum and mining Engineering, Reservoir Engineering Department, Mosul, Iraq

<sup>2</sup>University of Nineveh, Collage of Electronics Engineering, Mosul, Iraq

<sup>3</sup>Commission of research and Industrial Development- Iraq

E-Mail: [Ayad\\_waise@yahoo.com](mailto:Ayad_waise@yahoo.com)

*Received: 22/2/2019 / Accepted: 12/10/2020 / Published: 1/4/2020*

Convective heat transfer can be enhanced by changing flow geometry and/or by enhancing thermal conductivity of the fluid. In this work, CFD modelling of horizontal straight and curved channel with square cross section were presented to investigate the effect of hybrid nanofluids on turbulent forced convective heat transfer. This study proposes simultaneous passive heat transfer enhancement by combining the geometry effect using 0.1% graphene nanoplatelets-silver hybrid nanofluids (GNP–Ag) inflow in straight and curved channel. The results showed that the average Nusselt number is generally higher for curved channel with hybrid nanofluid when compared with straight square channel. Moreover, for 0.1% of GNP–Ag hybrid nanofluid improvement is 22.61% and 34.78% for straight channel and 27.43% and 39.52 for curved channel at the Reynolds number of 5,000 and 17,500, respectively.

**Keywords:** Heat transfer; turbulent flow; hybrid nanofluid; curved channel; straight channel.

### 1. Introduction

According to the importance of energy in the world, so far, many attempts have been made to increase energy efficiency [1, 2]. One way is the use of fluids with higher heat transfer coefficient, by the addition of metal, non-metal and metal oxide particles with higher thermal conductivity into conventional fluids. Development of fluids thermal properties leads to more energy efficient, smaller size, lighter weight and lower operational costs for thermal systems like heat exchangers. The particles added to the base fluid should be in nanometer size, because the

larger particles and cause problems such as erosion, sedimentation, clogging and higher fluid resistance. Masuda et al.[3] and Choi et al. [4] were the first raised the idea of using nanofluids. Bergman [5] investigated the effects of increasing thermal conductivity and reducing the specific heat of the nanofluid relative to the base fluid and quantified heat transfer enhancement. They show that use of nanofluid instead of pure liquids can either enhance or degrade thermal performance.

In the recent years, significant investigations on the use of carbon-based nanomaterials such as, single-wall carbon nanotube, multi-wall carbon nanotube, graphene oxide and graphene nanoplatelets (GNP) to make nanofluids were reported in the literature [6-8]. New research indicates that graphene nanofluids could provide higher thermal conductivity enhancement in comparison to other tested nanofluids. Graphene particles have better thermal conductivity and also higher mechanical strength, and electrical conductivity. Favourable thermo-physical properties of graphene has made it an excellent candidate for use in nanofluids [9]. In addition, synthesizing graphene nano- articles is relatively easy and cost effective. Small variation of properties of graphene has been reported due to different methods used to manufacture one layer or multi-layer graphene such as, exfoliation of graphene oxide layer, deposition with chemical vapor and mechanical cleavage, etc. [9-11].

Channels with non-circular geometry are usually excluded from many applications. For one reason, this kind of ducts has very low rate of heat transfer. On the other hand, the pressure drop in non-circular cross sections is much less than that compared to circular cross sections. It should be stressed that the friction factors in rectangular and circular tubes equal to  $56.92/Re$  and  $64/Re$ , respectively. Therefore, heat transfer enhancement of the channels with non-circular ducts can result in its wide applications in different industries. Furthermore, they have other advantages such as high compaction in comparison with other kind of channels, high mechanical resistivity, easy forming using thin metal, and low-pressure drop, triangular and square ducts which make them beneficial to be utilized in compact heat exchangers, combustion engines, boilers, nuclear reactor and energy recovery equipment, furnaces, rockets, medical and electronics industries. Due to the importance of low-pressure drop in these applications, heat transfer enhancement can open up great opportunists [17].

Considering the literature review about nanofluids, the aim of this study is to investigate and compare the heat transfer enhancement of graphene nanoplatelets–silver hybrid nanofluids (GNP–Ag) through the straight and curved channel with square cross-section in the turbulent flow regimes under constant heat flux boundary condition for the wall.

## 2. Numerical Model

The computational domains were created in Free CAD as shown in Fig.1; the length of the copper channel is 500mm and the height and width are 2mm. The commercial pre-processor software GAMBIT 2.3.16 was used for meshing, labelling boundary conditions and determines the computational domain. Three different meshes,  $1 \times 10^5$ ,  $2 \times 10^5$ , and  $4 \times 10^5$ , were tested and compared in terms of the local pressure, velocities, and temperature to ensure a mesh independent solution. It is found that mesh number of around  $2 \times 10^5$  gives about 1% deviation compared to mesh size of  $4 \times 10^5$ ; whereas the results from mesh number of  $1 \times 10^5$  deviate by up to 8% compared to those from the finest one. Therefore, a mesh of around  $2 \times 10^5$  ( $20 \times 20 \times 500$ ) elements was considered sufficient for the numerical investigation purposes; a fine structured mesh near the wall to resolve the boundary layer and an increasingly coarser mesh in the middle of the channel to reduce the computational cost.

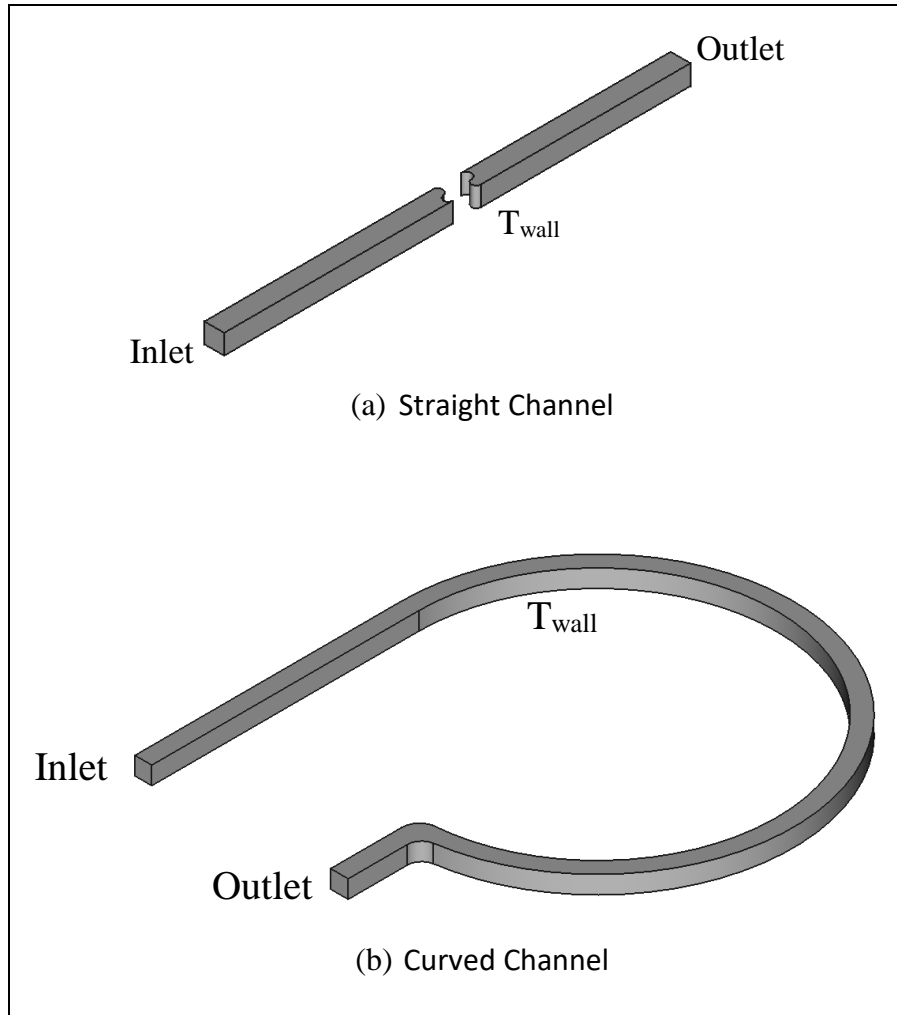


Fig. 1 Shapes of straight and curved channel

### 2.1 Governing equations

The realizable  $k-\varepsilon$  turbulence model with wall heat treatment is used for turbulent flow simulation. The Realizable turbulence model by Shih et al.[12] is the most sophisticated model newly of the three  $k-\varepsilon$  differences and characteristics two main variations from the standard  $k-\varepsilon$  model. It utilizes a new equation for the turbulent viscosity equation and derived the dissipation rate transport equation from the mean-square vorticity fluctuation equation. Turbulent kinetic energy,  $k$ , and turbulent dissipation rate,  $\varepsilon$ , are combined to the governing equations using the relation of the turbulent viscosity  $\mu_t = \rho C_\mu K^2 / \varepsilon$ , where  $C_\mu = 0.09$  and the following values have been assigned as an empirical constant:  $C_2 = 1.9$ ,  $\sigma_\tau = 0.85$ ,  $\sigma_\kappa = 1.0$ , and  $\sigma_\varepsilon = 1.2$ .

$$k = \frac{3}{2} (u.I)^2, \varepsilon = C_\mu^{3/4} \frac{k^{3/2}}{L} \tag{1}$$

Furthermore, the character  $L$ . in Eq. 6 refer to the turbulent characteristic length scale, which is set to be  $0.07(d/2)$  in the current study. As well as the factor of  $0.07$  been adopted based on the maximum value of the mixing length in fully developed turbulent pipe flow. For an initial guess of turbulent quantities ( $k$  and  $\varepsilon$ ), the turbulent intensity ( $I$ ) was specified. Where the turbulent intensity for each case can be calculated based on the Eq. 2. [13].

$$I = 0.16 \times \text{Re}^{-1/8} \quad (2)$$

ith regards to the nanofluid, infinitesimal (less than 100 nm) solid particles assumed to be able using single phase approach, so single phase approach adopted for nanofluid modelling. For all these assumptions, the dimensional conservation equations for steady state mean conditions are as follows: continuity, momentum and energy equations.[14].

$$\frac{\partial u}{\partial x} + \frac{1}{r} \frac{\partial}{\partial r} (r \rho_{nf} u) = 0 \quad (3)$$

$$u \frac{\partial u}{\partial x} + v \frac{\partial}{\partial r} (\rho_{nf} u) = -\frac{\partial p}{\partial x} + \frac{1}{r} \frac{\partial}{\partial r} \left[ r(v + \varepsilon_H) \frac{\partial u}{\partial r} \right] \quad (4)$$

$$\frac{1}{r} \frac{\partial}{\partial r} (\rho u T) = \frac{1}{r} \frac{\partial}{\partial r} \left[ r(\alpha + \varepsilon_H) \frac{\partial T}{\partial r} \right] + \frac{1}{r^2} \frac{\partial}{\partial x} \left\{ \frac{k_{nf}}{C_p} \frac{\partial T}{\partial x} \right\} \quad (5)$$

### 3. Thermo-physical properties of hybrid nanofluids

The thermo-physical properties of graphene nanoplatelets–silver hybrid nanofluids (GNP–Ag) in this study such as thermal conductivity ( $k_{nf}$ ) and viscosity ( $\mu_{nf}$ ) have been obtained from the experimental study of [15] as shown in Fig. 2 and Fig. 3. Meanwhile, the density ( $\rho_{nf}$ ) and specific heat capacity ( $C_{nf}$ ), of nanofluid have been obtained by the relation [16].

$$\rho_{nf} = \left( \frac{\phi}{100} \right) \rho_p + \left( 1 - \frac{\phi}{100} \right) \rho_f \quad (6)$$

$$C_{nf} = \frac{\frac{\phi}{100} (\rho C)_p + \left( 1 - \frac{\phi}{100} \right) (\rho C)_f}{\rho_{nf}} \quad (7)$$

Because the single-phase fluid Nusselt number correlations underestimate the heat transfer of nanofluids, the researchers have developed new Nusselt number correlations for nanofluids. Some of the available Nusselt number correlations are outline here:

Forced convection heat transfer coefficient under turbulent flow could be estimated by Dittus-Boelter [17] Eq. 8.

$$Nu = \frac{h_f}{k_f} D = 0.023 \text{Re}^{0.8} \text{Pr}^{0.4} \quad (8)$$

Maiga et al. [18] presented equation for evaluation of Nusselt number for nanofluids as a function of Re and Pr:

$$Nu = 0.085 \text{Re}^{0.71} \text{Pr}^{0.35} \quad (9)$$

The available friction factor expression for water and nanofluids are represented by Eq. (10) Blasius [19] presented equation for evaluation of friction factor for water flow;

$$f=0.316Re^{-0.25} \tag{10}$$

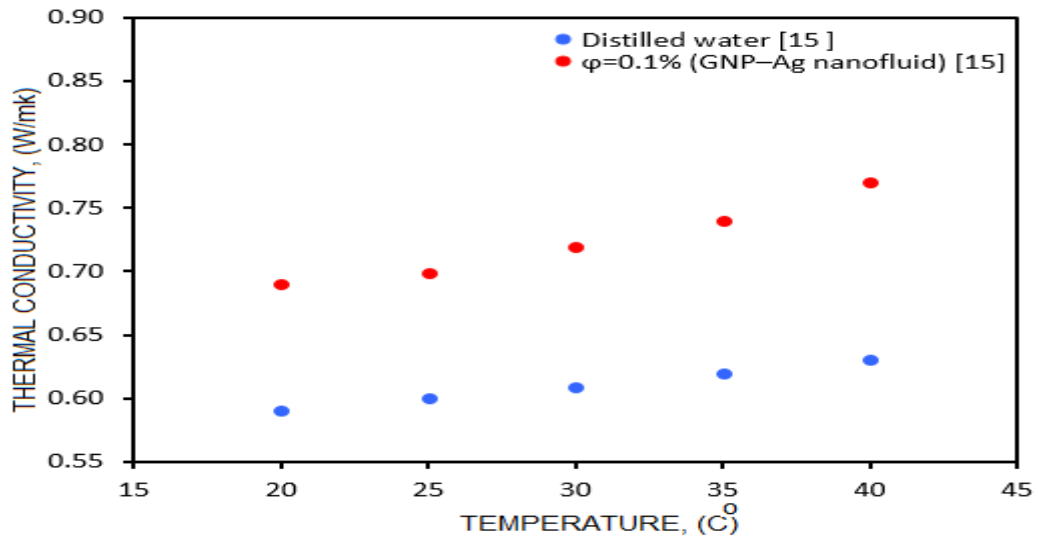


Fig. 2 Thermal conductivity of the GNP-Ag nanofluid.

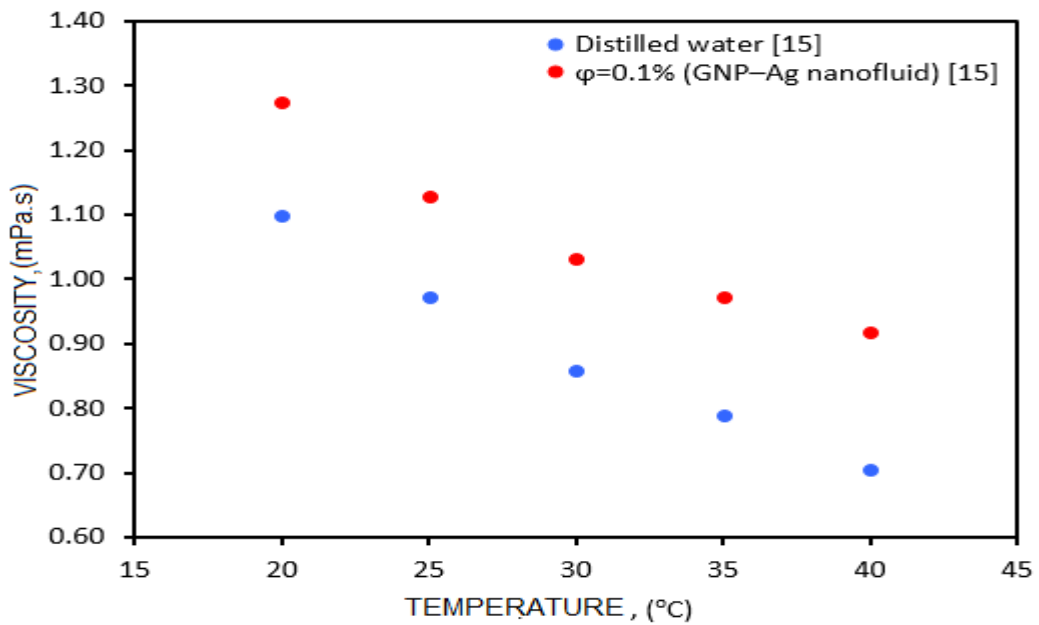
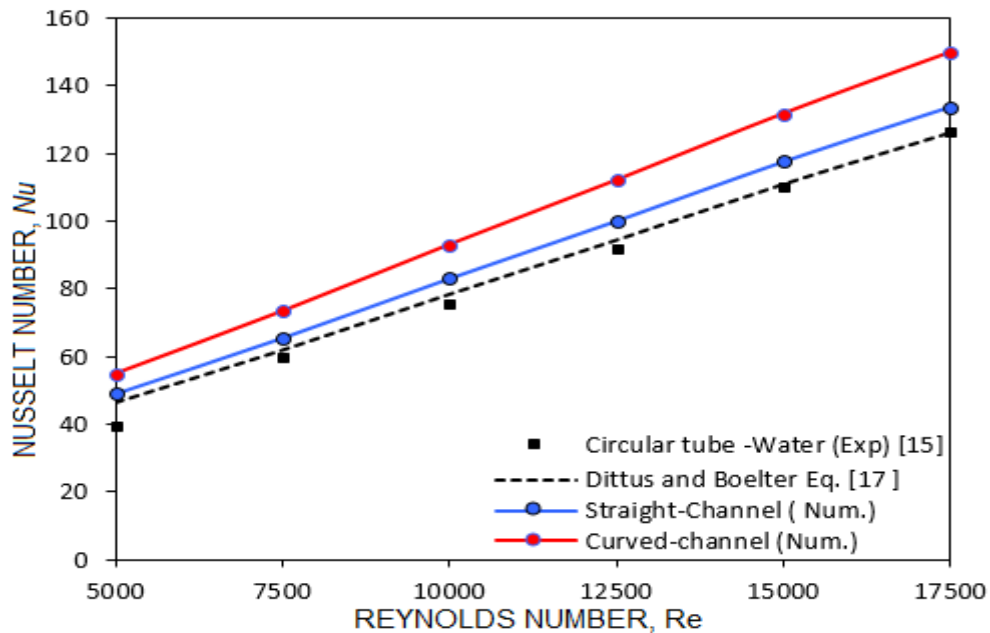


Fig. 3 Viscosity of the GNP-Ag nanofluid.

#### 4. Results and discussion

One of the key factors that determine the heat transfer performance is the cross-sectional tube geometry. This study examines straight and curved channel with square cross section. In order to validate the numerical procedure, a set of data was obtained with water as the working fluid. Comparison of the numerically measured Nusselt number for water with correlations of Dittus and Boelter [17] are presented in Fig. 4. This figure shows that the numerical results are in good agreement with the empirical correlations for turbulent flows. The maximum deviation between the present data and the existing correlations for Nusselt number is about  $\pm 5.3\%$ , which validates the numerical procedure. Nanofluids with 0.1% weight concentrations of functionalized GNP–Ag are then tested in straight and curved channel. The results reveal that the Nusselt number enhances with increase of Reynolds number at 0.1% nanoparticles concentration as shown in Fig. 5. This is because the nanofluid contains suspended nanoparticles, which have higher conductivity compared to the base fluid. The Nusselt number enhancement for GNP–Ag nanofluid is also attributed to thermophysical properties of the nanoparticles as well as particle Brownian motion. Moreover, for 0.1% of GNP–Ag hybrid nanofluid improvement is 22.61% and 34.78% for straight channel and 27.43% and 39.52 for curved channel at the Reynolds number of 5,000 and 17,500, respectively.



**Fig. 4** Nusselt number for water in straight and curved channel.

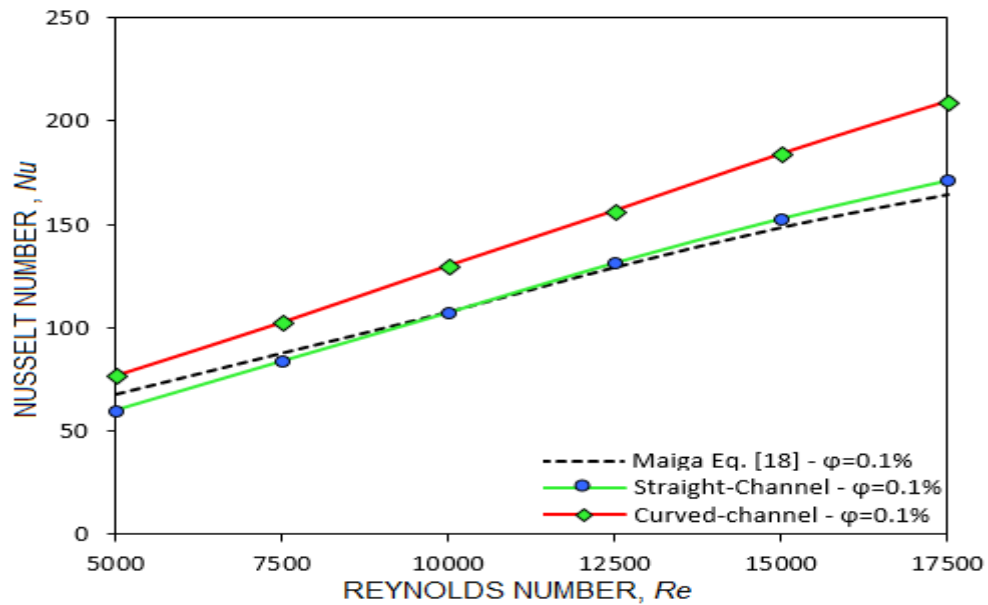


**Fig. 5** Nusselt number for nanofluid in straight and curved channel.

Fig. 6 shows the numerical friction factor for the base fluid in straight and curved channel comparing to the experimental result of a circular tube by [15] and thermotical data of Blasius equation (10) [19]. A maximum deviation of 5% is obtained between theoretical data and numerical data. Moreover, Fig.7 shows the numerical friction factor of GNP–Ag nanofluids in straight and curved channel. Nevertheless, Blasius equation (10) [19]. is used for estimating the friction factor of GNP–Ag nanofluids at 0.1% weight concentration and the result is illustrated in Fig. 7. The improvement of friction factor for 0.1% weight concentration of GNP–Ag nanofluid is 9.2% for curved channel at the Reynolds number of 17,500. The enhancement of friction factor due to the suspended of GNP–Ag nanoparticles in the base fluid is not significant in comparison to the heat transfer enhancement.

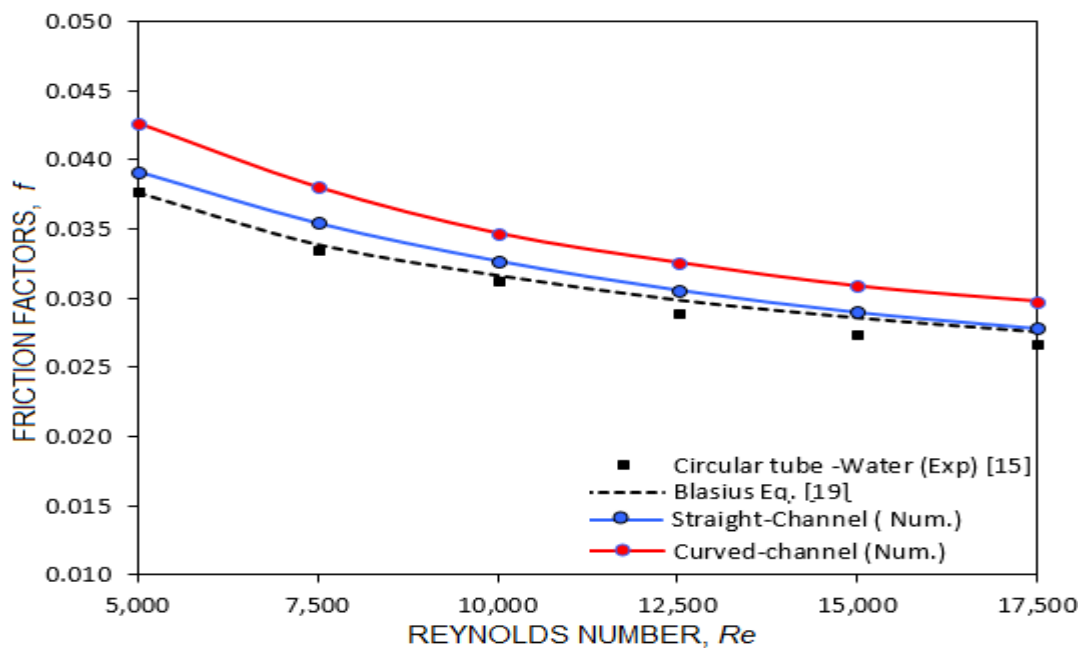


**Fig. 6** Friction factor for water in straight and curved channel.

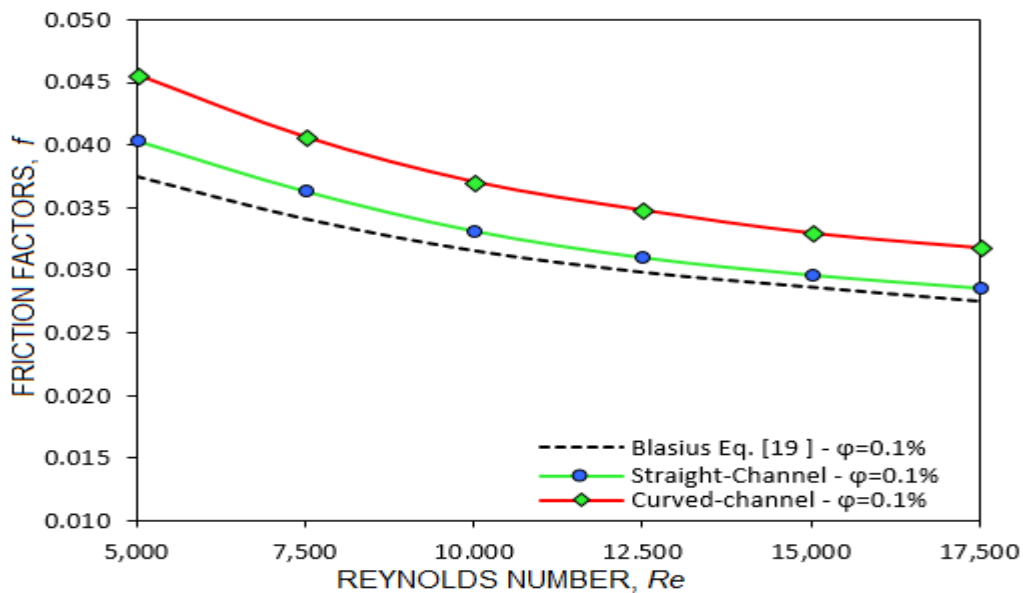


**Fig. 7** Friction factor for nanofluid in straight and curved channel comments and response.

## 5. Conclusions

A computational study was conducted to investigate the turbulent flow heat transfer performance of straight and curved channel with square cross section with water and GNP–Ag hybrid nanofluids. It is found that adding 0.1% nanoparticle volumetric concentration improves heat transfer performance for straight and curved channel. However, higher amounts of nanoparticles are not recommended. In- curved channel gives better performance than straight channel for nanofluids. The Nusselt number is enhanced in comparison to the base fluid. For 0.1% of GNP–Ag hybrid nanofluid improvement is 22.61% and 34.78% for straight channel and 27.43% and 39.52 for curved channel at the Reynolds number of 5,000 and 17,500, respectively. The increase of friction factor is negligible when compare to the advantages of heat transfer enhancement. The developed Nusselt number and friction factor correlations are proposed. Future study will evaluate various modeling approaches for nanofluid heat transfer, e.g., two-phase mixture, Euler-Euler, and Euler-Lagrange models, in coils with respect to the effect of secondary flow to the nanoparticle concentration.

## Reference

- [1] B. Klause, G. Bremene, V. Hernn, A. Bosch, Theo. Exp. NANOTECHNOLOGY 2 (2019) 193
- [2] Cortés, C., L.I. Díez, and A. Campo, *Efficiency of composite fins of variable thickness*. International Journal of Heat and Mass Transfer, 2008. **51**(9): p. 2153-2166.

- [3] Masuda, H., Ebata, A., Teramae, K., Hishinuma, N., *Alteration of thermal conductivity and viscosity of liquid by dispersing ultra-fine particles*. Netsu Bussei, 1993. **7**(4): p. 227-233.
- [4] Choi, S., *Enhancing thermal conductivity of fluids with nanoparticles*. ASME-Publications-Fed, 1995. **231**: p. 99-106.
- [5] N. Nabel, F. Gerous, Theo. Exp. NANOTECHNOLOGY 2 (2019) 201
- [6] Yu, W., H. Xie, and D. Bao, *Enhanced thermal conductivities of nanofluids containing graphene oxide nanosheets*. Nanotechnology, 2009. **21**(5): p. 055705.
- [7] Zheng, R., et al., *Thermal percolation in stable graphite suspensions*. Nano letters, 2011. **12**(1): p. 188-192.
- [8] Ding, Y., et al., *Heat transfer of aqueous suspensions of carbon nanotubes (CNT nanofluids)*. International Journal of Heat and Mass Transfer, 2006. **49**(1-2): p. 240-250.
- [9] Novoselov, K.S., et al., *Electric field effect in atomically thin carbon films*. science, 2004. **306**(5696): p. 666-669.
- [10] Land, T., et al., *STM investigation of single layer graphite structures produced on Pt (111) by hydrocarbon decomposition*. Surface Science, 1992. **264**(3): p. 261-270.
- [11] Tung, V.C., et al., *High-throughput solution processing of large-scale graphene*. Nature nanotechnology, 2009. **4**(1): p. 25.
- [12]. C. Tedlle, N. Chen, I. Pero, Exp. Theo. NANOTECHNOLOGY 3 (2019) 115
- [13] ANSYS, *ANSYS FLUENT V15 Theory Guide*. ANSYS Inc., USA, 2015.
- [14] Bejan, A., *Porous and complex flow structures in modern technologies*. 2004: Springer.
- [15] Yarmand, H., et al., *Graphene nanoplatelets–silver hybrid nanofluids for enhanced heat transfer*. Energy conversion and management, 2015. **100**: p. 419-428.
- [16] Korada, V.S., *Laminar convective heat transfer and friction factor of Al<sub>2</sub>O<sub>3</sub> nanofluid in circular tube fitted with twisted tape inserts*. International Journal of Automotive and Mechanical Engineering (IJAME), 2011. **3**(Jan-June 2011): p. 265-278.
- [17] C. S. da Laz, A. D. A. dos Santos, D. R. Izario, Exp. Theo. NANOTECHNOLOGY 3 (2019) 123
- [18] Maiga, S.E.B., et al., *Heat transfer enhancement by using nanofluids in forced convection flows*. International Journal of Heat and Fluid Flow, 2005. **26**(4): p. 530-546.
- [19] D.B. Devedov, R.J. Asherov, G.H. Glenko, N.O. Ferstaloja, Exp. Theo. NANOTECHNOLOGY 3 (2019) 131



## **Cytotoxicity and apoptotic activity of magnesium orotate nanoparticles towards human hepatoma cell line HepG<sub>2</sub>**

A. Hassani<sup>1</sup>, S.A. Hussain<sup>1,\*</sup>, N. Abdullah<sup>1</sup>, S.Kmaruddin<sup>1</sup>, M.K.Alomar<sup>2</sup>, A. Rasedee<sup>3</sup>, M. Al-Qubaisi<sup>3</sup>, R. Rosli<sup>3</sup>

<sup>1</sup>Department of Chemical and Environmental Engineering, Faculty of Engineering, Universiti Putra Malaysia, Serdang, UPM, Serdang 43400, Malaysia.

<sup>2</sup>Department of Civil Engineering, Al-Maaref University College, Ramadi, 31001, Iraq.

<sup>3</sup>Institute of Bioscience, Universiti Putra Malaysia, Serdang, UPM, Serdang 43400, Malaysia.

Email: [aslina@upm.edu.my](mailto:aslina@upm.edu.my)

*Received:* 1/3/2019 / *Accepted:* 28/7/2020 / *Published:* 1/4/2020

The purpose of this study was to enhance the therapeutic effect of magnesium orotate (MO) via loading it to gum arabic nanocarrier. The magnesium orotate-loaded gum arabic nanoparticles (MOGANPs) were prepared by high pressure homogenizer. The freeze-dried powder of nanoparticles was characterized using X-ray Diffractometry (XRD) and Transmission Electron Microscopy (TEM). The obtained nanoparticles were spherical in shape with diameters ranged from 30 to 50 nm. The cytotoxicity of MOGANPs was determined against human hepatocellular carcinoma HepG<sub>2</sub> cell line using 3-(4,5-dimethylthiazol-2-yl) 2,5-diphenyl tetrazolium bromide (MTT) assay which showed an enhanced efficacy of MO nano-carried with gum arabic when compared to pure compound alone. Moreover, the results revealed that MOGANPs induced apoptosis in the treated HepG<sub>2</sub> cells and thus it is promising formulation, in addition, further anticancer studies are needed.

**Keywords:** Magnesium orotate; Gum; Liver cancer; Cytotoxicity.

### **1. Introduction**

Recently, there has been renewed interest of research and applications of nanoparticles due to their capacity of reducing toxicity of chemotherapeutic agents [1-4]. The main advantages of nanoparticles is the improvement of efficacy of drugs towards human cells and diagnostic of diseases such as the use of gadolinium nanoparticles for theranostic applications [5-12]. Due to the rapidly developing domain of nanomedicine, many bioactives loaded nanocarriers systems are

under investigation to reduce toxicity for cancer therapy [13-15]. Magnesium orotate is a complex of magnesium and orotic acid. A recent study has reported the antitumor and anti-inflammatory effects of orotic acid. Researchers attempted to evaluate the impact of magnesium orotate on cancer therapy [16]. Gum arabic (GA) also known as *acacia gum*, enhanced the *in vivo* stability of nanoparticles [17]. The MOGANPs nanoparticles were characterized using (XRD), (TEM), and cell cycle arrest was determined using cytometry analysis.

## 2. Methods of analysis

### 2.1. Characterization of MOGANPs nanoparticles

X-ray diffractogram patterns were recorded using  $\text{CuK}\alpha$  radiation,  $\lambda$  1.5406 Å at  $2\theta = 20^\circ$ - $60^\circ$  and scan speed of  $2^\circ$  per minute. Transmission electron microscopy was carried out to visualise the morphology, size distribution, and determine the homogeneity of nanoparticles.

### 2.2. MTT Assay

Two hundred microliters at a concentration of  $1 \times 10^5$  cells/mL of cancer cell line suspension was added to each well of a 96-well plate and incubation for 24 h. After that, the cells were treated with MO and MOGANPs at various concentration of 1.56-100  $\mu\text{g/mL}$  then incubation for 72h at  $37^\circ\text{C}$  in 5%  $\text{CO}_2$ . Then, 20  $\mu\text{l}$  of 5mg/mL of MTT solution was added to each well. The plate was then incubated for 4 h at  $37^\circ\text{C}$  in 5%  $\text{CO}_2$  until formazan product was developed. The absorbance readings were recorded at 570 nm using ELISA reader.

### 2.3. Cell cycle analysis

The HepG2 cells were seeded at  $1 \times 10^6$  cells/well for 24 h in a 6-well plate. The cells then were treated 12.5 and 25  $\mu\text{g/mL}$ . After that, 250  $\mu\text{L}$  of trypsin buffer solution was added to the tubes including harvested cells and incubation for 10 min at room temperature. 200  $\mu\text{L}$  of trypsin inhibitor and RNase buffer was further added to each tube and incubation for 10 min. 200  $\mu\text{L}$  of PI stain solution was added then followed by incubation in the dark for 10 min. The PI fluorescence was measured under 620-640 nm excitation using flow cytometry analysis.

### 2.4. Statistical Analysis

The analysis of variance was carried out using the ANOVA technique ( $p < 0.05$ ).

## 3. Experimental analysis

The preparation of MOGANPs nanoparticles was performed using freeze-drying method in 1: 1 molar ratio by dissolving 0.94g of MO in 50 mL of deionized water under mild agitation for 20 min. MO solution was added dropwise to GA solution with vigorous under stirring for 72 h. The dispersion was subjected to a high pressure homogeniser (Avestin Canada) at a pressure of 1000 bar for seven cycles followed by freeze-dried for 72 h.

## 4. Results and discussion

### 4.1. X-ray Diffraction

The patterns of MO, GA, Physical mixture, and MOGANPs nanoparticles are depicted in figure 1. A sharp diffraction peaks were revealed at several diffraction angles  $25.94^\circ$ ,  $27.96^\circ$ , and  $37.82^\circ$ , illustrating the crystalline nature of MO. The MO peaks were totally vanished due to the complexation that happened between MO and GA (figure 1d).

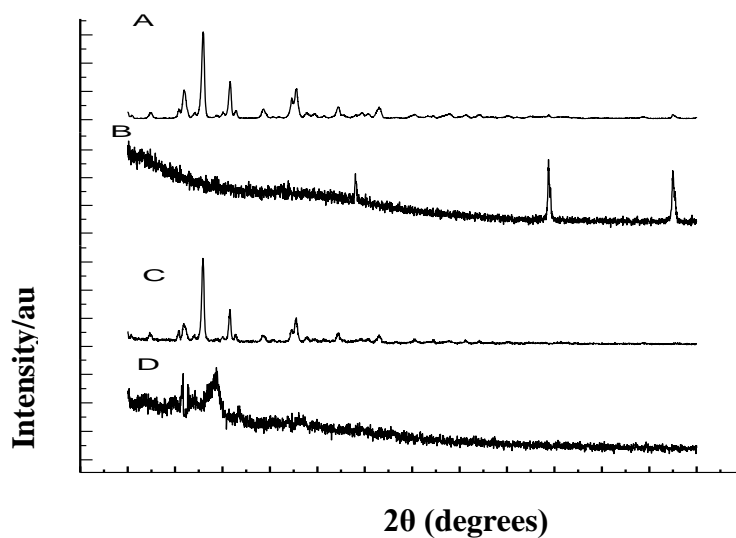


**Fig.1** X-ray diffractogram: ( A) MO, ( B ) GA, ( C) physical mixture,(D) MOGANPs

#### 4.2. Transmission Electron Microscopy (TEM)

Nanoparticle prepared presents approximately spherical elliptical shape as individual particles with narrow size distribution ranging from 21 to 45nm.

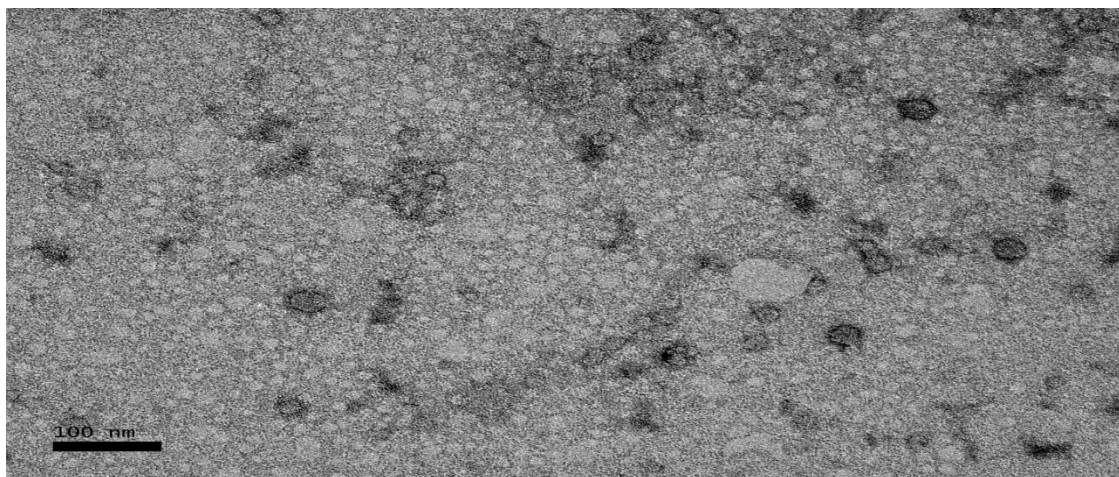


**Fig 2.** Transmission electron microscopy of MOGANPs nanoparticles

#### 4.3. Cytotoxicity assay

The anticancer activity of MOGANPs was slightly higher than the free MO due to the galactose group of GA polymer [18] ( $p$  value < 0.05).

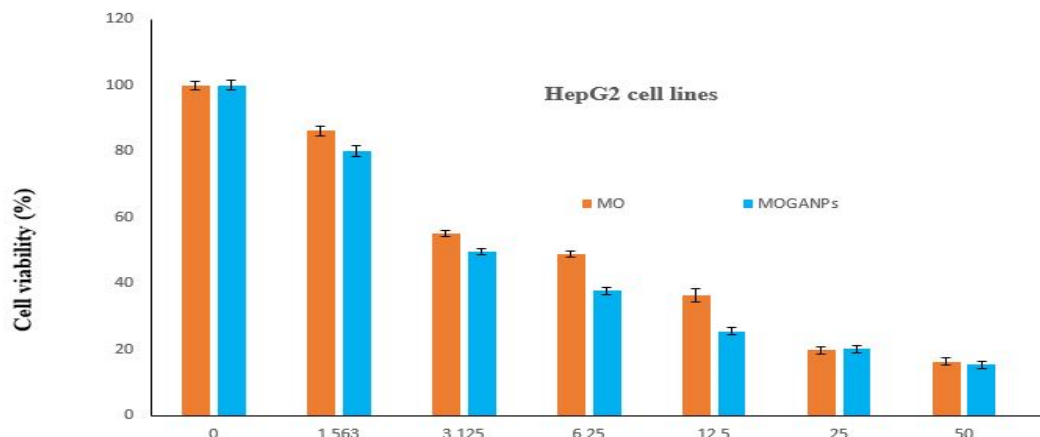


**Fig.3** Cytotoxicity activity of MO, MOGANPs exposed to HepG2 cell lines

**Table 1** IC<sub>50</sub> ( μg/mL ) values of MO and MOGANPs nanoparticles on HepG2

Cell lines	MO	MOGANPs
HepG2	24.20 ±0.1	12.08±0.2

#### 4.4. Induction of cell cycle analysis by MO and MONPs nanoparticles

MOGANPs nanoparticles at 12.5 μg/mL increased both G<sub>0</sub>/G<sub>1</sub> (7%) and S arrest (19%) in addition to reduce the total number of cells in G<sub>2</sub>/M phase which had 28 % decrease when compared to control. Moreover, MOGANPs nanoparticles induced apoptosis which had 13.9-fold increase at 12.5 μg/mL, and 28-fold increase at 25.0 μg/mL, when compared to control. For 24-hour treatment, MOGANPs nanoparticles at 25.0 μg/mL induce G<sub>0</sub>/G<sub>1</sub> arrest which had 13% increase, and 53% and 26% decrease at S and G<sub>2</sub>/M phases, respectively when compared to control (Figure 4). Also, pure MO dissolved in DMSO induced apoptosis which had 1410 % increase at 12.5 μg/mL, and 1926 % increase at 25.0 μg/mL when compared to control.

For 24-hour treatment, MO induced G<sub>0</sub>/G<sub>1</sub> arrest which had 8 % decrease at 12.5 μg/mL, and 3% decrease at 25.0 μg/mL when compared to control. MO showed no significant effect ( $p \geq 0.05$ ) on the cell cycle at S-phase in HepG2 cancer cells after treatment with both 12.5 and 25.0 μg/mL when compared to control. Besides, MO reduced cell numbers at G<sub>2</sub>/M which had 30 % decrease at 12.5 μg/mL, and 67 % decrease at 25.0 μg/mL, when compared to control (Figure

4).

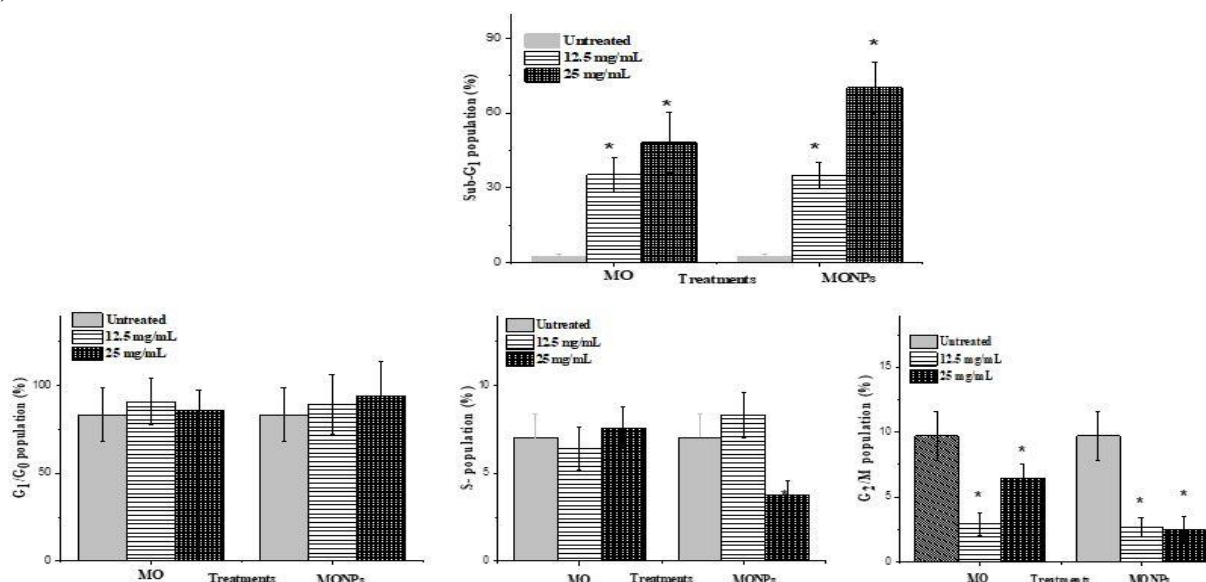


**Fig 4** Effect of MOGANPs nanoparticles and MO ( $IC_{50}$  values) on cell cycle distribution of HepG2 liver cancer cells determined by flow cytometry

## 5. Conclusion

The results confirmed the incorporation of MO into GA cavity. This study has found that MOGANPs nanoparticles can be considered as a potential candidate compound for the evaluation of prevention and cancer treatment. Thus, MO, either pure or MONPs, had effect on cell cycle of HepG2 cancer cell. However, the main cause of their antiproliferative activity on HepG2 cancer cell was apoptosis as it got the largest change when compared to other phases.

## Acknowledgment

The authors would like to acknowledge Universiti Putra Malaysia for awarding the funds to conduct this research under grant Vot No. GP-IPS/2016/9505500.

## References:

- [1] J. Shaikh, D. D. Ankola, V. Beniwal, D. Singh, Eur. J. Pharm. Sci 37(2009) 223
- [2] T. Duřvki, V. Saryviak, Exp. Theo. NANOTECHNOLOGY 3 (2019) 147
- [3] S. K. Sriraman, and V. P. Torchilin, Adv. Biomater. Biodevices (2014)79
- [4] M. S. Usman, M. E. El Zowalaty, and K. Shameli, Int. J. Nanomedicine 8(2013) 4467
- [5] A. J. Mieszawska, W. J. M. Mulder, and Z. A. Fayad, Mol. Pharm 10(2013) 831
- [6] S. Santra, C. Kaittanis, and O. J. Santiesteban, J. Am. Chem. Soc 133(2011)16680
- [7] Y. Wang et al, Am. Chem. Soc (2013)
- [8] Dalila MEKAM, Dalila MESRI, Habib. Rozale, Exp. Theo. NANOTECHNOLOGY 3 (2019) 159
- [9] F. Chen et al., ACS Nano 7(2013)9027

- [10] R. Kannan et al., JACS Commun (2006)11342
- [11] M. S. Usman, M. Z. Hussein, and S. Fakurazi, Nanomaterials 7(2017) 244
- [12] M. Ferrari, Nat. Rev. Cancer 5, (2005) 161–171, 2005.
- [13] P. Nasimi, and M. Haidari, Int. J. Green Nanotechnol 5(2013)1
- [14] M. G. Cascone, L. Lazzeri, and C. Carmignani, J. Mater, Sci. Mater. Med 3(2002)523
- [15] E. T. Baran, and C. De Azure, J. Mater, Sci. Mater. Med 3(2002)1113
- [16] J. E. Kipp, Int. J. Pharm 284(2004) 109
- [17] P. Sarika, and N. James, P. Kumar, Crbo.poly 134(2015)167
- [18] S. Ahmad, Exp. Theo. NANOTECHNOLOGY 3 (2019) 179

## ZnO-based sensors with controlled ethanol sensing

F. Y. Liu<sup>1</sup>, D. Z-H. Tong<sup>1</sup>, L. L. Tian<sup>2,\*</sup>

<sup>1</sup>Physics Department, Jilin University, Changchun 130012, China

<sup>2</sup>Superhard Materials Laboratory, Jilin University, Changchun 130012, China

\*) Email: [lltian@jlu.edu.cn](mailto:lltian@jlu.edu.cn)

*Received:* 10/12/2019 / *Accepted:* 5/3/2020 / *Published:* 1/4/2020

ZnO microcrystals are synthesized through a facile solution method and characterized by field-emission scanning electron microscopy, transmission electron microscopy, selected area electron diffraction and X-ray diffraction. The ethanol sensing properties of these microcrystals are investigated by spin-coating them on a silicon substrate with Pt electrodes to fabricate a micro-structure sensor. The sensitivity is up to 8 when the sensor is exposed to 50 ppm ethanol, and the response time and recovery time are 10 s and 20 s, respectively. A contact-controlled model is established to explain the sensing properties of the microcrystals, which provides another approach to realize high-performance gas sensors.

**Keywords:** ZnO, ethanol, micro-structure sensors, semiconducting metal oxides

1. **Introduction** Gas sensors play an important role in environmental protecting, chemical process controlling and air quality monitoring as well as personal safety[1–5]. Many semiconducting metal oxides have been employed for this application due to their small size, low cost and high compatibility with microelectronic processing[6]. The gas-sensing mechanism of these semiconducting metal oxides mainly involves a change in electrical resistance caused by the adsorption of gas on the sensor surface. Therefore the sensing properties are easily influenced by the micro-structural features, such as the grain size, crystal structure, geometry and connectivity between particles[6]. ZnO is a semiconducting metal oxide which has received a great deal of attention from researchers and industry alike[7–10]. Since the discovery in 1962 that the electrical conductivity of ZnO could be dramatically changed by the presence of reactive gases in the air, there have been tremendous reports on the applications of ZnO as gas sensors[11–18]. Extensive studies have been put on improving the sensing performances based on the ZnO gas sensors, aiming at improving the sensitivity, response/recovery, selectivity, stability and feasibility for practical use[19,20].

In this paper, we present a simple and effective route for the synthesis of ZnO microcrystals

with excellent ethanol sensing properties. The micro-structure sensor fabricated from these ZnO microcrystals shows high sensitivity, quick response and recovery to ethanol. The results demonstrate that ZnO microcrystals are very promising materials in fabricating ethanol sensors. Additionally, a contact-controlled model is established based on the nanocrystals, which provides another approach to realize high-performance gas sensors.

## 2. Experimental

### 2.1 Preparation and characterization of materials

ZnO microcrystals were synthesized through a facile solution method under mild conditions. All the chemicals (analytical grade reagents) were purchased from Beijing Chemicals Co. Ltd. and used as received without further purification. The deionized water with a resistivity of 18.0 M $\Omega$ /cm was used in all experiments. In a typical synthesis process, 100 mL of an aqueous solution of zinc acetate dihydrate ( $\text{Zn}(\text{CH}_3\text{COO})_2 \cdot 2\text{H}_2\text{O}$ ) and 100 mL

of a hexamethylenetetramine ( $(\text{CH}_2)_6\text{N}_4$ , HMT) aqueous solution of equal concentration (0.1 mol·L<sup>-1</sup>) were mixed together and kept under mild magnetic stirring for 5 min. Then the solution was transferred into a 500 mL flask and heated at 90°C for 2 h with refluxing. Subsequently, the resulting white products were centrifuged, washed with deionized water and ethanol, and dried at 60°C in air for further characterization. Field emission scanning electron microscopy (FESEM) images were performed on a JEOL JEM-6700F microscope operating at 5 kV. Transmission electron microscope (TEM) images and selected area electron diffraction (SAED) patterns were obtained on a JEOL JEM-2000EX microscope with an accelerating voltage of 200 kV. X-ray diffraction (XRD) analysis was conducted on a Rigaku D/max-2500 X-ray diffractometer with Cu K $\alpha$  radiation ( $\lambda=1.5418 \text{ \AA}$ ).

### 2.2 Sensor fabrication

Micro-structure sensor was fabricated on a silicon-based substrate with Pt electrodes and a Pt heater. The fabrication of the sensor was achieved according to the following steps: (i) growth SiO<sub>2</sub> (thickness of 3000 Å) on the Si-substrate as insulating layer, (ii) sputtering titanium (thickness of 450 Å) as an adhesive layer, (iii) sputtering platinum (thickness of 1800 Å) as metal electrodes, (iv) mask patterns transfer to the Si wafer by photolithography, (v) etching the two-layer metals (Ti and Pt), (vi) removing the photoresist, (vii) finally spin-coating ZnO microcrystals (thickness of 100 nm) on the substrates. The dimension of the sensor area was about 2.0 mm × 0.5 mm, and the sensing film area was about 0.6 mm × 0.5 mm. The width of the signal electrodes and heater was 50 nm, and the distance between the adjacent Pt strips was 25 nm. The cross-section, top-view and optical micrograph of the micro-structure gas sensor are shown in Figure 1(a), (b) and (c), respectively.

### 2.3 Gas sensing measurement

The as-fabricated sensor was put into several chambers with certain concentration of detecting gas to study the sensing properties.

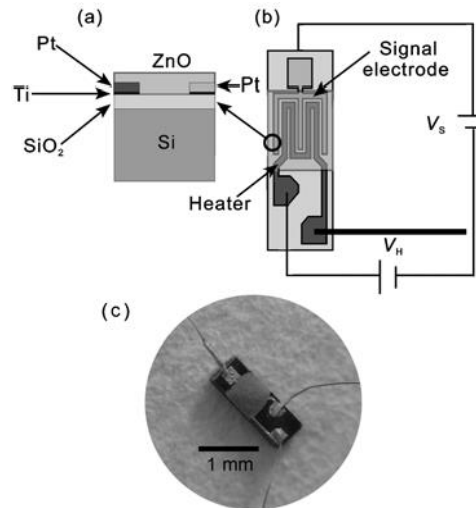


**Figure 1** Cross-section (a), top-view (b) and optical micrograph (c) of the micro-structure gas sensor.

The heater, controlled by a heating voltage ( $V_H$ , DC), ensured the operating temperature of the sensor. To measure the electrical signal of the sensing film, a voltage of 6 V was applied to the signal electrode ( $V_S$ , DC). The electrical properties of the sensors were measured by a CGS-1 intelligent test system (Beijing Elite Tech. Co., Ltd., China).

The sensitivity of the gas sensors in this paper is defined as  $R = R_a/R_g$ , where  $R_a$  is the baseline resistance of the sensing film in pure air (without access to a target gas) and  $R_g$  represents the resistance in a target gas environment. The time taken by the sensor to achieve 90% of the total resistance change was defined as the response time in the case of adsorption or the recovery time in the case of desorption.

### 3. Results and discussion

The morphology of the ZnO microcrystals is characterized by FESEM and TEM as shown in Figure 2. Figure 2(a) shows a typical image of the products, indicating the structured ZnO composed of two hexagonal prisms with the length and diameter of 3.5–5.4  $\mu\text{m}$  and 1.3–1.8  $\mu\text{m}$ , respectively. It can be obviously seen that smaller columns, with lengths of 200–400 nm and diameters of 200–800 nm, grow on the center and edge of end faces of the dumbbells. Further morphology characterization of the ZnO sample is performed on a transmission electron microscope as shown in Figure 2(b), which agrees with the FESEM results. The inset SAED pattern indicates that the dumbbells possess a single-crystal hexagonal structure and grow along the [0001] direction.

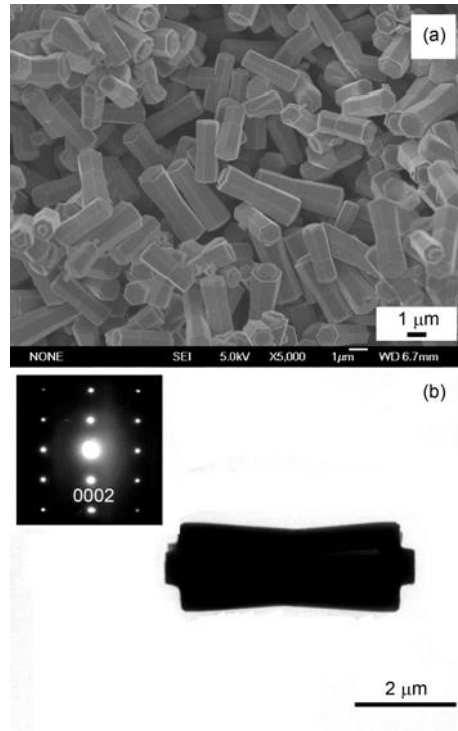


**Figure 2** FESEM image (a), TEM image (b) and SAED pattern (inset) of the ZnO microcrystals.

The structure of the as-prepared ZnO was characterized by XRD as shown in Figure 3. All the diffraction peaks can be indexed as hexagonal ZnO with lattice constants of  $a = 3.249 \text{ \AA}$  and  $c = 5.206 \text{ \AA}$ , which are consistent with the values in the standard card (JCPDS 36-1451). No diffraction peaks from any other impurities are detected.

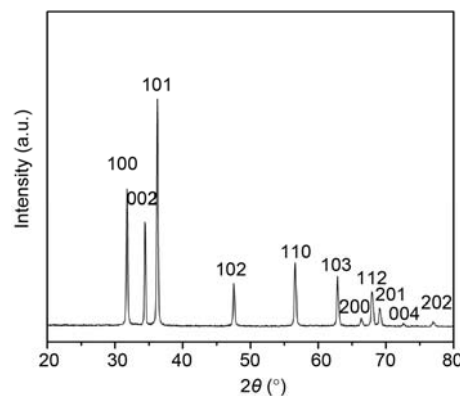


**Figure 3** XRD pattern of the ZnO microcrystals.

Gas sensing experiments are performed at different operating temperatures to find the optimum operating condition. Figure 4 shows the relationship between the operating temperature and the sensitivity to 50 ppm ethanol. The sensitivity increases and reaches its maximum at  $260^\circ\text{C}$ , and then decreased rapidly with the increasing temperature. This behavior is mainly because of the influence of operating temperature on the activation of absorbed oxygen species on the surface of ZnO film[6]. At a relatively low temperature the activation of absorbed oxygen species is low and the sensor response is consequently very small. If the temperature increases

too much, the progressive desorption of the previously adsorbed oxygen species occurs and the sensor signal decreases. Accordingly, 260°C is believed to be the optimum operating temperature for the detection of ethanol, which is applied in all the investigations hereinafter.

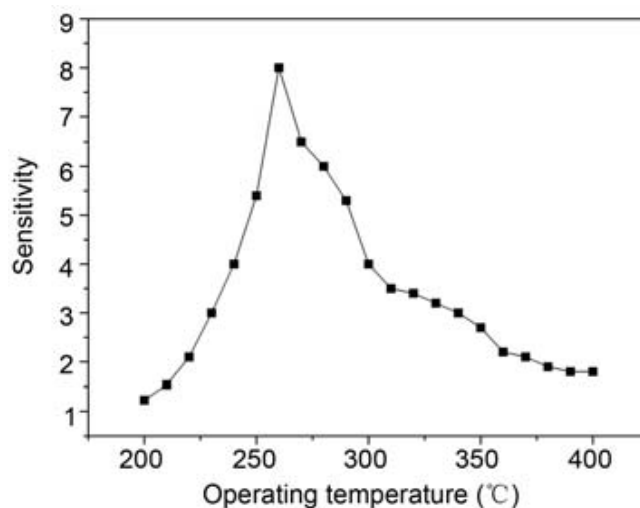


**Figure 4** The sensor sensitivity to 50 ppm ethanol at different operating temperatures.

The response and recovery characteristics of the sensor to 50 ppm ethanol at 260°C are shown in Figure 5. The sensor exhibits quick response and recovery to ethanol, and the electrical signal increases abruptly in 10 s when the sensor is exposed to ethanol. About 10 s later, the sensor is placed in air ambient again, and the electrical signal decreases to the original value in 20 s. Thus the response and recovery time are 10 s and 20 s, respectively. Figure 6 shows the sensitivity of the sensor versus ethanol concentration at 260°C, and the insert is the calibration curve in the range of 1–300 ppm. The sensitivity rapidly increases by increasing the ethanol concentration below 300 ppm. Above 300 ppm, the sensitivity slowly increases by increasing the ethanol concentration, which indicates that the sensor becomes more or less saturated. Finally, the sensor reaches saturation at about 3000 ppm. In fact, the sensitivity of the semiconducting oxide gas sensor can usually be empirically represented as  $S_g = AP_g^\beta$ , where  $P_g$  is the target gas partial pressure, which is in direct proportion to its concentration, and the sensitivity is characterized by the prefactor  $A$  and exponent  $\beta$ .  $\beta$  may have some rational fraction value (usually 1 or 1/2), depending on the charge of the surface species and the stoichiometry of the elementary reactions on the surface[21–25]. As shown in Figure 6, when the ethanol concentration is in the range of 1–300 ppm,  $\beta$  is found to be 1, which confirms that the ZnO microcrystals can be used as a promising material for gas sensors.

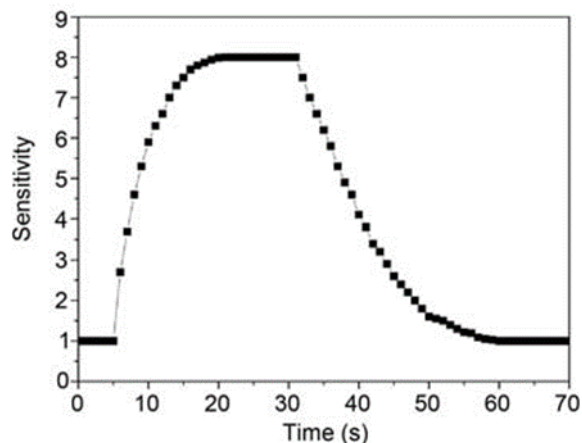


**Figure 5** Response and recovery characteristics of the ZnO microcrystal sensor to 50 ppm ethanol at 260°C.

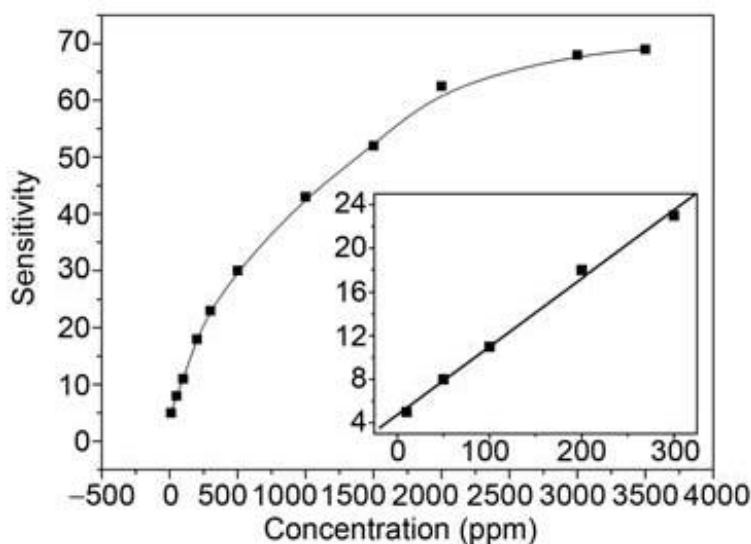


**Figure 6** The sensitivity of the ZnO microcrystal sensor vs. ethanol concentration. The insert is the calibration curve in the range of 1 – 300 ppm.

When the sensor is exposed to a reducing gas such as ethanol, the reducing gas may react with the adsorbed oxygen molecule and increase the conductance of the sensing film, thereby the sensor response can be easily found by comparing the resistance of the sensing layer in air and the target gas. The present sensor has the advantages of high sensitivity, quick response and recovery. In order to illustrate its high-performance sensing characteristics, a contact-controlled sensing is proposed based on the morphology of ZnO microcrystals. We think that many contacts are formed among the ZnO microcrystals, leading to the formation of many junctions in the sensing film. The surface depletion width is about several nanometers for ZnO in air[24]. Because the diameter of ZnO microcrystals is much larger than the depletion width, surface depletion does not greatly affect the density and mobility of the electrons in the microcrystals but does significantly modify the potential barrier of the contacts between the

microcrystals. Comparing with many semiconductor metal oxide sensors, more effective contacts will form and most of them in the sensing film contribute to the sensing, thus the modulation in carrier concentration of the contacts between ZnO microcrystals becomes larger and a higher sensitivity can be realized.

#### 4. Conclusions

ZnO microcrystals have been synthesized through a facile solution method and characterized by FESEM, TEM and XRD. The micro-structure sensor fabricated from these ZnO microcrystals exhibits high sensitivity and quick response-recovery to ethanol at 260°C. A contact- controlled model is established to explain the sensing properties of our microcrystals. Our results demonstrate the potential application of ZnO microcrystals for fabricating high-performance gas sensors.

#### References

- [1]Badis Bendjemil, Mohamed Mouyane, Jacques G. Noudem, Jérôme Bernard, Jean Michel Reboul, Yannick Guel, David Houivet, Exp. Theo. NANOTECHNOLOGY 3 (2019) 243
- [2]Guo B, Bermak A, Chan P C H, et al. A monolithic integrated 4×4 tin oxide gas sensor array with on-chip multiplexing and differential readout circuits. Solid-State Electron, 2007, 51: 69—76
- [3]Leman O, Chaehoi A, Mailly F, et al. Modeling and system-level simulation of a CMOS convective accelerometer. Solid-State Electron, 2007, 51: 1609—1617
- [4]Olbrechts B, Rue B, Suski J, et al. Characterization of FD SOI devices and VCO's on thin dielectric membranes under pressure. Solid-State Electron, 2007, 51: 1229—1237
- [5]Su P G, Wu R J, Nieh F P. Detection of nitrogen dioxide using mixed tungsten oxide-based thick film semiconductor sensor. Talanta, 2003, 59: 667—672
- [6]R. Ahmed Ammar, M. Lemerin, Exp. Theo. NANOTECHNOLOGY 3 (2019) 275
- [7]Navamathavan R, Choi C K, Yang E J, et al. Fabrication and characterizations of ZnO thin film transistors prepared by using radio frequency magnetron sputtering. Solid-State Electron, 2008, 52: 813—816
- [8]Iñiguez B, Picos R, Veksler D, et al. Universal compact model for long- and short-channel thin-film transistors. Solid-State Electron, 2008, 52: 400—405
- [9]Mandalapu L J, Xiu F X, Yang Z, et al. Ultraviolet photoconductive detectors based on Ga-doped ZnO films grown by molecular-beam epitaxy. Solid-State Electron, 2007, 51: 1014—1017
- [10] Wang D, Chu X, Gong M. Hydrothermal growth of ZnO nanoscrew-drivers and their gas sensing properties. Nanotechnology, 2007, 18: 185601
- [11] Chen Z J, Han T, Ji X J, et al. Lamb wave sensors array for nonviscous liquid sensing. Sci China Ser G-Phys Mech Astron, 2006, 49: 461—472
- [12] Xu D, Gu J H, Wu S. Development and application of flexible substrate sensors in instantaneous heat flux measurement. Chinese Sci Bull, 2009, 54: 1311—1316
- [13] A. H. Laatar, S. Kennich, J. Balti, N. Badi, Exp. Theo. NANOTECHNOLOGY 3 (2019) 285

- [14] Ling Z Y, Chen S S, Wang J C, et al. Fabrication and properties of anodic alumina humidity sensor with through-hole structure. *Chinese Sci Bull*, 2008, 53: 183—187
- [15] Wu C S, Wang L J, Zhou J, et al. The progress of olfactory transduction and biomimetic olfactory-based biosensors. *Chinese Sci Bull*, 2007, 52: 1886—1896
- [16] Luo J, Huang Y Y, Xiong S X, et al. Study on peptide-peptide interaction using high-performance affinity chromatography and quartz crystal microbalance biosensor. *Chinese Sci Bull*, 2007, 52: 1311—1319
- [17] Wu S, Chen H, Gu J H, et al. A thermal insulation method for a piezoelectric transducer. *Chinese Sci Bull*, 2007, 52: 2305—2309
- [18] Yu J H, Choi G M. Electrical and CO gas-sensing properties of ZnO/SnO<sub>2</sub> heterocontact. *Sens Actuat B Chem*, 1999, 61: 59—67
- [19] Li C C, Du Z F, Li L M, et al. Surface-depletion controlled gas sensing of ZnO nanorods grown at room temperature. *Appl Phys Lett*, 2007, 91: 032101
- [20] Feng P, Xue X Y, Liu Y G, et al. Highly sensitive ethanol sensors based on {100}-bounded In<sub>2</sub>O<sub>3</sub> nanocrystals due to face contact. *Appl Phys Lett*, 2006, 89: 243514
- [21] Wan Q, Li Q H, Chen Y J, et al. Fabrication and ethanol sensing characteristics of ZnO nanowire gas sensors. *Appl Phys Lett*, 2004, 84: 3654—3656
- [22] Chen Y J, Xue X Y, Wang Y G, et al. Synthesis and ethanol sensing characteristics of single crystalline SnO<sub>2</sub> nanorods. *Appl Phys Lett*, 2005, 87: 233503
- [23] Adawiya J. Haider, Mahammed K. Dhaer, Khalil I. Hajem, *Exp. Theo. NANOTECHNOLOGY 3* (2019) 305
- [24] Chen Y, Zhu C L, Xiao G. Reduced-temperature ethanol sensing characteristics of flower-like ZnO nanorods synthesized by a sonochemical method. *Nanotechnology*, 2006, 17: 4537—4541
- [25] Barsan N, Koziej D, Weimar U. Metal oxide-based gas sensor research: How to? *Sens Actuat B Chem*, 2007, 121: 18—35

## Structural and optical properties of lead iodide nanostructure synthesized by vacuum evaporation method

C. V. Rajon, H. A. Serajecko, J. Cohen\*

Department of Chemistry & Biochemistry, University of Texas at Arlington, Arlington, Texas, 76019, USA.

Email: [james.cohen@uta.edu](mailto:james.cohen@uta.edu)

*Received: 1/11/2019 / Accepted: 17/2/2020 / Published: 1/4/2020*

Structural and optical properties were studied as a function of films thickness for thermally evaporation PbI<sub>2</sub> films. X-ray diffraction analysis confirmed that PbI<sub>2</sub> films are polycrystalline having hexagonal structure. The optical absorption data indicate an allowed direct transmission with optical energy gap varies continuously from (2.15eV - 2.33 eV). The energy gap shows thickness dependence, which can be explained qualitatively by a thickness dependence of grain size through the decrease of the grain boundary barrier height with grain size. The low fluctuation in energy gap indicates that the grain size is quite small, which is finding in agreement with AFM results.

**Keywords:** PbI<sub>2</sub>; Optical; Structural.

### 1-Introduction

Lead iodide PbI<sub>2</sub> is a wide band gap semiconductors  $E_g \sim 2.3$  eV. Due to the high atomic number of its elements ( $Z_{Pb}=82$ ,  $Z_I=53$ ), it is a material with potential use as an ionizing radiation detector (X and  $\gamma$  rays) [1,2,3]. Lead iodide is an important and promising P-type semiconductor and crystallizes in a hexagonal structure and can be grown from solution, vapor and gels [4]. The polytypism of PbI<sub>2</sub> seems to be a significant property of this material with no structure modification. Lead iodide is isostructural to CdI<sub>2</sub> and 20 polytypes have been reported. The poly types of PbI<sub>2</sub> are 2H, 4H, 6H, 8H, 12H, 12R, 14H, 18H, 18R, 20H, 20R, 36H, 42R, 48R. The most common type is 2H, which represents 95% polytypes described for PbI<sub>2</sub> structure [5]. Recently many researches were published on the development of the method of prepared thin films of PbI<sub>2</sub> from solutions, vapor, melts and gels. Similarly to the recently published results reporting on the influence of rare earth (RE) elements on the quality of materials for radiation detectors [6].

Electronic transport and optical measurements in polycrystalline PbI<sub>2</sub> by vacuum evaporation with different thickness and grain size up to 100 nm was studied [7,8]. Conventional vacuum coating unit (INFICON V90) under vacuum of order of  $6 \times 10^{-6}$  torr with deposition rate of  $\sim 4-7 \text{ nm sec}^{-1}$ . A summary of the deposition conditions is shown in table (1). Film thickness was measured after evaporation by optical interferometer method, using He-Ne Laser  $\lambda = 632.8 \text{ nm}$  and the thickness were determined. The aim of this work is to prepare a thin polycrystalline lead iodide by vacuum evaporation method, and studying the optical and structural properties of this material to present preliminary results which in this approach could be a way to develop PbI<sub>2</sub> nuclear imaging devices beside the electrical properties.

**Table 1** Summary of deposition conditions. [5].

Coating Unit	INFICON V90
Materials	Lead iodide (PbI <sub>2</sub> ) powder
Substrates	glass slides
Vacuum	$\sim 6 \times 10^{-6}$ torr
Substrate to film gap	15 cm
Deposition rate	$\sim 4-7 \text{ nm sec}^{-1}$

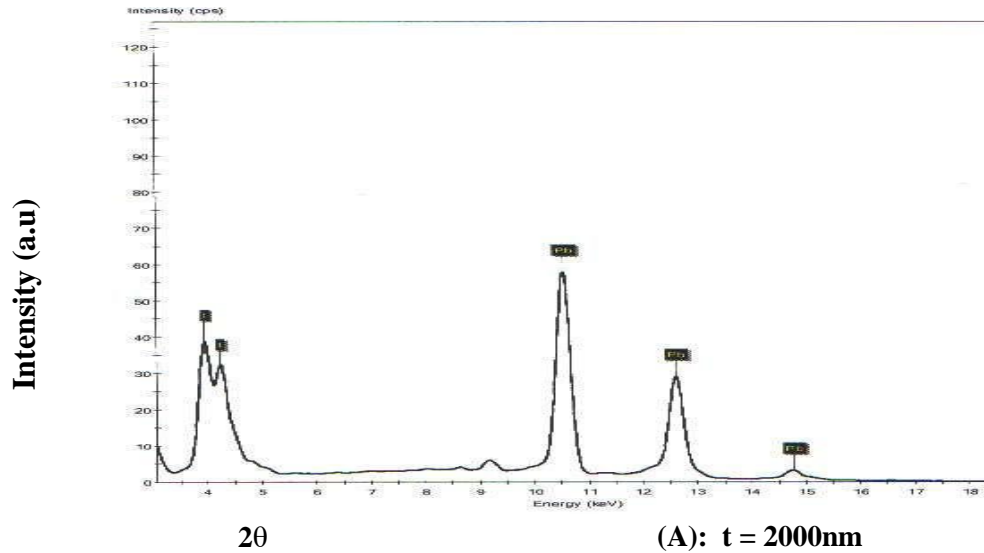
## 2- Experimental details

Polycrystalline PbI<sub>2</sub> samples were prepared on glass substrates using vacuum evaporation method. PbI<sub>2</sub> powder prepared in the laboratories without further purification as in [9] as checked by X-ray fluorescence the main residual impurity in the base material is Ag as is shown in figure (1). The PbI<sub>2</sub> powder was preheated at temperature  $\sim 250 \text{ }^\circ\text{C}$  for several hours to remove occluded materials from it. The prepared material was housed in a vacuum deposition chamber for the preparation of thin film. The E-glass substrate was kept in ambient at  $200^\circ\text{C}$  to maintain stoichiometry. At first, a film has been prepared then by decreasing the substrate temperature at a rate  $\sim 1\text{K}$  per minute until we brought to room temperature. This process will reduce the defect and grain boundaries if any considerably. The color of the film appears to be pale yellow in nature. The evaporation was carried out.

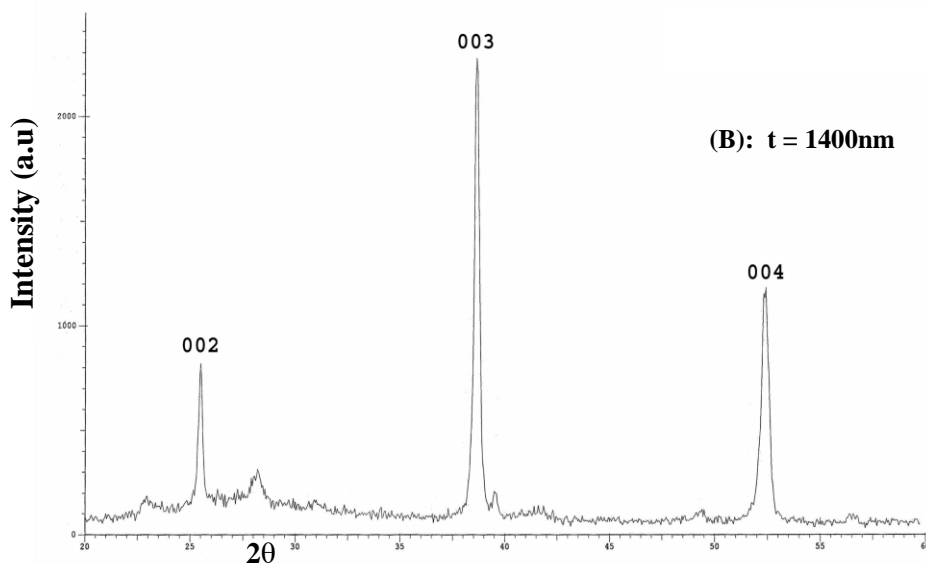
## 3- Results and discussion

X-ray diffraction analyses of all the films with different thickness show a high degree of crystallite orientation with the basal plane parallel to substrate and c-axis normal to the substrate plane indicated by the negligible relative intensity of (002), (003) and (004) reflection. X-ray diffraction (XRD) pattern of the films deposited on glass substrate in a "Shimadzu XRD 6000". Advance using Cu-K $\alpha$  radiation of monochromatic wavelength. For pure PbI<sub>2</sub> films recorded for a range of  $2^\circ$  from  $10^\circ$  to  $60^\circ$  at  $2^\circ$  glancing angle. Figure (2:A,B,C,D) shows a typical XRD of a thin film of lead iodide samples.

The inter-planer distance  $d$  and  $(hkl)$  planes are shown in table (2), which corresponds to XRD and standard ASTM data [10], the main facts of all XRD patterns are the existence of the same peaks through different deposition conditions.



**Figure 1** X-ray fluorescence pattern of  $\text{PbI}_2$



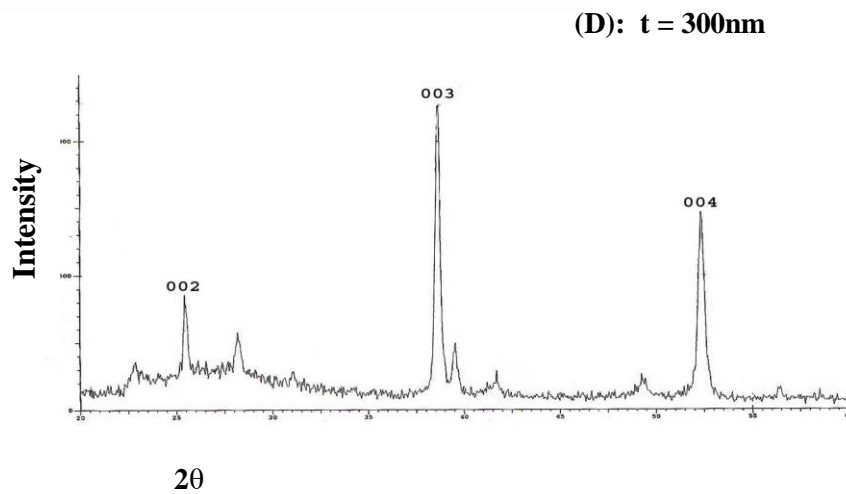
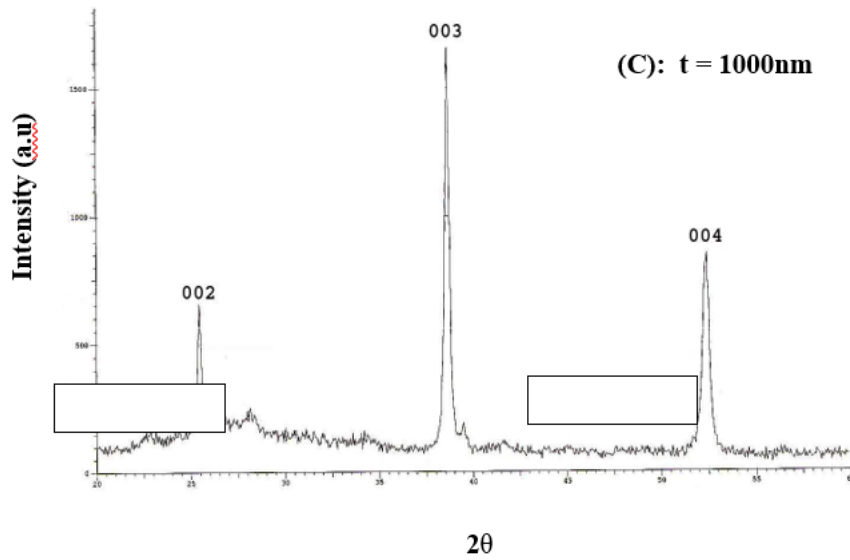


**Figure 2** X-Ray diffraction pattern and miller indices of PbI<sub>2</sub> films prepared with different thickness

**Table 2** Structural values of PbI<sub>2</sub> thin films at different thickness with ASTM.

Thickness nm	2	d (Å <sup>o</sup> )		hkl	δ	FWHM (deg.)	Average G.S(nm)
		Observed	d (Å <sub>o</sub> ) ASTM				
300	25.5126	3.4886	3.4890	002	0.011	0.2455	36.7303
	38.6567	2.3260	2.3270	003	0.043	0.2777	

	52.362	1.7458	1.74490	004	0.114	0.3401	
1000	25.5221	3.48733	3.4890	002	0.057	0.24110	39.4976
	38.6581	2.32520	2.3270	003	0.077	0.25760	
	52.3631	52.3631	1.74490	004	0.16	0.34820	
1400	25.5476	3.48390	3.4890	002	0.171	0.21590	43.6354
	38.7002	2.3250	2.3270	003	0.086	0.2323	
	52.4105	1.74439	1.74490	004	0.057	0.2538	
2000	25.4951	3.4909	3.4890	002	0.054	0.2527	46.4670
	38.6434	2.32469	2.3270	003	0.103	0.21797	
	52.348	1.74632	1.74490	004	0.172	0.3795	

A comparison between our results and those of the ASTM standard data is shown in table (2). It is clear that a strong peak is observed at ( $d= 3.486, 2.332$  and  $1.744 \text{ \AA}^0$ ) which corresponds to the reflection planes (002), (003) and (004) respectively. These results are agreed well with data achieved by others [1,3]. An accurate observation of each reflection peak for most samples reveals the presence of two less intense peaks very close to the main one ( $30\text{-}40^\circ$ ). This is probably due to the presence of polytypes [10,11]. As shown in figure (3A,B) an AFM (Atomic force micrograph) model (AA3000) scanning prop microscope was used in this search, the AFM Where G.S is the average grain size is the X-ray wavelength,  $\Delta(2\theta)$  is (FWHM),  $\theta$  Bragg diffraction angle of XRD peak (degree). Figure (4) shows the variation in the average grain size with different thickness. Average grain size increases linearly with increasing thickness. The increasing tensile stress as it seen in figure (3) may be responsible for the flattening of grains.

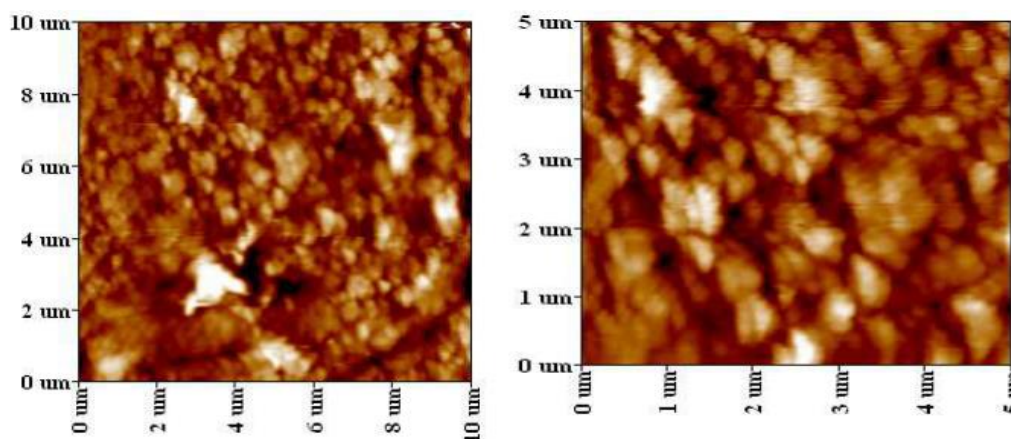


**Figure 3** AFM photograph of  $\text{PbI}_2$  films at thickness (A) 1000nm and (B) 2000 nm

In the X-ray diffraction data, we have directly measured  $\Delta(2\theta)$  for major peaks of appreciable relative intensities we can calculate [14], results show very smooth surfaces for both 1000 nm and 2000 nm thickness,  $[d_{ASTM} / d_{XRD} / d_{ASTM}] 100\%$  (1)

with an average surface roughness of 23nm for 1000nm thickness and 19.1nm for 2000nm thickness. Also different in grains area with different thickness, in thickness 1000nm the grains area seems smaller than in the case of 2000nm thickness.

The X-ray diffraction data can also be used to determined residual stress or non-uniform strain in the film due to structural defects like dislocation, stacking faults, which are quite common in the films grown by thermal evaporation. The in homogeneous stress in the film can be determined from the line broadening  $\Delta(2\theta)$ , full width at half maximum (FWHM) (Where  $2\theta$  is the diffraction angel), which is also related to the variation in d spacing (where d is the distance between any two parallel crystal planes having the same Miller index (hkl) through a relation [12].

Where  $\delta$  is the residual stress. From the observed  $d_{hkl}$  with reference to  $d_{hkl}$  (ASTM) from corresponding powder data ASTM. All the analysis carried, the residual stress  $\Delta d/d$  was found to be tensile and increase linearly with film thickness as it shown in figure (5). The residual stress may increase with film thickness depending mainly on the depositing material and growth conditions [13]. Different materials show different behaviors. However, the linear dependence of  $d/d$  on film thickness observed for PbI<sub>2</sub> films could be due to the orientation crystallite growth.[15].

The optical transmission spectra of PbI<sub>2</sub> films deposited on the glass substrate at different thickness was recorded as a function of wavelength in the range of (380-900) nm at room temperature it shown in the figure (6). The average transmission over the rang

$$\Delta(2\theta) = 2 \tan \theta \quad (2)$$

(380-900) nm exceeds 85% with a sharp fall near the fundamental absorption; The average grain size is determined from the full width at half maximum (FWHM) for the most intense peak using the Scherrers formula [13], whereas fall in transmission is gradual for other samples, these results are good agreement with the measurements results obtained by T.Ghosh et al [16]

The absorption coefficient ( $\alpha$ ) was calculated using Lambert law as follows [14 ]:

$$\ln(I_0/I) = 2.303A = \alpha d \quad (3) \text{ where}$$

$I_0$  and  $I$  are the intensity of incident light and transmission light respectively,  $A$  is the optical absorbance and  $d$  the sample thickness. The absorption coefficient ( $\alpha$ ) was found to follow the relation:

$$\alpha = [G(h\nu - E_g)^{1/2}] / h\nu \quad (4)$$

where  $G$  is a constant and  $E_g$  the optical energy gap, figure (7) shows the relation between absorption coefficient and photon energy. Plots of  $(\alpha h\nu)^2$  versus the photon energy ( $h\nu$ ) in the absorption region near the fundamental absorption edge indicate direct allowed transmission in the film material, as shown in figure (8). The optical energy gap was estimated from the extrapolation of the linear portion of the graph to the photon energy axis [17]. It is observed that  $E_g$  degrades with increasing thickness as it shown in figure (9). The interface between the substrate and films is an important junction where free energy supplied and minimizing it by a slow process shall reduce the chance of formation of decades, and the grain size[5]. In general, thickness dependence of optical band gap can arise due to one or combined effect of the change in barrier height due to change in grain size in polycrystalline films as given in Table 3 [18].

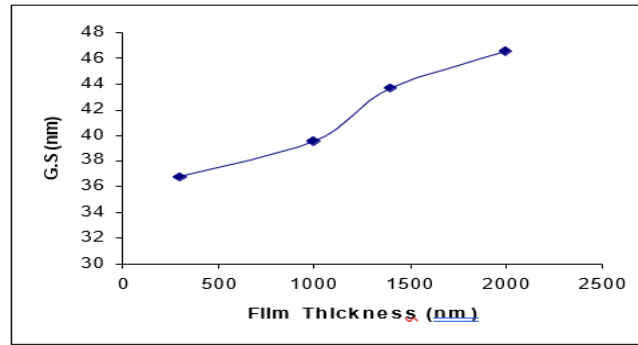


Figure 4 Grain size with film thickness of PbI<sub>2</sub>

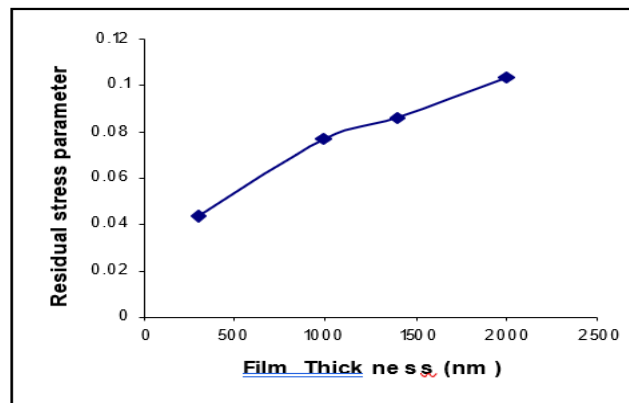


Figure 5 Residual stress with film thickness of PbI<sub>2</sub>

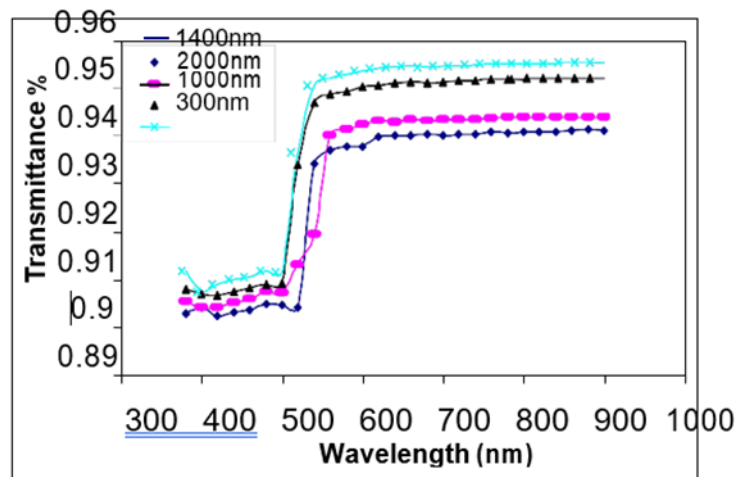
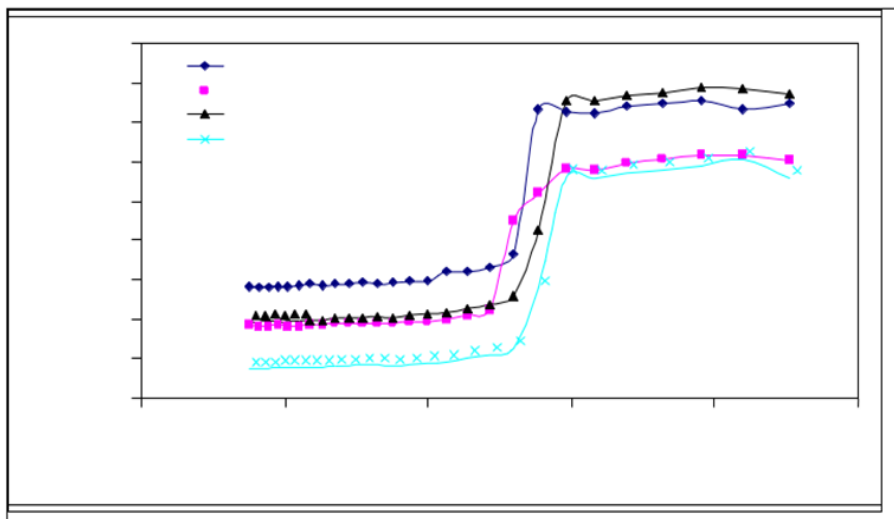
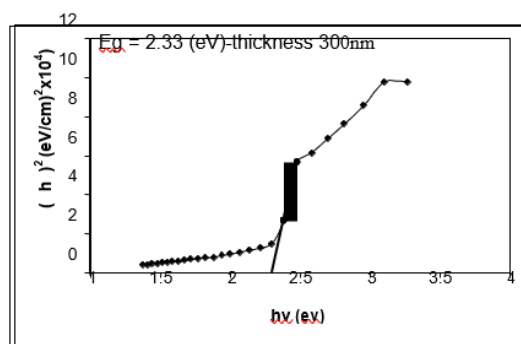
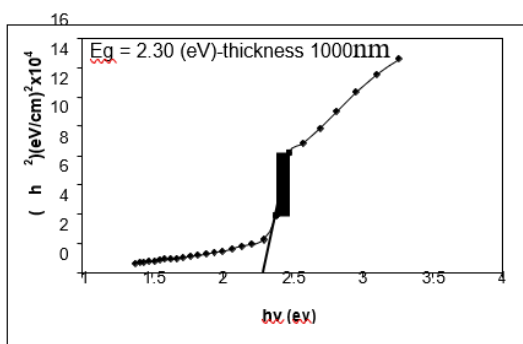


Figure 6 Optical transmittance spectra for different thickness of PbI<sub>2</sub>



**Figure 7** Absorption coefficient as a function of  $h$  for  $PbI_2$  films with different thickness

**Table 3** Values of band gap for different thickness of  $PbI_2$



Thickness (nm)	Band gap (eV)
300	2.33
1000	2.3
1400	2.24
2000	2.15

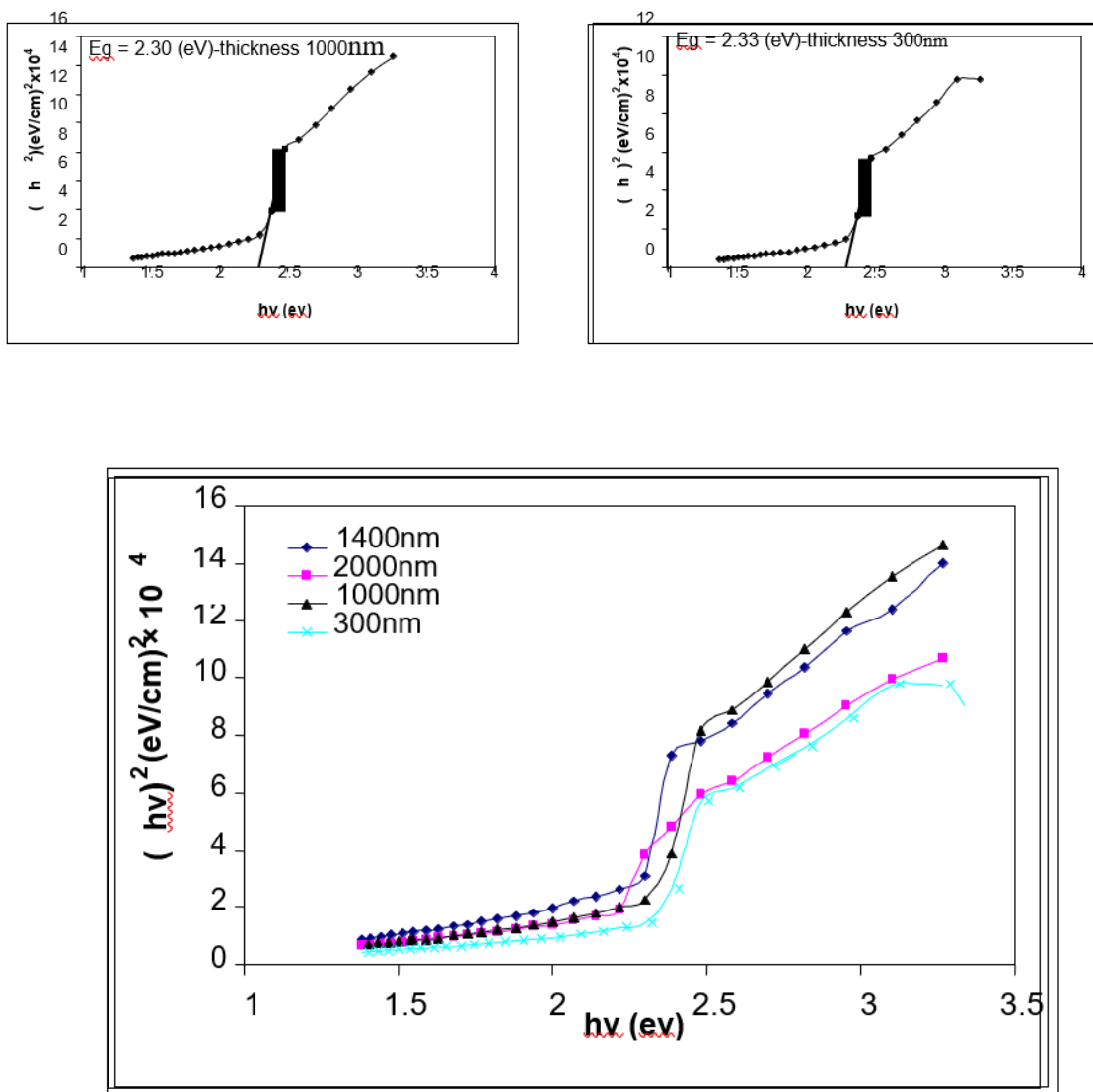


**Figure 8** Photon energy dependences of the absorption coefficient squared for PbI<sub>2</sub> films with different thickness to determine of  $E_g$

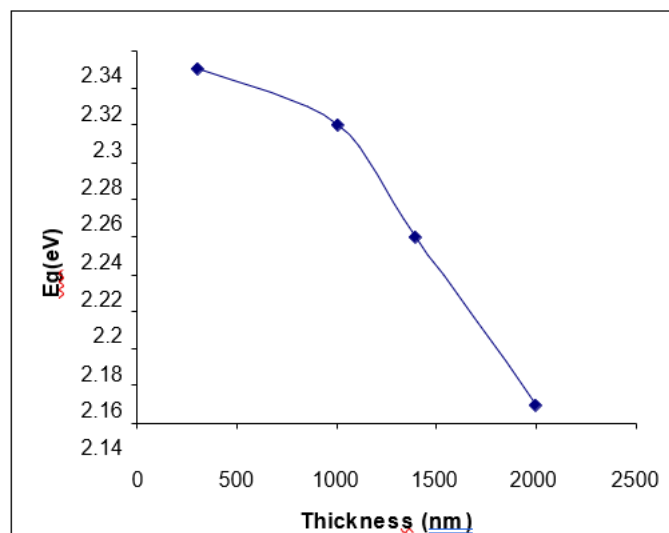


**Figure 9** Film thickness dependence on direct optical energy gap for  $\text{PbI}_2$  films

### Conclusions

The X-ray diffraction analysis confirms that  $\text{PbI}_2$  films are polycrystalline, having a hexagonal structure. The inception of the data for pure thin film of lead iodide indicates that the observed ( $d$ ) values closely match with the existing standard values for hexagonal structure. The low fluctuation in the value of structure parameters is due to the fluctuation in lattice parameters, which is attributed to the stress (positive) that accompanies the increase in grain size. The values of the band gap vary from (2.15 eV– 2.33 eV). The low fluctuation in energy gap with sample thickness indicates that the grain size is quite small. The results are in agreement with existing works adopting different techniques for film preparation. The reproducibility in making thin films of  $\text{PbI}_2$  is very good by the present method.

### References

- [1] Arafa H Aly, Walaa M. Nouman, S.E.-S. Abd El-Ghany, Samira M.Sallam, AbdelFattah B. Dawood, *Exp. Theo. NANOTECHNOLOGY* 3 (2019) 315
- [2] D.S.Bhavsar, K.B.Saraf, *Mat, Chem. Phys.* 78 (2003) 630-639
- [3] M.Svatusk, J.Zavadil, M.Matuchova, *J.Phys Chem* 97 (1993) 9288-9295
- [4] A.Nayak, G.L.Bhalla, B.Kumar, G.C.Tricunat, *Phys State Sol (b)* 213 (1999) 487-488
- [5] T.Ghosh, S.Bandyopadhyay, K.K.Roy, S.Kar, A.K.Lahiri, A.K.Maiti, K.Goswami, *Cryst.Res. Technol.* 43 (2008) 959-963
- [6] R.A.street, S.E.Ready and F.Lemmi, *Journal of Applied Physics* 86 (1999) 2660-2666
- [7] O.V.Rybak, Yu.O.Lun, I.M.Bordun, M.F.Omelyan, *Inorganic Materials* 41 (2005) 1124-1127
- [8] Ali H. AL-Hamdani, Mohammed A.R. Hussein, Aya H. Makki, *Exp. Theo.*

NANOTECHNOLOGY 3 (2019) 1.

[9] M. Namdar, Sh. Kh. Asl, ExExp. Theo. NANOTECHNOLOGY 3 (2019) 9

[10]Gopik.Kasi, Norman.R.Dollahon, Temer S.Ahmadi, Journal of Physics D: Applied Phys. 40 (2007) 1778-1783

[11] M.Matuchva, O.Prochazkova, J.Maixner, K.Zdansky, J.Zavadil, Phys Stat. Sol (C) 2 (2005) 1275-1279

[12]Arafa H. Aly, Ahmed Mehaney, Shrouk Eid, Exp. Theo. NANOTECHNOLOGY 3 (2019)19

[13] B.D.Cullity, Elements of x-ray Diffraction, 2<sup>nd</sup> edition, Addison Wesley published Company,INC,1978.

[14]P.Tyagi and A.G.Vedeshwar, Eur.Phys.J.AP 19,3-13.pp7, (2002).

[15] P.Tyagi, A.G.Vedeshwar, Phys.Rev. B 64 (2001) 245406-245414

[16]T.Ghosh, S.Bandyopadhyay K. K .Roy ,S.Kar ,A.K.Lahiri, A.K.Maiti, K.Goswami, Crst. Res. Tehnol. 43 (2008) 959-963 \

[17] N.F.Mott, E.A.Davis, "Electronic processes in Noncrystalline materials"(Clarendon Press-Oxford. pp.273-274, ,(1979).

[18] P.Tyagi and A.G.Vedeshwar, Bull. Mater. Sci. 24 (2001) 297-300



## Synthesis of CdS nanotubes and nanospheres by living bio-membrane bi-template

T. Sunagai, I. Hiro\*

Hayashibara Co., Ltd., Shimoishii, Kita-ku Okayama 700-0907, Japan

Faculty of Natural Science, Otani University, Kyoto, Japan

\*) Email: [ihiro@chem.eng.osaka-u.ac.jp](mailto:ihiro@chem.eng.osaka-u.ac.jp)

Received: 15/1/2020 / Accepted: 24/3/2020 / Published: 1/4/2020

Semiconductor CdS nanotubes with a small ratio of length to diameter and nanospheres were simultaneously synthesized in the light of bio-mineralization process through living bio-membrane bi-template of mungbean sprouts at room temperature. The outside diameter of the nanotube is 220–240 nm and the inner diameter is 200–220 nm, the length is up to 600–700 nm and the ratio of length to diameter is 2:1. The nanospheres are 25 nm in diameter and well distributed. The XRD pattern indicates that these nanocrystals were crystallized in the cubic structure with lattice  $a = 5.818 \text{ \AA}$ . The optical properties of the products are illustrated, and their possible forming mechanism is explored.

**Keywords:** CdS; Nanotube; Bi-template.

### 1. Introduction

Group II-VI semiconductors, because of its wider band width and nonlinear optical properties, have already shown vital applications in fluorescence probe, sensors, solar battery, photoelectrocatalysis, photoelectricity devices, laser light-emitting diodes[1-3]etc. CdS is one of the most important materials in the group II-VI semiconductors. And its synthesis, assembly and the particles morphology control have received great attention all the time. A number of methods have been developed to synthesize the CdS nanomaterials such as hydrothermal-solvothermal methods[2,4], SBA-15 templates[5], sol-gel methods[6], single-source molecular precursors methods[7],

polymethylmethacrylate matrix methods[8], porous alumina template[9], etc. However, so far there has been no report on the synthesis of CdS nanomaterials through living bio-membrane bi-template. Especially, no one has achieved the successful synthesis of different morphologies of CdS nanomaterials simultaneously. In addition, there are many reports about

synthesis of CdS nanotubes<sup>[10–12]</sup>, mainly on large L/D nanotubes and there is no report on the syn- thesis of small L/D nanotubes (L/D=2).

It is well known that there are many active groups and special transport proteins on living bio- membrane, which could transport ions, and induce biological min- eralization as well[13-15]. Many living bio-membranes have different structures on the outer and inner surfaces, and there are some active groups on the surface such as hydroxyl, amido, carboxyl and special transport pro- teins, so it is possible to assemble significant nanoma- terials with different morphologies, when the nuclea- tion and growth of molecules are induced through liv- ing bio-system.

Mungbean sprout is a simple living bio-membrane material easily available. Its surface is uniform with many shallow channels, and there are many vasculars in its stem (Figs. 1 and 2). And there are great differ- ences in structure between the outer surface of the mungbean sprout and the inner vascular tissue. The inorganic ions could be controlled to enter or exit the organism through the membrane, when the whole mungbean sprout is easily survived and kept fresh in solutions, so it is ideal as a living bio-membrane bi-temple. Because of the abundance in the living bio-membrane of plant and animal in the world, the method would be significative not only on materials science, biology and chemistry, but on the environments.

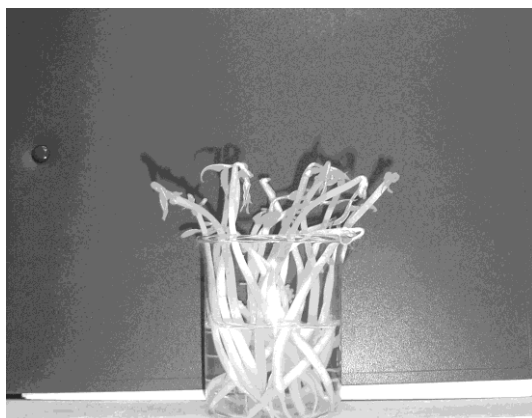


Fig. 1. The whole morphology of mungbean sprout.

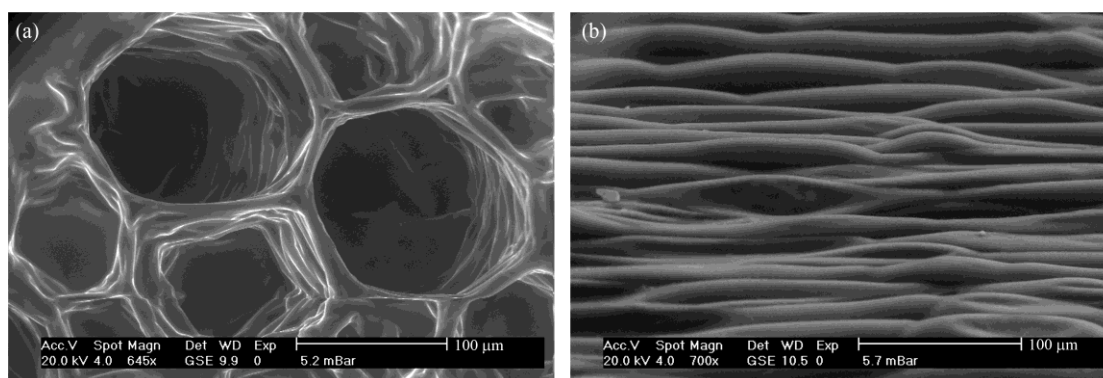


Fig. 2. ESEM pattern of mungbean sprout. (a) The interior of mungbean sprout; (b) surface of mungbean sprout.

In this paper, two kinds of semiconductor CdS nanomaterials with different morphologies were synthesized simultaneously through living bio-membrane bi-template for the first time. In them, the nanotube with small L/D is a novel structure and has potential application in the assembly of nanodevice.

## 2. Experimental

### 2.1 Reagent and instrument

Chemicals:  $\text{Na}_2\text{S}\cdot 9\text{H}_2\text{O}$ ,  $\text{CdCl}_2\cdot 2.5\text{H}_2\text{O}$ , carbon disulfide and absolute ethanol (A.R.) (purchased from the Shanghai Chemical Reagent Factory, China). Mungbean sprouts were purchased from the market.

Instruments: TEM images and electron diffraction spectrum were carried out on a Hitachi Model-800 transmission electron microscope. Powder X-ray diffraction (XRD) pattern of sample was measured on 1710 diffraction with  $\text{Cu K}\alpha$  radiation ( $\lambda=0.15406$  nm) (Philips). ESEM images were carried out on XL-30E scanning electron microscope (Philips). Absorption spectrum was recorded on Aligent 8453 UV-Visible spectrophotometer. PL spectra were obtained on a Perkin-Elmer luminescence spectrophotometer (LS-55) (PL, USA).

### 2.2 Experimental process

- (1) Immersing the mungbean sprouts (except laminae) in solution of 0.08 mol/L  $\text{Na}_2\text{S}$  for 12 h.
- (2) Taking out the mungbean sprouts and washing them with deionized water. Then immersing them in solution of 0.1 mol/L  $\text{CdCl}_2$  for 24 h.
- (3) Washing the mungbean sprouts with deionized water and ethanol, and transferring the different yellow products into two beakers containing absolute ethanol.
- (4) Purifying the products through using carbon disulfide to remove excess sulfur.
- (5) Taking a small amount of ethanol containing CdS nanomaterials, and dripping one or two drops on the meshwork after ultrasound. Then illustrating the morphology and structure of products through TEM and ED.

## 3. Results and discussion

### 3.1 TEM and ED measurements

Figure 3 shows the TEM micrograph and SAED pattern of the products synthesized through outer template of living bio-membrane bi-template. From the TEM micrograph, it could be concluded that the tubular nanomaterials would emerge through regulating experimental condition. The outside diameter of this nanotube is 200–240 nm and the inner diameter is 200–220 nm, the length is up to 600–700 nm and the length to diameter ratio is 2:1. Both ends of the nanotubes are opened. The partial magnification image (Fig. 3(c), magnification= $8\times 10^4$ ) of the products demonstrates that the wall is very smooth with thickness being 20–30 nm and minor L/D nanotubes have not been reported up to now.

Figure 3(c) is the magnification image of single nanotube. Its structure is quite different from the nanorod (Fig. 3(d)), which has solid structure. The fringe color of the nanorod is light but the nanotube is dark. The color of the nanotube middle is light and the structure is hollow. The selected area electron diffraction in Fig. 3(d) shows that these nanotubes are polycrystalline in structure. The corresponding lattice planes from inner to outer rings are

(111), (220), and (311).

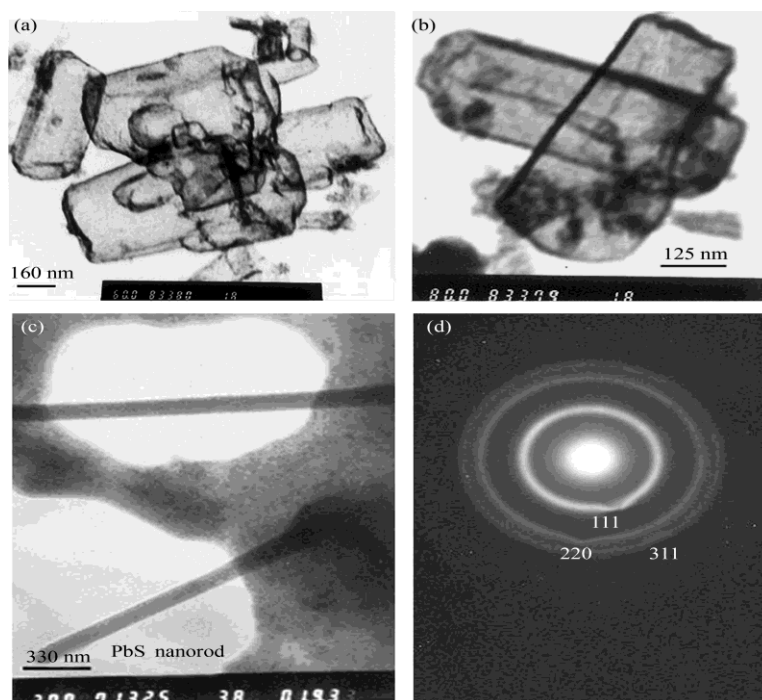


Fig. 3. (a), (b) TEM images of CdS nanotubes (external products); (c) TEM images of nanorod; (d) SAED image of prepared products.

Fig. 4 shows the TEM image and SAED pattern of inner products synthesized through living bio-membrane bi-template. The products are irregular nano-spheres and dispersed well, and the dimension of them is 25 nm. The dimensions of the products have been nanosized and this is the key factor of the optics optimization. And because of the spherical morphology of the products, they are useful for the machine lubrication. From the irregular diffraction spots of SAED pattern, it is suggested that they are single-crystalline in structure.

#### a. XRD study

The crystal structure of the semiconductor nanomaterials is very important because the different functions and applications of photochemistry are influenced by the crystal structure. The XRD pattern (Fig. 5) indicates that these nanocrystals of inner and outer products were crystallized in the cubic structure with lattice constants  $a = 5.818 \text{ \AA}$ , which is consistent with JC–PDS card No.10-454. And it also shows that there are no mixed peaks and the products are of high purity.

#### b. Choice of experiment conditions

The experiment condition and sequence have certain impact on the growth of CdS nanomaterials. During the experiment, the concentrations of 0.2, 0.1, 0.05 and 0.025 mol/L CdCl<sub>2</sub> or Na<sub>2</sub>S solution were chosen respectively. When the concentration was too high, it was not a suitable environment for mungbean sprout to live and bulk materials increased gradually. When the concentration was too low, synthetic efficiency would reduce. So, the concentrations of 0.1 and 0.08 mol/L were chosen separately for CdCl<sub>2</sub> and Na<sub>2</sub>S. In order to eliminate the “toxicity of single salt” caused by the metal ions, the order of metal ions was the S<sup>2-</sup> and then Cd<sup>2+</sup>. This is mainly because the absorption and combination of anion and cation was controlled by bio-membrane. If the mungbean sprout was immersed

in the solution of  $\text{Cd}^{2+}$  firstly, it would lose the function of organism and the following reaction would not continue. If the mungbean sprouts were immersed in the solution of  $\text{S}^{2-}$  firstly, it would not only accelerate the synthesis reaction but also offer nutrition to the living bio-membrane.

In addition, when the mungbean sprout was immersed in the solution of  $\text{S}^{2-}$  and  $\text{Cd}^{2+}$ , the leaf and the stem were kept fresh. Hence, it is reasonable that the nanomaterials were synthesized through living bio- membrane.

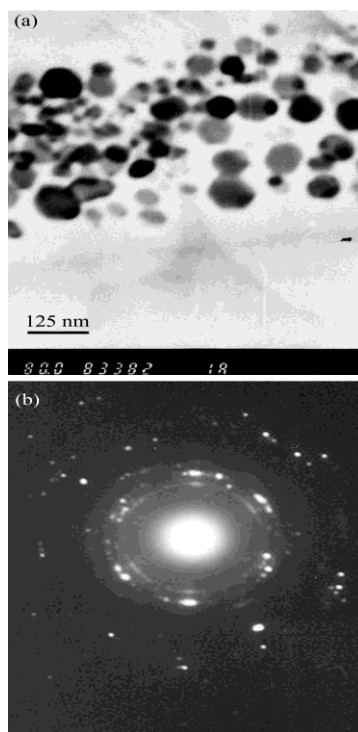


Fig. 4. (a) TEM images of CdS nanospheres; (b) SAED images of CdS nanospheres.

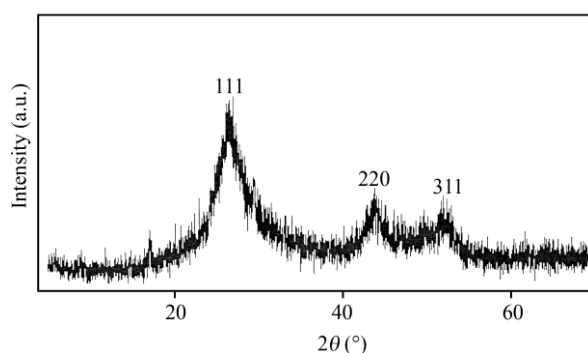


Fig. 5. XRD pattern of CdS nanomaterials.

### 3.2 Synthetic mechanisms

During the reaction, it was clear that there were some yellow products adhering on the outer bio- membrane. Meanwhile, some other yellow products emerged in the root primarily and then grew up to the stem. After reaction, SEM pattern indicated that there was quantity of CdS nanomaterials on the outer and inner surface of mungbean sprouts. According to the

above experiment, the possible formation mechanism of CdS nanomaterials was deduced as follows:

1) When mungbean sprouts were immersed in the solution of  $S^{2-}$ , because of the concentration gradient, some  $S^{2-}$  ions on the outside of bio-membrane were transferred into the inside of mungbean sprouts by special protein and the other  $S^{2-}$  ions were absorbed on the outer membrane.

2) When the mungbean sprouts, which absorbed plenty of  $S^{2-}$ , were immersed in solution of  $Cd^{2+}$ , some  $S^{2-}$  ions in the mungbean sprouts were actively transported to the outer epidermis of mungbean sprouts and at once reacted with  $Cd^{2+}$  and produced CdS, while there were other CdS simultaneously formed on its inner surface.

3) With the increase of CdS on outer and inner surface of mungbean sprouts, crystal nucleus of  $(CdS)_m$  came into being.

4) Because of the templates operating on the outer and inner surfaces of mungbean sprouts, CdS nuclei were respectively induced to grow into different morphologies of nanotubes and nanospheres.

### 3.3 UV optical properties

UV-visible absorption spectra (Fig. 6) of CdS nanomaterials showed a strong absorption peak at about 417 nm and an obvious blue shift was observed comparing with bulk CdS at 515 nm due to size quantization effects. The absorption peak for the products shifted about for 98 nm. And it would have important scientific value on the optical filter, photochemical catalysis and special optical devices if utilizing the optical property of products.

## 4 Conclusions

In conclusion, two different morphologies of semiconductor CdS nanomaterials are successfully synthesized through living bio-membrane bi-template (mungbean sprout) during the growth of plant. This method is easy to generalize, because of its low cost and easily obtained living bio-membranes. Through this method, some new nanomaterials could be synthesized, when many kinds of living bio-membrane bi-templates could be employed. So it offers a new way to synthesize nanomaterials.

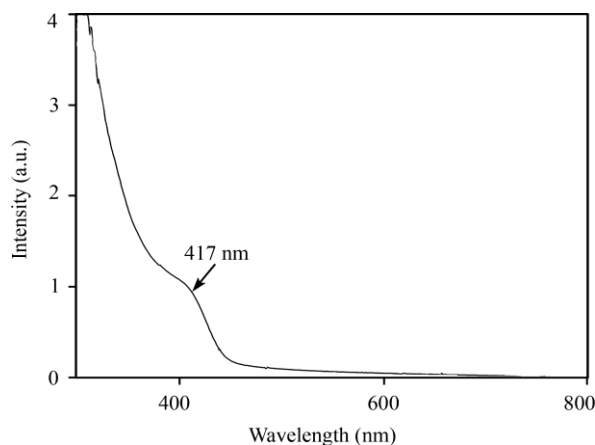


Fig. 6. UV-visible spectrum of prepared CdS nanomaterials.

## References

- [1] Peng, X. G., Manna, L., Yang, W. D. et al., Shape control of CdSe nanocrystals, *Nature*, 2000, 404: 59–61.
- [2] F. M. Shamsudin, S. Radiman, Y. Abdullah, N. A. Hamid, *Exp. Theo. NANOTECHNOLOGY* 3 (2019) 27
- [3] Wu, Q. S., Liu, J. K., Ding, Y. P., Controlled synthesis and properties of CdS quasi-nanospheres with active membrane as template, *Acta Chimica Sinica*, 2003, 61: 1824–1827.
- [4] Zhang, P., Gao, L., Cadmium sulfide nanocrystals via two-step
- [5] hydrothermal process in microemulsions: Synthesis and characterization, *J. Colloid. Inter. Sci.*, 2003, 266(2): 457–460.
- [6] Bisma Bilal, Suhaib Ahmed, Vipin Kakkar, *Exp. Theo. NANOTECHNOLOGY* 3 (2019) 33
- [7] Cao, Y. C., Wang, J. H., One-pot synthesis of high-quality
- [8] zinc-blende CdS nanocrystals, *J. Am. Chem. Soc.*, 2004, 126: 14336–14337.
- [9] Barrelet, C. J., Wu, Y., Lieber. C. M., Synthesis of CdS and ZnS nanowires using single-source molecular precursors, *J. Am. Chem. Soc.*, 2003, 125: 11498–11499.
- [10] Pedone, L., Caponetti, E., Leone, M. et al., Synthesis and charac-
- [11] terization of CdS nanoparticles embedded in a polymethyl-methacrylate matrix, *J. Colloid. Interf. Sci.*, 2005, 284: 495–500.
- [12] Naser Al-Falahy, Omar Y. K. Alani, *Exp. Theo. NANOTECHNOLOGY* 3 (2019) 45
- [13] Zhang, H., Ma, X. Y., Xu, J. et al., Synthesis of CdS nanotubes by
- [14] chemical bath deposition, *J. Cryst. Growth*, 2004, 263: 372–376.
- [15] Peng, T. Y., Yang, H. P., Dai, K. et al., Fabrication and characterization of CdS nanotube arrays in porous anodic aluminum oxide templates, *Chem. Phys. Lett.*, 2003, 379: 432–436.
- [16] Zhou, S. M., Feng, Y. S., Zhang, L. D., A two-step route to
- [17] self-assembly of CdS nanotubes via electrodeposition and dissolution, *Eur. J. Inorg. Chem.*, 2003, 1794–1797.
- [18] Mann, S., Biomimetalization and biomimetic materials chemistry, *J. Mater. Chem.*, 1995, 5: 935–946.
- [19] Baeuerlein, E., Biomimetalization of unicellular organism: An unusual membrane biochemistry for the production inorganic nano- and microstructures, *Angew Chem. Int. Ed.*, 2003, 42: 614–641.
- [20] Li, M., Schnablegger, H., Mann, S., Coupled synthesis and
- [21] self-assembly of nanoparticles to give structures with controlled organization, *Nature*, 1999, 402: 393–395.



## **Fabrication of NiO/PSi for gas sensor application prepared by chemical method**

*Aseel Mustafa Abdul Majeed\**, *Elham Jasim Mohammad*, *Itab Fadhil Hussein*

Physics Department, College of Science, Mustansiriyah University, Baghdad, Iraq

\*) Email: [aseelalaziz@uomustansiriyah.edu.iq](mailto:aseelalaziz@uomustansiriyah.edu.iq)

*Received:* 15/1/2019 / *Accepted:* 8/11/2020 / *Published:* 1/4/2020

---

In this paper NiO<sub>NPs</sub>/n-PSi/Si heterojunction for gas sensor has been investigated using chemical method and can show to enhance sensitivity. The structural properties SEM and XRD were synthesis. The sensitivity of NiO/PSi/Si heterojunction for gas sensor to H<sub>2</sub>, N<sub>2</sub> and CO gas was studied. It is obtained a high gas response is clear at 250 C at low concentration 50 ppm. The NiO NPs depended on the temperature and gas concentration.

---

**Keywords:** Nickel Oxide; Gas Sensor; Chemical Method; Sensivity; Gas Concentration.

### **1. Introduction**

Nanomaterials have significant mechanical, electronic, magnetic, thermal, catalytic properties, and optical properties, and have many wide-ranging concerns [1, 2]. Recently, the formation of nanoparticles sized crystalline metal oxides has been a growing interest because of their large surface areas, their unique properties, surface defects, and speed of propagation [3]. NiO has cubic lattice structure so it classified as an significant transition metal oxide. Nickel oxide has attracted increasing interest due to potential use in a variety of applications, such as: catalysis, battery cathodes, gas sensors, electro chromic films and magnetic materials. In addition, nickel oxide is widely used in dye sensitized photo cathodes. It exhibits anodized electrochromism, high durability and electrochemical stability, large optical density rotation and other diverse manufacturing potential [4]. In addition, nickel oxide semiconductors can be considered as distinct topics and are selected in future studies and research due to of low-cost materials such as ion storage. Due to of the effects of (quantum tunnel and size, volume, surface), it is possible to estimate that nanocrystalline have many improved properties of micrometer-sized nickel oxide particles. [4–8].

It should too be noted that it can be expand many mechanical process or chemical process to compose crystalline oxide powders in nanoscale dimensions. In many of them, the main objective is to reduce the costs of chemical synthesis and to production of materials for technological applications [9]. The purpose of this work is the synthesis of NiO nanoparticles

by the chemical precipitation process. Where, NiO/n-PSi/Si heterojunction of the gas sensor has been investigated using the chemical method.

## 2. Experimental procedure

Nickel oxide nanoparticles were prepared by chemical method at 0.1 M  $\text{Ni}(\text{NO}_3)_2 \cdot 6\text{H}_2\text{O}$  and 0.2 M of sodium hydroxide NaOH and Urea  $\text{CO}(\text{NH}_2)_2$  both of them dissolved in 50 ml double distilled water and mixed under magnetic stirring for 20 min. The precipitate was washing and calcinations at 500 C for 3 hr. In the other hand the NiO NPs deposited n-type of porous silicon by drop castle. Porous silicon fabricated by photo electro chemical etching. The morphology and gas sensor properties have been measured for NiO/PSi/c-Si heterojunction.

## 3. Results and discussion (TNR 12 bold)

The X-Ray diffraction of NiO nanoparticles is shown in figure 1. All the XRD peaks are sharp indicating to confirm a good polycrystalline of the oxide with a cubic NiO phase.

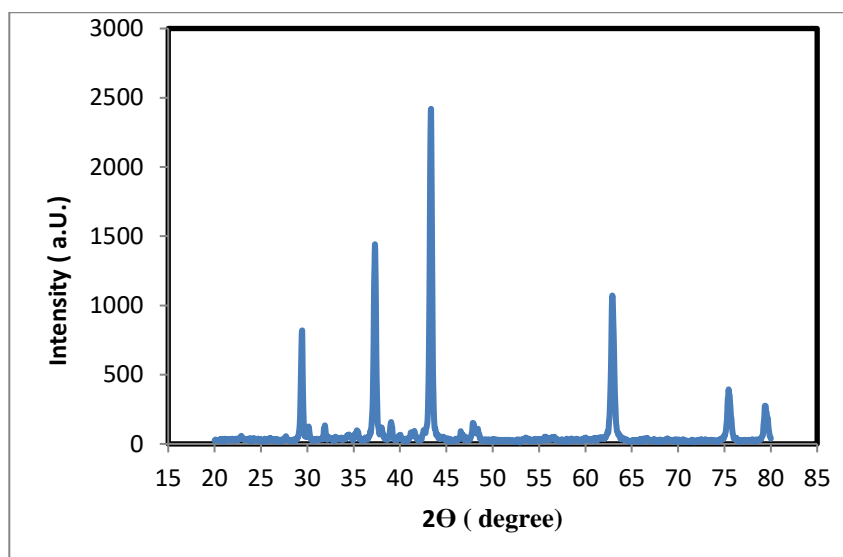


Figure 1: X-Ray diffraction of NiO NPs.

It can be observed the patterns show peaks around ( $2\theta = 29.4^\circ, 37.2^\circ, 43.3^\circ, 62.85^\circ, 75.3^\circ$  and  $79.25^\circ$ ) which are in agreement with (JCPDS) card number (004-0835). The highly intensity peak occurs at ( $2\theta = 43.3^\circ$ ) which is pointed to (200) plane. It can be noticed no other peak related to any impurity. The crystalline size of powder NiO nanoparticles was calculated using scherrer formula was found about (60 nm).

Figure 2 displays the FESEM pattern of powder NiO nanostructure. It is clear that the original morphology of NiO nanoparticles and that a spherical shape but show agglomeration of particles are occurred. The average size of NiO nanoparticles was found 40 nm.

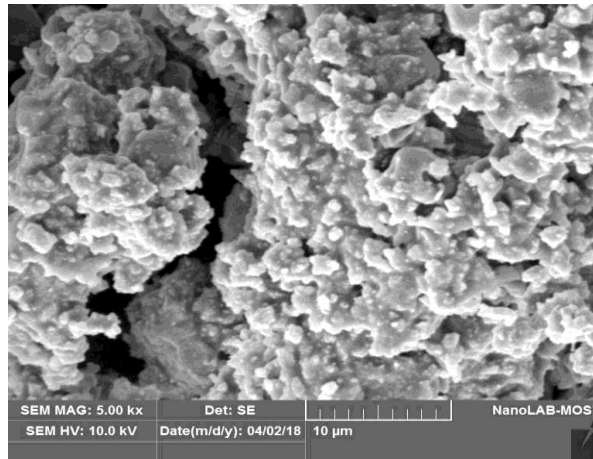


Figure 2: FESEM of NiO Nanoparticles.

The vibration properties of NiO<sub>NPs</sub>/PSi/c-Si nanostructure was investigation by Raman spectra is shown in figure 3. It is clear they have typical characteristics of strength emission and narrow band at 500 cm<sup>-1</sup>, it is to be noted that the LO mode of NiO/PSi becomes asymmetric in comparison with that of c-Si.

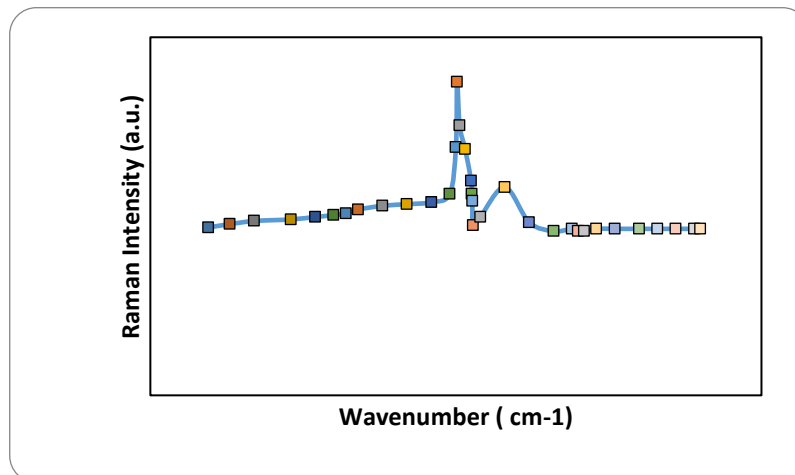


Figure 3: The vibration properties of NiO/PSi/c-Si nanostructure.

Figure 4 displays the sensitivity of NiO/PSi/c-Si sensor for H<sub>2</sub>, N<sub>2</sub>, CO gases as a function to temperature. It can be observed that the sensitivity of NiO/PSi/c-Si was increased with increasing temperature and it is found the high value is 70% for H<sub>2</sub> gas at 250<sup>0</sup> C.

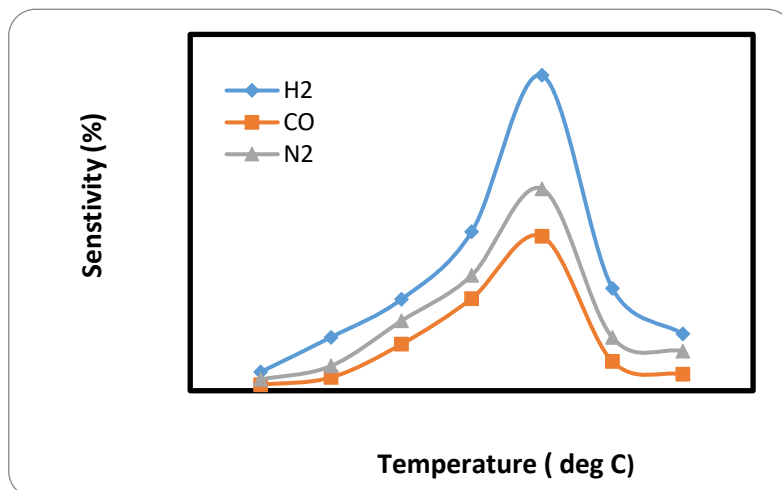


Figure 4: The sensitivity of NiO/PSi/c-Si sensor for H<sub>2</sub>, N<sub>2</sub>, CO gases as a function to temperature.

The increasing of sensitivity for gas sensor related to high surface area of NiO/PSi/c-Si and smaller grain size of NiO particles.

#### 4. Conclusions

NiO Nanoparticles n-PSi/c-Si sensor was synthesized at room temperature prepared by chemical method. The sensitivity of NiO/PSi fabrication structures to 50 ppm of H<sub>2</sub>, N<sub>2</sub>, CO gases were studied. Results of measurements showed that it is the sensor response to H<sub>2</sub> at low operating temperatures has high sensitivity compared to N<sub>2</sub> and CO. Finally, NiO nanoparticles sensitivity was dependence on the temperature.

#### Acknowledgement

The basic purpose to include acknowledgement is to pay a thankful for all those people who have supported you in carrying out your research such as financial provider, proofreading etc.

#### References

- [1] Q. Li, L.-S. Wang, B.-Y. Hu, C. Yang, L. Zhou, and L. Zhang, "Preparation and characterization of NiO nanoparticles through calcination of malate gel," *Materials Letters*, vol. 61, no. 8-9, pp. 1615–1618, (2007).
- [2] Anissa A. Putri, S. Kato, N. Kishi, T. Soga, *Exp. Theo. NANOTECHNOLOGY* 3 (2019) 61
- [3] Y. Wu, Y. He, T. Wu, T. Chen, W. Weng, and H. Wan, "Influence of some parameters on the synthesis of nanosized NiO material by modified sol-gel method," *Materials Letters*, vol. 61, no. 14-15, pp. 3174–3178, (2007).

- [4] M. El-Kemary, N. Nagy, I. El-Mehasseb Nickel oxide nanoparticles: Synthesis and spectral studies of interactions with glucose. *Mater Sci Semicond Process* 16:6, (2013).
- [5] D. Juárez, H. E. Castillo García, *Exp. Theo. NANOTECHNOLOGY* 3 (2019) 71
- [6] S. A. Needham, G. X. Wang, and H. K. Liu, “Synthesis of NiO nanotubes for use as negative electrodes in lithium ion batteries,” *Journal of Power Sources*, vol. 159, no. 1, pp. 254–257, (2006).
- [7] Y.-Z. Zheng and M.-L. Zhang, “Preparation and electrochemical properties of nickel oxide by molten-salt synthesis,” *Materials Letters*, vol. 61, no. 18, pp. 3967–3969, (2007).
- [8] Y. Wu, Y. He, T. Wu, T. Chen, W. Weng, and H. Wan, “Influence of some parameters on the synthesis of nanosized NiO material by modified sol-gel method,” *Materials Letters*, vol. 61, no. 14-15, pp. 3174–3178, (2007).
- [9] M. Gharaibeh, A. Obeidat, W. Al Awawdeh, A. Rousan, *Exp. Theo. NANOTECHNOLOGY* 3 (2019) 97



## **The Influence of RF power, pressure and substrate temperature on the energy gap to vanadium oxide at tallness wave stir 290 nm of RF sputtered**

Hanaa E. Jasim<sup>1</sup>, Mohammed K. Khalaf<sup>2,\*</sup>

<sup>1</sup>Department of Physics, College of Scientific, Tikrit University, Tikrit, Iraq

<sup>2</sup>Ministry of Science and Technology, Center of Applied Physics, Baghdad, Iraq

\*) Email: [mohammedkhkh@yahoo.com](mailto:mohammedkhkh@yahoo.com)

Received: 15/1/2019 / Accepted: 7/10/2020 / Published: 1/4/2020

In this work, the (V<sub>2</sub>O<sub>5</sub>) films were deposited on glass substrates which produce by using "radio frequency (RF)" power supply and Argon gas technique and the nano-thin film deposition is obtained from a V<sub>2</sub>O<sub>5</sub> target (5 mm in diameter and 5mm thickness) by the gradual variation of sputtering power 150 Watt and variation pressure (0.03 ,0.05 and 0.007) Torr. The Energy Gap were investigated by, UV spectroscopy at "radio frequency" (RF) power ranging from 150 Watt and and substrate temperature (359, 373,473 and 573 K) and gas pressure (0.03, 0.05 and 0.007 Torr ).The Energy Gap of the Vanadium Oxide thin film deposited by RF magnetron sputtering were analysis by UV-Visible spectroscopy shows that the average transmittance of all films in the range 40-65 %. When the thickness has been increased the transhulance was decreased from (65-40)%. The values of energy gap were decreased from (3.02-2.7 eV) with the increase of thickness the films in relation to an increase in power, The energy gap decreased (2.8 - 2.7) eV with an increase in the substrate temperature respectively and the pressure.

**Keywords:** V<sub>2</sub>O<sub>5</sub>; Energy gap; Thin films; RF Sputtering.

### **1.1 Introduction**

The development of low dimensional metal oxides is imperative due to their promising device applications such as photo detectors. Researchers have focused on the synthesis of these materials and fabricate of metal oxides Nano devices. For several years silicon-based devices have been further developed and to date have represented the core of the entire semiconductor industry [1]. The(V<sub>2</sub>O<sub>5</sub>)favoring materials for electronic and photovoltaic implementations [2]. Vanadium oxide (V<sub>2</sub>O<sub>5</sub>) is an n-type semiconductor that is both more stable and has a high

oxidation case[3]. Vanadium oxide is a material that shows a phase transition of semiconductor to metal when is heated around of a critical temperature  $257 \pm 5$  °C. Now a days the study of vanadium oxides thin film, has received a great deals because of their interesting electrical, optoelectronic properties, optical switches and the potential use of these devices as thermal sensing, and energy saving devices with in the development of smart windows They have been processed in thin film configuration to develop electrical and optical devices; especially the vanadium pent oxide (V<sub>2</sub>O<sub>5</sub>), a wide band gap and n-type semiconductor material [4] . There has been tremendous recent interest in V<sub>2</sub>O<sub>5</sub> in view of its material characteristics, which can be readily integrated into many scientific and technological applications. These include applications in electro chromic and photochromic devices, electronic information displays, color memory devices, micro batteries and smart windows, chemical sensing, catalysis, and optical / electrical switching, photo detectors [5]. The V<sub>2</sub>O<sub>5</sub> is an effective material in the industrialization of many solid state devices, such as the sensors, optical-electrical switches [6].The (V<sub>2</sub>O<sub>5</sub>) is the most stable juncture among all mangle phases (V<sub>n</sub>O<sub>2n+1</sub>), exhibits interesting electrical, optical and electrochemical properties[7].V<sub>2</sub>O<sub>5</sub>" thin films have been prepared by various methods such as sputtering [8], vacuum evaporation[9], pulsed laser deposition [9], sol-gel [10], chemical vapor deposition[11], spray pyrolysis" [12], thermal evaporation [13]and electron beam evaporation [14 ]. Nanoparticle V<sub>2</sub>O<sub>5</sub> thin films are used to overcome this issue by increasing the surface area and decreasing the diffusion distance [15 ].

### 1.2.1 Experimental

In this work, V<sub>2</sub>O<sub>5</sub> films were prepared by the RF magnetron system (CRC600 CO. Manufactured in the USA).Prepared thin films on glass Substrate in different power, pressure and substrate temperatures . The chamber was evacuated under low pressure ( $3 \times 10^{-5}$ ) Torr. The glass slides were sequentially cleaned in an ultrasonic bath with acetone and ethanol. Finally they were rinsed with distilled water and dried. . The optical properties measurements for (V<sub>2</sub>O<sub>5</sub>) thin films obtained by using the UV-Visible recording Spectrometer (UV-2601 PC Shimadzu software 1700, 1650), made in Japan. The thickness of the films has been calculated by using Device the FT-650 Film Thickness (FT) Probe System.. Use the V<sub>2</sub>O<sub>5</sub> deposition of RF Sputtering in pure argon gas (99.9%) with pressure (0.03,0.05 and 0.007Torr ). With different of RF power (75, 100, 125, and 150 watts), with various substrate temperatures were ( 359, 373, 473 and 573 K ) respectively.

### 1.2.2 RF magnetron Sputtering System

The CRC-600 system is shown in Figure (1-2). It consists of a vacuum system including a turbo-molecular pump, direct drive oil sealed rotary vacuum pump or dry scroll rotary pump, a quartz crystal thickness monitor , a stainless steel chamber with viewport, planar magnetron sputtering source (s) ,a (DC) and or (RF) power supply and substrate with and without rotation including temperature controller.



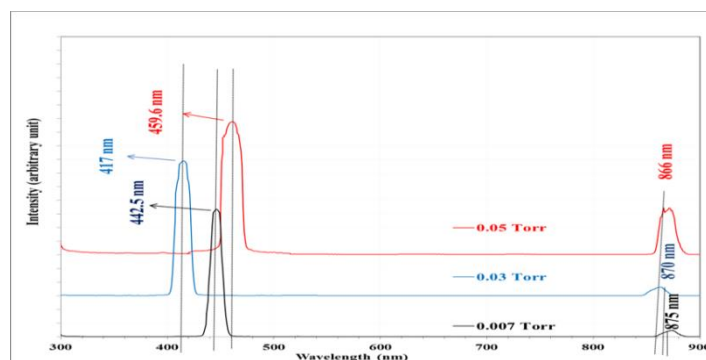
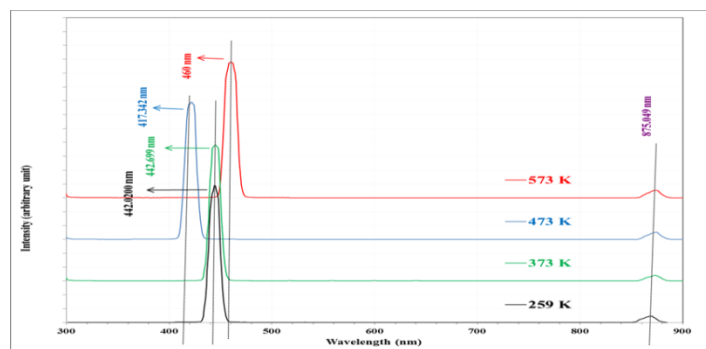
Figure (1-2): The CRC 600 magnetron sputtering system.

### 1.3 Results and Discussions

#### Optical Properties

##### 1-4. Photoluminescence (PL)

Figure(1-2). shows the PL spectra of V2O5 thin films deposited at various ( rf power, pressure and substrate temperature), recorded at room temperature . It was the excitation wavelength 290 nm for every thin films. PL emission peaks at wavelength ranges 400 - 470 nm i.e. all absorption peaks occur in the visible region. The optical energy gap values have been calculated from the emission wavelength as in the table (1-1). The calculated energy gap values are in good agreement with those obtained from UV spectrophotometer. and agreement with reference [207,208].



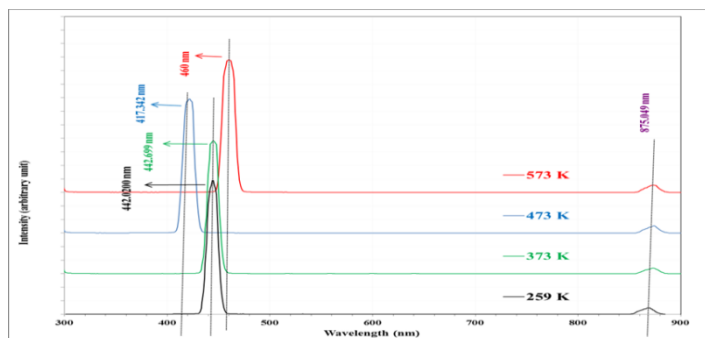


**Figure (1-2):** PL emission spectra of V2O5 thin films deposited at

.Different sputtering power, working pressure and temperature substrate

**Table (1-1):** Wavelength data and values Energy gap optical of V2O5 thin films deposited at Different sputtering power, working pressure and temperature substrate.

	Sample	Wavelength (nm)	Energy gap (eV)
<b>P(W)</b>	75	0.94410	3,023
	100	0.45415	2,98
	152	416,036	2,98
	150	417,192	2,97
<b>Pressure (Torr)</b>	0.007	442,5	2,8
	0.03	417	2,9
	0.05	459,6	2,69
<b>Temp (K)</b>	359	442,020	2,8
	373	442,69	2,8
	473	417,347	2,9
	573	460	2,7

**Conclusions:**

The optical properties of the (V2O5) thin films deposited by (RF) magnetron sputtering shows a decrement in transmission spectra with increase RF power as result of increasing films thicknesses, with decreased the energy band gap.

**Acknowledgement**

The basic purpose to include acknowledgement is to pay a thankful for all those people who have supported you in carrying out your research such as financial provider, proofreading etc.

**References:**

[1] Mohammed Jwair Dathan , Preparation and Characterization of Nanoparticles of Some Elements by Using Plasma Sputtering for Medical Application . PhD. Thesis .University of Tikrit College of Education for Pure Science ,(2017) .

- [2] S. Nivetha, R. Perumalsamy, A. Ayeshamariam, A. Mohamed Saleem, M. Karunanithy, M. Jayachandran, *Exp. Theo. NANOTECHNOLOGY* 3 (2019) 109
- [3] S. Beke, “A review of the growth of V<sub>2</sub>O<sub>5</sub> films from 1885 to 2010,” *Thin Solid Films*, vol. 519, no. 6, pp. 1761–1771, Jan. 2011.
- [4] J. Hamed, H. Abd, R. Muzahim, *Exp. Theo. NANOTECHNOLOGY* 3 (2019) 131
- [5] C. V. Ramana, R. J. Smith, O. M. Hussain, and C. M. Julien Growth and surface characterization of V<sub>2</sub>O<sub>5</sub> thin films made by pulsed-laser deposition Citation: *Journal of Vacuum Science & Technology A* 22, 2453 (2004); doi: 10.1116/1.1809123
- [6] V. Petkov, P. Y. Zavalij, S. Lutta, M. S. Whittingham, V. Parvanov, and S. Shastri, “Structure beyond Bragg: Study of V<sub>2</sub>O<sub>5</sub> nanotubes,” *Phys. Rev. B*, vol. 69, no. 8, p. 085410, Feb. 2004
- [7] Tagreed K. Hamad, Alaa H. Ali, Alaa J. Ghazai, Hussein T. Salloom, *Exp. Theo. NANOTECHNOLOGY* 3 (2019) 149
- [8] Ottaviano, A. Pennisi, F. Simone, and A. M. Salvi, “RF sputtered electrochromic V<sub>2</sub>O<sub>5</sub> films,” *Opt. Mater. (Amst.)*, vol. 27, no. 2, pp. 307–313, Nov. 2004.
- [9] Y. Shimizu, K. Nagase, N. Miura, and N. Yamazoe, “Electrochromic properties of spin-coated V<sub>2</sub>O<sub>5</sub> thin films,” *Solid State Ionics*, vol. 53–56, pp. 490–495, Jul. 1992
- [10] G. Wu et al., “Optical absorption edge evolution of vanadium pentoxide films during lithium intercalation,” *Thin Solid Films*, vol. 485, no. 1–2, pp. 284–289, Aug. 2005.
- [11] N. T. B. Bay et al., “Optical and electrochemical properties of vanadium pentoxide gel thin films,” *J. Appl. Phys.*, vol. 80, no. 12, p. 7041, Aug. 1998.
- [12] C. Julien, E. Haro-Poniatowski, M. Camacho-López, L. Escobar-Alarcón, and J. Jiménez-Jarquín, “Growth of V<sub>2</sub>O<sub>5</sub> thin films by pulsed laser deposition and their applications in lithium microbatteries,” *Mater. Sci. Eng. B*, vol. 65, no. 3, pp. 170–176, Nov. 1999.
- [13] C. Ramana, O. Hussain, and B. S. Naidu, “Growth and structure of electron beam evaporated V<sub>2</sub>O<sub>5</sub> thin films,” *Mater. Chem. Phys.*, vol. 50, no. 3, pp. 195–199, Oct. 1997



# **Study the effect of different dilutions from filtrates of two fungi *Alternaria alternata* and *Aspergillus flavus* on the ground Beetles adults (carabidae: Coleoptera) *Harpalus rufipes***

*Athraa H. Jasim Al-Rahmany*

Department of Biology, College of Education, University of Samarra, Samarra, Iraq

\*) Email: [athraabiologyalrahmany@gmail.com](mailto:athraabiologyalrahmany@gmail.com)

*Received: 2/2/2019 / Accepted: 4/9/2020 / Published: 1/4/2020*

---

The present study was conducted to test the efficiency and effectiveness of different dilutions of filtrate innate from *A. flavus*, *Alternaria alternata* (25%, 50%, 75%, 100%) on the adult insect ground beetle, results showed no significant effect dilutions filtrate innate from *A. flavus*, *Alternaria alternata* in the decimation adults ground beetle *Harpalus rufipes* and 100% concentration may outweigh the rest of the other dilutions to give a higher proportion of the loss amounted to (80%, 100%) at 24.48 hours of treatment for a leaky mildew fungus *A. flavus* and (70% 0.90%) at 24 hours, 48 hours of treatment for a leaky mushroom fungus *Alternaria alternata* As for dilutions other has given dilution of 25%, 50%, 75% the proportion of the loss amounted to ( 0.0 % , 10 % , 20%) and , respectively, after 24 hours of treatment, the proportion of the loss (10% , 20% , 50%) and respectively after 48 hours of labor for a leaky mildew *A. flavus* As for the other dilutions leaky mildew fungus *Alternaria alternata* ( 25 % , 50 % , 75% ) was given to the proportion of the loss ( 0.0 % , 10 % , 30 % ) after 24 hours of treatment , respectively (10% .20 % .60 % ) after 48 hours of treatment , respectively.

---

**Keywords:** Fungi; Concentration; Analysis.

## **1.Introduction**

Ground beetles Carabidae are the most important insects of economic interest. They are belonged to a large family of coleoptera insects and they are one of the largest animal kingdom their known types of coleoptera estimated (350,000) types and about of these known insects are beetles vary significantly and ecologically and vary in size from one to a very large size of 3 cm [1]. The ground beetles are harmful agricultural pests and the blight is attributed to the larvae and imago phases [2]. Many of the beetles prey to other insects (aphids) and there are other harmful species to the plants as the piercers of buds, fruit, stems and leaves.

They feed on dry materias, stocks as flour, cereals and clothes. Some of them are considered carnivorous[ 3].

The type of this family are common and many,including the genus *Harpalus rufipes* that can be seen on the ground running quickly or hidden beneath the rock ,all these beetles are predatoy ,eating all animal products such as leather ,wool silk ,feathers ,hair ,dried meat,dead insects and dried plant materials .in addition to being awool carpet biting ,it is called carpet beetle[4]. The *Harpalus rufipes* has a nocturnal activity and its larvae are also found on the ground where they are moving effectively and are sever predatory.The imago is characterized by a nematoform and consisted of (11)articles and the wrist is form (5) articles.This insect passed the winter in the soil cavaties or under the rocks or between the plant wastes or any hidden holes and went out in spring and put its egg in the soil [5;6].

The eggs hatched out the active and predatory small larvae and after anumber of moultings the larvae is ripen in one or two weeks or three weeks and entered the soil to be a virgin taking a cycle of eggs to the full imago in fire or six weeks ,but the imago remained in the soil and sometimes lived for some years and laid eggs evey year .This family is considered from the useful insects and it plays a great role in the biological control in fields and farms where it preys many agricultural pests[7;8]. The study objective:Due to the economic damage caused by this insect *Harpalus rufipes*.The abstracts of *Alternaria alternata* and *Aspergillus flavus* are used as a means of biological fighting to decrease the damage caused by this insect.AS these instracts contain a higher ratio of toxins called Aflatoxins AB having a higher capacity of calling the insect and breaking down its bodies[9].

## 2. Method of analysis :-

Table 1 The Material and devices used in the experiment

## 3.Experimental procedure

### 3.1. Collecting of an insect Method .

The 500 ground beetles carbidue were gathered from genus *Harpalus rufipes* in July .This process was continuous to one week from differents sites in Samarra where they took from various holes in the soil ,houses and some farms by hands and put them in to the sterilized plastic cans[1].

### 3.2.The cultura Media used for growing fungi

Prepare the browth by melting (39)gram of PDA mixture in a distill water bath in a conical flask of (2) litres and put it in water bath and add to it (250)mg of chloramphenicol.put the medium in an autoclave in 121C and pressure of 15 pound /inch for 20 minutes.This is used for isolating and purifing the fungi to use in the next experiments[10].

### 3.3.potato dextrose browth (PDB)

Prepare the medium from cooking (200gram potato ) of potato cutting into small piece with (500ml)of distil water for(2) minutes in a beaker .The cooked potato filterd with a piece of steril ganuze and add a 20 grams of dextrose and complete the volume to a litre with distilled water and implant the susernatant in glass flasks of (250)ml and a rate of (150)ml per flask .The media were sterilized by an autoclave at 121C ,and and pressure of 15 pound /inch for 20 minutes.Use the medium to prepare the fungal supernatant of the fungus *Aspergillus flavus* and *Alternaria alternata* [10].

### 3.4. potato dextrose broth (PDB)

Prepare the PDB and put it in a conical flask of 250ml with amount of 15ml /flask and then add chloramphenicol of 25 mg /ml and incubate each flask three tablets each diameter of 5mm with a cork borer from the edge of the fungal colonies purified on the middle of PDA and extract after 7 days for *A. flavus* and *A.alternata*. The flasks are incubated at  $\pm 25^{\circ}\text{C}$  considering shaking the flasks each (3-4) days to distribute the fungal growth and after (28) days ;the vaccine was filtered by using filtration papers and by the air discharge. The refiltration was done by the accurate filterer. The concentrations (25%,50%,75%,100%) are Prepared from the fungal supernatant *A.flavus* and *A.alternata* and the concentrations of the supernatant are used in the following experiments[11].

### 3.5.Valuation of the toxin efficacy of different dilutions taken from the fungal supernatant for *A.flavus* and *A.alternata* isolated in labo on growing and developing the ground beetles adults genus *Harpalus rufipes* .

1-The effect of the fungal supernatant for *A.flavus* and *A.alternata* on the ground beetles adults genus *Harpalus rufipes* under ( $\pm 27$ ) C and relative humidity 5% .The 25, insects are taken for each concentration of the fungal supernatant for two fungi (25%,50%,75%,100%) at a rate 5ml by using a half liter plastic sprayer. The insects that were put in sterile plastic cans were sprayed at a distance (5cm). The number of dead adults is calculated in each concentration and for each fungal supernatant respectively.

### 3.6.The statistical Analysis :-

Data are analyzed statistically by (Anova) analysis on way variation Test and by applying the statistical program (Minitab) and the arithmetic averages of the coefficients were compared with the use of Duncans multiple range test at probability level 0.05[12].

## 4. Results and discussion

The results in table (1) showed the ratio of killing is directly proportional to the concentration, the higher the concentration ,the higher the killing rate . The rate of killing concentration (25%) is zero within 24 hours of treatment ,while the killing rate was 90% at 100% concentration within 24 hours of treatment , but in 48 hours of treatments ,the killing rate was 100% at 100 concentration in comparison with the control sample that did not have a killing rate within 24 and 48 hours of treatment ,Thus,through these results,it is clear that there is a significant effect on the fungal supernatant dilutions of *A. flavus* (25%,50%,75%,100%) in the ground beetles adults genus *Harpalus rufipes* .The concentration (100%) could be higher than the rest , which is different in the effect on the death of the ground beetles adults ,giving the highest ratio of death at 95%.It is significantly different from the rates of death in the other dilutions , which differ from each other in impact .As for the effect of periods in death ratios after the treatments .They highest death rate in the ground beetles adults was after 48 hours of treatments 52.5% and it is significantly different from the proportions of the loss after 24 hours of treatments ,which amounted to 35%.The interference between the dilutions and periods showed that the highest rate of death occurred after 48 hours after treatments at 100% concentration ,the lowest rate of death occurred after 48 hours of treatments at the 25% dilution,which reached 10% . The mechanism of lethal effect of the fungal supernatant for *A. flavus* on the ground beetles adults was due to several causes . One of the most important Causes is the effect of this toxin on the gas exchange between the insect and the environment.

Thus lead to the death of insect or some of the toxins are combined in this fungus with cytoplasm of the insect body wall and thus lead to poisoning it and then its death .The results of our study conform to the results of many researchers such as[13].which explained the toxic

efficacy of the fungal supernatant for *A. flavus* in killing and analyzing the various tissues of the body and stopping the work of all the cells and tissues of different life phases of the *Culex pipiens* of. The study Ali [12]. which explained the efficacy of *Beauveria* for the most important effects observed during treating the ground beetles adults, genus *Harpalus rufipes* with the fungal supernatant of *A. flavus*[14]. It has resulted in very high killing and deformation ratios due to the overlapping of toxic compounds of the fungal supernatant with vital system of the gastro intestinal cells with some of the main components within the gastro intestinal tract such as lipid resulting in the decompositions of the digestive tract tissue as well as fracturing, twisting and blocking the bronchi and obstructing respiratory openings as a result of gathering toxic substances (Systematic toxins) because they damaged and analyzed all parts of body organ and that is what has been proved in our study[15].

**Table 2 The effect of various concentration of the fungal supernatant for *A. flavus* on the ground beetles adults *Harpalus rufipes* at  $\pm 38$  C**

Concentration/time	24hours	48 hours	Average of concentration effect	Average of supernatant TYPE effect
0	0	0	0	
25%	0.0g	10f	5c	38.8a
50%	10f	20e	15c	
75%	30d	60g	45b	
100%	80b	100a	90a	
Average of time effect	a(30.0)B	b(47.5)A		

**The similar small letters in on column mean that no significant differences between them**

It is observed from (3) there is a significant effect of the various dilutions for the fungal supernatant *A.alternata* on the ground beetles adults *H.rufipes*. The concentration 100% is the highest in giving the highest ratio of death amounted to 90%. It is significantly different from the ratios in other dilutions that are differed significantly from each other in tracing also AS for the effect of periods in death the ratios after the treatments the highest death rate was found in the ground beetles *H.rufipes* after 48 hours of treatment, which amounted to 47.5% and is significantly different from the rates of loss after 24 hours of treatment either from the overlap between the dilutions and the period. It is obvious that the highest death rate was after 48 hours of treatment at 100% concentration, which reached 100%. The lowest death rate was 10% after 48 hours of treatment at 25% concentration. The mechanism of lethal effect of the different concentrations of the fungal supernatant *A.alternata* on the ground beetles adults *H.rufipes*. This is due to many causes; and the fact the toxins resulting from this fungus combined with cytoplasm of the insect body wall cells. thus lead to its poisoning as well as that some fungi including *A.alternata* have the ability to produce protease, lipase and chitinase enzymes which play a significant role in the destructions of the body wall[16].

It is also due to the entry of large amounts of toxins produced by fungi with nutrition, which causes them enter the digestive tract of insect leading to its poisoning [17;18]. This results in closure of the respiratory openings and then it is death. From these findings, it is clear that the rate of loss is directly proportional to the concentration of the fungal supernatant, and the higher the ratio of killing which is consistent with the study carried out by [19]. at treatment with house flies adults with different weights of fungi *A. alternata* because the death rates are increasing with weight of fungus. They amounted to 100% at weight 5g and 40% at weight

1grm .This is consistent with the results of our study and ours with[11], and explained that the increase of spraying the nymphs and adults of white fly with supernatant of *Aspergillus* ,pvigerl .distrupted the activity of the tissues and thus effects their life performance leading to their death , as observed when treating the *H .rufipes* with various concentrations of the fungal supernatant *A. alternate* that led to blacken or patches on the wall of the insects body .This is called the blakenning .Also,the beetles that treated with the fungal supernatant *A. alternate* ,they have been waekened or paralysed completely by the toxin transformed by fungus (Aflatoxins ,one of the most dangerous toxins with hight sucse tibility in destructing tissues and cells of the organisms body . They most important toxins are B1G1[20]. ,and these symbols have to do with the colour of any two compounds under the ultraviolet rays .[B] is for blue and [G] is for green .The results of our study refered to it [20;21] .that the most importance evidence adopted in the diagnosis of the fungal infections in insects is the change of the bodies colour and distability to lay eggs ,this is consistent with the results of our study [22].

**Table 3 The effect of different concentrations of the fungal supernatant *Alternaria alternata* on the ground beetles *H .rufipes* at 38±2 C .**

Concentration/time	24hours	48 hours	Average of concentration effectc	Average of supernatant TYPE effec
0	0	0	0	
25%	0.0g	10f	5c	33.8b
50%	10f	20e	15c	
75%	20d	50c	35a	
100%	70b	90a	80a	
Average of time effect	B(25.0)B	B(42.5)A		

## 5. Conclusions

In experimental study:- 1-The fungal supernatants are systematic toxin fungi on insects .

2- The fungal supernatants of *A.flavus* and *A. alternata* are effective in killing and analyzing various tissues and organs of *H .rufipes* .

4-It is noticeable that the different effect of dilutions of the used fungal supernatants is contrasted .They only concentration 100% is effective and affected more than others .

## Acknowledgement

The basic purpose to include acknowledgement is to pay a thankful for all those people who have supported you in carrying out your research such as financial provider, proofreading etc.

## References

- [1] S. E. Jasim, M. A. Jusoh, R. Jose, Exp. Theo. NANOTECHNOLOGY 3 (2019) 65
- [2] J., Al-huluw , General Entomology .Dar al-salamah for publishing and distribution .Amman ,Jordan.print 1.pp78-79, (2009).
- [3] P. Y. Feng, L-Q. Fa, C-G. Wang, Exp. Theo. NANOTECHNOLOGY 3 (2019) 169
- [4]E. Saad , Ground beetle *Harpalus rufipes* important& damage pp:2, (2015).

- [5] K. Hamza, Biological resistance of pests. Dar Alkutub for printing & publishing. University of Mosul. pp:440, (1992).
- [6] G.I. Knols, B., Bukhari. T., Farent, Entomopathogenic fungi as the next generation control agents against malaria mosquitoes – center f4 -214- amestrdam, (2010).
- [7] S. Chernkov, P. Badov, Exp. Theo. NANOTECHNOLOGY 3 (2019) 175
- [8] N., Aayed, M., wjih, A., Hadi, Effect different dilutions from filtrate fungal *Aspergillus niger* in Nympha and adult insect *Bemicia tabaci* (Homoptera). Al Rafidain Journal of Agricultural sciences. 2(3):pp:167183, (2012).
- [9] P., Guillebeau, N., Hinkle, p., Robret, summary of losses from insect damage and costs of control in Georgia, Agr. and environ. Sci. miscellaneous pub. no. 106-60 p, (2005).
- [10] M., Abdulhamid, fungi and fungal toxins. publishing house of university. Cairo. Egypt. pp:2, (1988).
- [11] M., Amin, Isolation and identification soil fungi in different regions from Basrah city and its morbidity test on insect whitefly *Bemicia tabaci* and *Aphis fabae* phd. thesis. since college University of Basrah. pp2-3, (2007).
- [12] M. Khashiea, K. Abdulaziz, Design and analysis of Stastical experiments. Dar Alkutub for printing & publishing. University of Mosul. pp55, (1980).
- [13] H., Abdulhameed, H., Athraa, Study the effect of the different dilutions From the fungous filtrate of the fungus *Aspergillus flavus* on growth and development of the aqueous Phases in the matured insect of mosquito *Culex pipiens pipiens L.* Culicidae (Forsk.) Second international scientific conference. Agricultural of College. University of karkuk, (2013).
- [14] I., Mahmud, foundations of modern fungi. Ibn alatheer house for printing and silk. University of Mosul. print :1, (2011).
- [15] E.J., Scolte, B.G., knols, R.A., Sason, W. Taken, Entomopathogenic fungi for mosquito control (arevien) J. insect. sci. 4 (19) ; 1-24, (2004).
- [16] R., Leger, J. Joshi, I., bidochka, M., Rizzo, N., W., Roberts, flavireidae and *Beauveria bassiana* during fungal invasion of host cuticle. environ. Microbial. 62; 407-912, (1996).
- [17] B., Bulter, f., jerrg, M., frank & runika, M., jame, *Musca domestica* as pathogenic of bacteria. department of Entomology. p.o. box 110620. Universi of florida. pp:-132, (2011).
- [18] D., Bouer, J.p. Ret, D, Lemperiere, P., giranvel, response of *Aedes aegypti* (Diptera : culicidae) larval three xenobiohc exposure : larval to larence. chapter. 25. pp:-(2), (2006).
- [19] H., Abdulhameed, H. Athraa, Effect of contaminating the different weights of the fungus *Alternaria alternata* in destruction adults *Musca domestica* (Diptera: Muscidae). Second

international scientific conference. University of Kufa. College of Education Girls  
.Department of Biology . PP3-10,(2015).

[20] N. ,Abdulaziz., Mycotoxins. Dar Digla printing & publishing . pp: 1:5, (2011).

[21] D.G., Bougas, J.G. , pendland, principles of insect pathology, kluwer akademis. Publisher  
Boston/ Dorderaut .Londen. P. 537 , (1998).

[22] k., Theiling, b . Mlcrofta , pesticide side effects arthropod natural enemies : adata base  
summargagri . environ . 21 : 191 -218 ,( 1988) .



## Evaluation of uranium concentration in soil samples of Al-Diwaniya governorates using ICP-mass techniques

Thaer M. Salman<sup>1</sup>, Abbas A. Sweaf<sup>1</sup>, Hussein Ali Noor<sup>2</sup>, Jihad S. Addasi<sup>3</sup>, M. Jadan<sup>4,\*</sup>

<sup>1</sup>Department of Physics, College of Education for Pure Science, University of Basrah, Basrah, Iraq

<sup>2</sup>Department of Physics, College of Education, University of Qadisiyah, AL-Diwaniyah, Iraq

<sup>3</sup>Department of Applied Physics, College of Science, Tafila Technical University, 66110 Tafila, Jordan

<sup>4</sup>Department of Physics, College of Science, Imam Abdulrahman Bin Faisal University, P.O. Box 1982, 31441 Dammam, Saudi Arabia

Received: 2 July 2019 / Accepted: 2 September 2019 / Published: 1 May 2020

The present work is concerned with the measurements of uranium concentrations in forty nine surface soils samples from selected locations (some of them were measured for the first time as far as authors know) in Al-Diwaniyah governorate by using ICP-Mass (inductively coupled plasma mass spectrometry) was found to be ranging from 2.78 ppm in (Al-shamr 2) to 7.99 ppm in (Al-shawfa) in soils. The results are presented and compared with other studies. The measurements of uranium concentration of soils samples measured had a uranium content of less than 100 ppm, a concentration that characterizes overburden and tailings quality, rather than minable reserves. This paper presents and evaluates the concentration of uranium in Al-Diwaniya Governorates. The study further reveals that 49 surface soil samples have uranium below detection limit. The present results have shown that the uranium concentrations in the studied surface soils samples were less than the allowed value (11.7 ppm) recommended by UNSCEAR, 1993.

**Keywords:** Uranium, Soil samples, ICP-Mass, Al-Diwaniya Governorates.

### 1. INTRODUCTION

Uranium is a very widely distributed element in the earth's crust, is presented naturally everywhere in soil, sand and rock in various concentration from one place to another. Uranium is a radioactive and chemical element, represents by (U) symbol, and it is a heavy metal with a very high density (18.95 g/cm<sup>3</sup>, 1.7 times higher than lead's density of 11.35 g/cm<sup>3</sup>). Metallic uranium has a high melting point (1132 °C) and boiling point (4131 °C), has a tensile strength

similar to most steels and it is chemically very reactive [1]. Natural uranium consists of three isotopes. Their concentrations by mass are  $^{238}\text{U}$  99.276%,  $^{235}\text{U}$  0.718% and  $^{234}\text{U}$  0.0056% [2-4]. Uranium is a naturally occurring element with an average abundance in the earth crust of about 2 mg per kg (range 0.1 to 20 mg per kg). It is more abundant than silver or gold. It has adverse effects on the human health. The major health effect of uranium is its chemical toxicity, rather than its radiological hazard [5-8]. The chemical toxicity was thought to be similar to lead. The elemental and isotopic abundances of uranium have been extensively used to explore biogeochemical and physical processes in diverse fields of the Earth sciences [9]. Low uranium concentrations ([U]) and low abundances of  $^{234}\text{U}$  in most natural samples, however, constrain many applications due to measurement limitations. Alpha spectrometry methods have been used to quantify uranium radionuclides for five decades [10,11] but large sample size requirements and the advent of techniques with vastly improved throughput and analytical precision have pushed alpha-counting techniques toward obsolescence. Monitoring uranium content in environmental samples is typically performed using alpha spectrometry and inductively coupled plasma atomic emission spectrometry (ICP-AES). However, due to the relatively low sensitivity of these techniques for uranium, a large number of samples and long measurement times are generally required to obtain reliable results. Moreover, the accuracy of alpha spectrometry allows only a rough estimation of uranium levels. Mass spectrometry, which boasts both high sensitivity and accuracy, is considered one of the best alternatives to the aforementioned methods [12,13]. The general aim is to investigate the complex interactions and exchanges with soil samples, and to estimate how much hazards brought with soils. In fact, the study area is located inside Al-Diwaniya Governorate which is located in the extreme southern part of Iraq, see Figure 1.

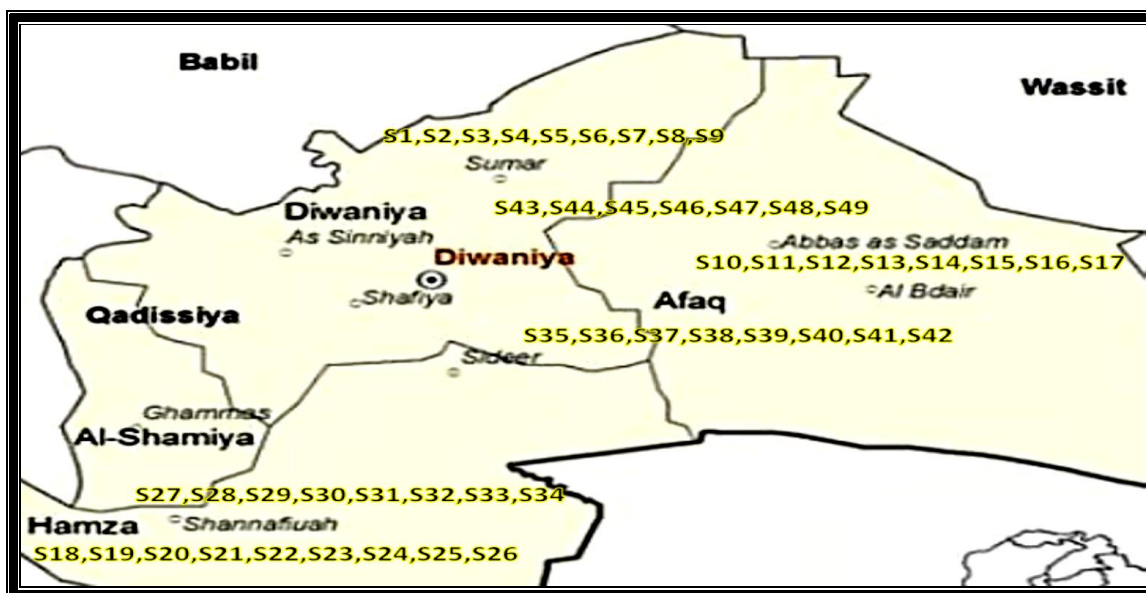


**Figure 1** Al-Diwaniya Governorate, dots represent the places where samples taken from, numbering in station number (S).

## 2-MATERIAL AND METHODS

### 2.1 Collection of soil sample

Forty nine samples of soils distributed in Al- Diwaniya center, Al-ghanam, Al-shamr, Al-barakat, Al-aqarae, Al-khazraj, Alamisar Al-farahina, Al-thawra, Alsabahi, Abu-shrifafa, Alsinidal, Alhuriya, Aljumhuriu, Al-sdeer, Al-shawfa, Al-ttabu, Al-askari, Al-karama, Aldawr Alshanaafia, Almuealimin, Alkhasf, Alsaray, Al-fawar, Al-daraeia, Afak Center, Aleayn,

fadalallah, Alkarama, alsaray and Al- dighara districts in Al- Diwaniya governorate were taken from location of study, from depth (5-15) cm than the sample s were cleaned. . dried in oven at 70 C° for few hours finally they were powdered and sifted by using special sieve (75)  $\mu\text{m}$  in diameter [7]

## 2.2 Plasma-source MS

The ICP–MS is the result of coupling an extremely efficient ion source (ICP) with an extremely sensitive ion detection technique (MS). Both ICP–OES and ICP–MS share ICP as the ionization source and both have the same systems for introduction. In the case of ICP–MS, ions generated in the plasma (at atmospheric pressure) pass through an assembly of a sampler and a skimmer cone to a highly evacuated MS area. An ion optic system focuses ions to the MS which measures mass-to-charge ratios of the ion(s) of interest. The commonly used quadruple MS acts as a mass filter that allows only a given mass-to-charge ratio of ions to pass to the detector. The ions passing through the MS are deflected to an ion detector that converts the ionic energy to electric energy which forms the basis for the measurement of the analytic concentration. For multielement analyses, the parameters are sequentially changed to allow the passage of other ions of differing mass-to-charge ratios to the detector. Thus, multielement analysis by ICP–MS is, in fact, sequential single element analysis. The advantages of ICP–MS over other methods are higher sensitivity, lower detection limits and simultaneous measurement of U concentrations and U isotope ratios. The ICP–MS can carry out U determination by the isotope dilution method which is considered the most precise for quantitative analysis. Some researchers have used FI technique for separation/ preconcentration of U and determination by the isotope dilution method to improve sensitivity and precision and detection capabilities [14, 15].

## 3. RESULTS AND DISCUSSION

The results for Uranium concentration in Soil samples determined in the present study are presented in Table 1 which are collected from some areas in Al-Diwaniya Governorate, southern Iraq. For the measurement of Uranium concentration level soils, table 1 and Fig. 2, reflect the fact that, there was some less than level of Uranium concentration in this soil samples less than from the U.S Environmental Protection Agency (EPA) . The results for these 49 samples categorized into 49 locations, from S1 to S49, shown in Fig. 2. Uranium content found maximum (7.99ppm) in Al-shawfa belt and minimum (2.78ppm) was recorded in Al-shamr2belt. Out of the 49 soil samples 4 samples recorded higher which are beginning from 7.12ppm to 7.99 ppm while the 16 soil samples are beginning from 6.04 ppm to 6.95 ppm but 24 soil samples which are beginning from 4.01 ppm to 5.97 ppm and 5 soils samples are beginning from 2.78 ppm to 3.97 ppm than the prescribed EPA limit (30 ppm). The maximum contaminant level (MCL) of uranium was determined to be about 30  $\mu\text{g/L}$  by U.S Environmental Protection Agency (EPA)[16].it is important to reliably monitor uranium concentrations in environmental samples. Monitoring uranium content in environmental samples is typically performed using alpha spectrometry and inductively coupled plasma atomic emission spectrometry (ICP-AES). However, due to the relatively low sensitivity of these techniques for uranium, a large number of samples and long measurement times are generally required to obtain reliable results. Moreover, the accuracy of alpha spectrometry allows only a rough estimation of uranium levels. Mass spectrometry, which boasts both high sensitivity and accuracy, is considered one of the best alternatives to the aforementioned methods [12,13]. The results of this study were compared with a study of researchers Abd alsattar K. Hashim and Laith A. Najam Measurement of Uranium Concentrations, Radium

Content and Radon Exhalation Rate in Iraqi Building Materials Samples, Uranium content in these samples has been found, it is varying from 0.074 to 5.055 ppm with a mean value of 0.755ppm The selection of these regions to measure the ratio of uranium, depending on several factors, the most important are The increase in uranium concentrations in some areas around the Diwaniyah center, due to the recent war in those areas and the remnants of nuclear weapons [11].

**Table 1** Measurements of Uranium concentration in soil samples from different areas of Al-Diwaniya Governorate by using ICP-Mass

No of site	Location of sample	Concentration of Uranum by ICP-mass (ppm)
S1	Al-ghanam 1	5.01
S2	Al-shamr 1	4.11
S3	Al-barakat 1	4.07
S4	Al-aqarae	6.34
S5	Al-khazraj	6.22
S6	Alamisar	3.11
S7	Al-ghanam 2	7.12
S8	Al-shamr 2	2.78
S9	Al-barakat 2	4.84
S10	Al-farahina	6.93
S11	Al-thawra	6.69
S12	Alsabahi	5.66
S13	Albu-shrifa	4.7
S14	Alsinidal	5.89
S15	Al-shuhada'	4.17
S16	Alhuriya	4.37
S17	Aljumhuriu	5.92
S18	Al-sdeer	7.98
S19	Al-shawfa	7.99
S20	Al-ttabu	5.77
S21	Al-askari	6.04
S22	Al-karama	6.78
S23	Alzuhur	6.88
S24	Al-sdeer 2	6.95
S25	Al-askari 2	4.68
S26	Al-karama	6.41
S27	Aldawr1	4.05
S28	Alshanaafia	6.88
S29	Almuealimin	6.31
S30	Alkhasf	4.01
No of site	Location of sample	Concentration of Uranum by ICP-mass (ppm)
S31	Alsaray	4.56
S32	Aldawr 2	4.27
S33	Alkhasf 2	3.97
S34	Alshanaafia 2	6.21
S35	Al-fawar	6.24

S36	Al-daraeia	6.49
S37	Afak Center	5.77
S38	Aleayn	6.09
S39	fadalallah	6.85
S40	Alkarama	4.27
S41	alsaray	3.25
S42	Almuealimin	3.45
S43	aldighara 1	4.34
S44	aldighara 2	5.82
S45	aldighara 3	5.84
S46	aldighara 4	4.89
S47	aldighara 5	5.97
S48	aldighara 6	4.88
S49	aldighara 7	7.32

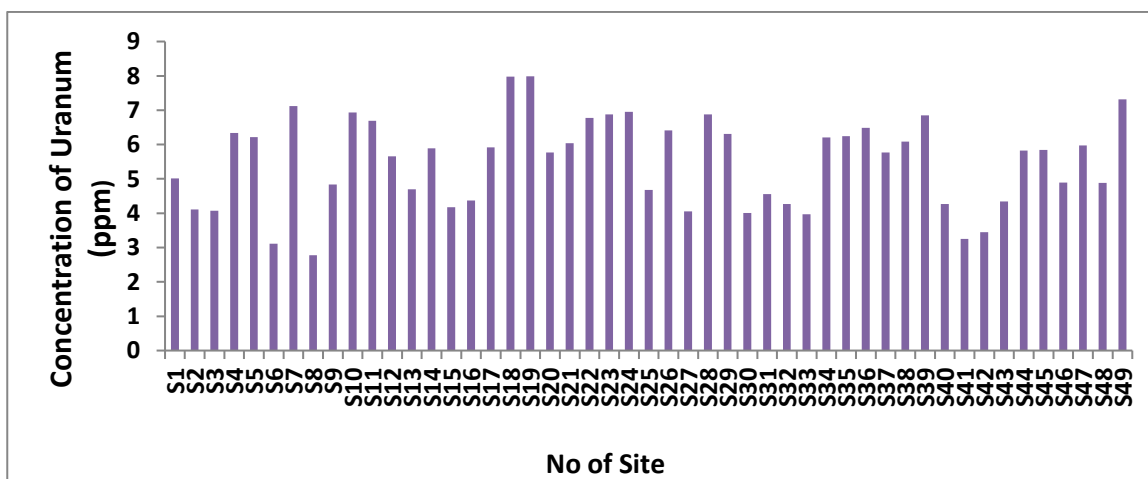


**Figure 2** Uranium Concentration in soil samples from different areas of Al-Diwaniya Governorate analysis by ICP- Mass.

#### 4. CONCLUSION

This study is the first Uranium concentration measurement in soil sources that is performed in the area of Al-Diwaniya Governorate (Iraq). In general, well soil samples within the investigated area are highly mineralized. The correlation analysis revealed the strong positive association between uranium and some chemical compounds in soil samples. Access to safe soil samples is essential to human well-being and is a key public health issue. The maintenance of good quality of soil samples were achieved both by protecting the raw soil samples supply and soil water treatment. It is possible to protect the raw soil samples supply by means of pollution control measures that prevent undesirable constituents from entering the soil samples and by good watershed management practices. The highest concentration of uranium in the soil samples was in the sample (S 19) which is equal to (7.99 ppm), this value is less than the allowed limit, which is equal to (11.7 ppm). The pollution ratio in the region (Al-shawfa ) with uranium is the highest in the comparison with other regions, and this means that the people of this region are the most vulnerable to uranium from the other regions. The uranium

contamination ratio in (Al-sdeer) and the region (Near a Al-sdeer) despite being within allowed limit, but it is the ratio cannot be underestimated, the uranium ratio is relatively high, so it is advisable to processed with all means to ensure the safety of the population from continuous exposure to uranium, while the rest of the proportions of the other regions are reasonable proportions.

### References

- [1] Thaer M. Salman, Sawsan Sh. Fleifil, IOSR Journal of Engineering (IOSRJEN) 5(2015), 43-47.
- [2] UNSCEAR-Sources, effects and risks of ionization radiation, United Nations Scientific Committee on the Effects of Atomic Radiation, Report to the General assembly, with Annexes, New York, 2005.
- [3] U.S. Department of Health and Human Services, Agency for Toxic Substances and Disease Registry. "Toxicological profile for uranium", 2013.
- [4] United Nations Scientific Committee on the Effects of Atomic Radiation, UNSCEAR-Sources, Effect, and Risks of Ionizing Radiation, Report to the general Assembly with Scientific Annexes, United Nations, 1993.
- [5] A. A. Abo Jassim, IOSR Journal of Applied Chemistry (IOSR-JAC) ,6(5)(2014), 61-65.
- [6] Rasheed M. Yousuf, Kamal O. Abullah, ARPN Journal of Science and Technology, 3(6)(2013).
- [7] Ashraf E. M. Khater, Hamed A.Sewaidan.. Ph.D .Thesis. College of Science, University of King Saud. .(2009)
- [8]-M. Gavrilescu, L. V. Pavel and I. Cretescu , Journal of Hazardous Materials, Vol.163(2), (2009). (475-510).
- [9] - Al- Wasity A. M, M.Sc. Thesis, university of Baghdad, Iraq, 2010.
- [10] A. Alyaa, H. Asia, Journal of Current Engineering and Technology, 5(6) (2015).
- [11] M. Gharaibeh, A. Obeidat, W. Al Awawdeh, A. Rousan, *Exp. Theo. Nanotechnology* 3 (2019) 97
- [12] Nidhala H. K. Al-Ani, Qasim, R. Y. and Alwan, A. M. Journal of Al- Nahrain university, 15, 2, 1- 5, (2012).
- [13]- Alia A. Kaddhima and Issraa K. Ahmed, Vol.2,(2014).
- [14] J. Hamed, H. Abd, R. Muzahim, *Exp. Theo. Nanotechnology* 3 (2019) 131
- [15]- Akram. M, Nazar .M, Ghaffar A, Malik. F, Ali N, Mujahid S, Rajput. M. 2013, *World Journal of Nuclear Science and Technology*, Vol. 3 No. 2, pp. 51-58.
- [16]- Mostafa Fayek , journal/minerals ,5, 2015, 133-141.

## **AUTHOR GUIDELINES FOR JOURNAL ARTICLE**

### **Introduction**

This document enables the user to have a better understanding of rules and regulations used for writing journals. However, each institute has its own template so it is advised that after writing any journal or publication, refer to your specific institute references for writing journals and publications.

### **Format**

All files should be submitted as a Microsoft Word Document.

### **Article Length**

Articles should usually be between **4000 and 10000 words** in length. This includes all text including references and appendices. Please allow roughly **280 words** for each figure or table.

### **Article Title**

A title of not more than **16 words** is advised.

### **Article Title Page**

An Article Title Page should be submitted alongside each individual article using the template provided.

This should include:

- Article Title
- Author Details (see below)
- Acknowledgements
- Author Biographies
- Structured Abstract (see below)
- Keywords (see below)
- Article Classification (see below)

### **Author Details**

Details should be supplied on the Article Title Page including:

- Full name of each author
- Affiliation of each author, at time research was completed
- Where more than one author has contributed to the article, details of who should be contacted for correspondence
- E-mail address of the corresponding author

### **Structured Abstract**

Authors should supply a structured abstract on the Article Title Page, set out under 4-7 sub-headings:

- Purpose (mandatory)
- Design/methodology/approach (mandatory)

- Findings (mandatory)
- Research limitations/implications (if applicable)
- Practical implications (if applicable)
- Social implications (if applicable)
- Originality/value (mandatory)

Maximum should roughly be **250** words in total (including keywords and article classification).

### **Keywords**

You should provide up to **10 keywords** on the Article Title Page, which encapsulate the principal topics of the paper.

### **Article Classification**

Categorize your paper on the Article Title Page, under one of these classifications:

- Research paper
- Viewpoint
- Technical paper
- Conceptual paper
- Case study
- Literature review
- General review.

### **Headings**

Headings should be concise, with a clear indication of the distinction between the hierarchies of headings.

The preferred format is for first level headings to be presented in bold format and subsequent sub-headings to be presented in medium italics.

### **Notes/Endnotes**

Notes or Endnotes should be used only if absolutely necessary and must be identified in the text by consecutive numbers, enclosed in square brackets and listed at the end of the article.

### **Research Funding**

Authors must declare all sources of external research funding in their article and a statement to this effect should appear in the Acknowledgements section. Authors should describe the role of the funder or financial sponsor in the entire research process, from study design to submission.

## Figures

All Figures (charts, diagrams, line drawings, web pages/screenshots, and photographic images) should be submitted in electronic form.

All Figures should be of high quality, legible and numbered consecutively Graphics may be supplied in color to facilitate their appearance on the online database.

□ Figures created in Microsoft Word, Microsoft PowerPoint, Microsoft Excel and Illustrator should be supplied in their native formats. Electronic figures created in other applications should be copied from the origination software and pasted into a blank Microsoft Word document or saved and imported into an Microsoft Word document or alternatively create a .pdf file from the origination software.

□ Figures which cannot be supplied in as the above are acceptable in the standard image formats which are: .pdf, .ai, and .eps. If you are unable to supply graphics in these formats then please ensure they are .tif, .jpeg, or .bmp at a resolution of at least 300dpi and at least 10cm wide.

□ To prepare web pages/screenshots simultaneously press the "Alt" and "Print screen" keys on the keyboard, open a blank Microsoft Word document and simultaneously press "Ctrl" and "V" to paste the image. (Capture all the contents/windows on the computer screen to paste into Microsoft Word, by simultaneously pressing "Ctrl" and "Print screen".)

Photographic images should be submitted electronically and of high quality. They should be saved as .tif or .jpeg files at a resolution of at least 300dpi and at least 10cm wide. Digital camera settings should be set at the highest resolution/quality possible.

## Tables

Tables should be typed and included in a separate file to the main body of the article. The position of each table should be clearly labelled in the body text of article with corresponding labels being clearly shown in the separate file.

Ensure that any superscripts or asterisks are shown next to the relevant items and have corresponding explanations displayed as footnotes to the table, figure or plate.

## References

References to other publications must be in Harvard style and carefully checked for completeness, accuracy and consistency. This is very important in an electronic environment because it enables your readers to exploit the Reference Linking facility on the database and link back to the works you have cited through CrossRef.

You should cite publications in the text, for example: (Adams, 2006) using the first named author's name or (Adams and Brown, 2006) citing either names of two, or (Adams et al., 2006), when there are three or more authors. At the end of the paper a reference list in alphabetical order should be supplied:

### **References for Books**

For books you should follow below template:

Surname, Initials (year), Title of Book, Publisher, Place of publication.

### **References for Book Chapters**

For book chapters you should follow below template:

Surname, Initials (year), "Chapter title", Editor's Surname, Initials, Title of Book, Publisher, Place of publication, pages.

*e.g.* Calabrese, F.A. (2005), "The early pathways: theory to practice – a continuum", in Stankosky, M. (Ed.), *Creating the Discipline of Knowledge Management*, Elsevier, New York, NY, pp. 15-20

### **References for Journals**

For journals you should follow below template:

Surname, Initials (year), "Title of article", Journal Name, volume, number, pages.

*e.g.* Capizzi, M.T. and Ferguson, R. (2005), "Loyalty trends for the twenty-first century", *Journal of Consumer Marketing*, Vol. 22 No. 2, pp. 72-80.

### **References for Published Conference Proceedings**

For journals you should follow below template:

Surname, Initials (year of publication), "Title of paper", in Surname, Initials (Ed.), Title of published proceeding which may include place and date(s) held, Publisher, Place of publication, Page numbers.

*e.g.* Jakkilinki, R., Georgievski, M. and Sharda, N. (2007), "Connecting destinations with an ontology-based e-tourism planner", in *Information and communication technologies in tourism 2007 proceedings of the international conference in Ljubljana, Slovenia, 2007*, Springer-Verlag, Vienna, pp. 12-32.

### **References for Unpublished Conference Proceedings**

For unpublished conference proceedings you should follow below template:

Surname, Initials (year), "Title of paper", paper presented at Name of Conference, date of conference, place of conference, available at: URL if freely available on the internet (accessed date).

*e.g.* Aumueller, D. (2005), "Semantic authoring and retrieval within a wiki", paper presented at the European Semantic Web Conference (ESWC), 29 May-1 June, Heraklion, Crete, available at:<http://dbs.uni-leipzig.de/file/aumueller05wiksar.pdf> (accessed 20 February 2007).

### **References for Working Papers**

For Working Papers you should follow below template:

*Surname, Initials (year), "Title of article", working paper [number if available], Institution or organization, Place of organization, date.*

*e.g. Moizer, P. (2003), "How published academic research can inform policy decisions: the case of mandatory rotation of audit appointments", working paper, Leeds University Business School, University of Leeds, Leeds, 28 March.*

### **References for Encyclopedia Entries (no author or editor)**

For encyclopedia entries you should follow below template:

*Title of Encyclopedia (year) "Title of entry", volume, edition, Title of Encyclopedia, Publisher, Place of publication, pages.*

*e.g. Encyclopaedia Britannica (1926) "Psychology of culture contact", Vol. 1, 13th ed., Encyclopaedia Britannica, London and New York, NY, pp. 765-71.*

### **References for Newspaper Articles (non-authored)**

For Newspaper Articles you should follow below template:

*Newspaper (year), "Article title", date, pages.*

*e.g. Daily News (2008), "Small change", 2 February, p. 7.*

### **References for Electronic Sources**

If it is available online, the full URL should be supplied at the end of the reference, as well as a date that the resource was accessed.

*e.g. Castle, B. (2005), "Introduction to web services for remote portlets", available at: <http://www-128.ibm.com/developerworks/library/ws-wsrp/> (accessed 12 November 2007).*

Standalone URLs, i.e. without an author or date, should be included either within parentheses within the main text, or preferably set as a note (Roman numeral within square brackets within text followed by the full URL address at the end of the paper).

=====

For more information

#### **Contact us:**

The Scientific Institute for Advanced Training and Studies

Email: [publisher@siays.co.uk](mailto:publisher@siays.co.uk)

Phone: (0060) 11 113 331 80

WhatsApp & viber

Facebook: <https://www.facebook.com/siats.mutamd?ref=bookmarks>

Experimental and Theoretical NANOTECHNOLOGY

<http://etn.siats.co.uk>

Guidelines link: <http://www.siats.co.uk/author-guidelines-for-journal-article/>

## Content

1. SYNTHESIS OF GAN NANOWIRES BY AMMONIATING $\text{Ga}_2\text{O}_3/\text{BN}$ .....	71
2. CHARACTERIZATION OF $\text{BiFeO}_3$ NANOTUBE AND Y-JUNCTION $\text{BiFeO}_3$ NANOTUBES.....	77
3. NUMERICAL INVESTIGATION OF HEAT TRANSFER AUGMENTATION IN CURVED CHANNEL USING HYBRID NANOFLUIDS.....	85
4. CYTOTOXICITY AND APOPTOTIC ACTIVITY OF MAGNESIUM OROTATE NANOPARTICLES TOWARDS HUMAN HEPATOMA CELL LINE HEPG <sub>2</sub> .....	95
5. ZNO-BASED SENSORS WITH CONTROLLED ETHANOL SENSING.....	101
6. STRUCTURAL AND OPTICAL PROPERTIES OF LEAD IODIDE NANOSTRUCTURE SYNTHESIZED BY VACUUM EVAPORATION METHOD...109	
7. SYNTHESIS OF CDS NANOTUBES AND NANOSPHERES BY LIVING BI-MEMBRANE BI-TEMPLATE.....	127
8. FABRICATION OF NIO/PSI FOR GAS SENSOR APPLICATION PREPARED BY CHEMICAL METHOD.....	135
9. THE INFLUENCE OF RF POWER, PRESSURE AND SUBSTRATE TEMPERATURE ON THE ENERGY GAP TO VANADIUM OXIDE AT TALLNESS WAVE STIR 290 NM OF RF SPUTTERED.....	141
10. STUDY THE EFFECT OF DIFFERENT DILUTIONS FROM FILTRATES OF TWO FUNGI ALTERNARIA ALTERNATA AND ASPERGILLUS FLAVUS ON THE GROUND BEETLES ADULTS (CARABIDAE: COLEOPTERA) HARPALUS RUFIPES.....	147
11. EVALUATION OF URANIUM CONCENTRATION IN SOIL SAMPLES OF AL-DIWANIYA GOVERNORATES USING ICP-MASS TECHNIQUES.....	155